Convective Cloud Microphysical Parameterizations in a Numerical Weather Prediction Model

An Evaluation with Polarimetric Radar Observations

Gregor Köcher

München 2023

Convective Cloud Microphysical Parameterizations in a Numerical Weather Prediction Model

An Evaluation with Polarimetric Radar Observations

Gregor Köcher

Dissertation
der Fakultät für Physik
der Ludwig-Maximilians-Universität
München

vorgelegt von
Gregor Köcher
aus Berlin

München, den 23.05.2023

Erstgutachter: Prof. Dr. Bernhard Mayer
Zweitgutachter: Prof. Dr. Christoph Knote
Tag der mündlichen Prüfung: 11.07.2023

Zusammenfassung

Wolken und Niederschlag sind Wetterphänomene mit dem Potential massive Schäden an Menschen oder Eigentum anzurichten. Üblicherweise werden numerische Wettervorhersagemodelle zur Vorhersage des Wetters, einschließlich solcher Niederschlagsprozesse verwendet. In diesen Modellen trägt die Darstellung der mikrophysikalischen Prozesse in Wolken wesentlich zur Unsicherheit der Niederschlagsvorhersage bei. Besonders schwierig vorherzusagen sind konvektive Wettersituationen. Dies ist zum Teil auf einige grundlegende Wissenslücken bei den zugrunde liegenden mikrophysikalischen Prozessen zurückzuführen. Die Beobachtung mikrophysikalischer Prozesse ist mit drei inhärenten Problemen verbunden: 1) Die Prozesse spielen sich auf sehr kleinen Skalen von Millimetern und weniger ab. 2) Niederschlagsprozesse sind komplex, da unter Umständen viele verschiedene Teilchenformen, -größen oder -phasen beteiligt sind. 3) Niederschlagsprozesse sind variabel; Die Beobachtung der Prozesse in einer Wolke sind nicht zwangsläufig repräsentativ für andere Wolken.

Auf dem Weg zur Verbesserung der Vorhersage von konvektivem Niederschlag werden in dieser Dissertation polarimetrische und Zwei-Wellenlängen-Radarmessungen als Beobachtungsgrundlage für die Bewertung mikrophysikalischer Wolkenmodelle in einem Wettermodell erforscht. Es wird ein Verfahren zur systematischen Charakterisierung von Unterschieden zwischen Modellsimulationen und polarimetrischen Radarbeobachtungen von konvektiven Wetterlagen vorgestellt. Im Gegensatz zu konventionellen Methoden, die typischerweise Einzelfallstudien zur Bewertung eines Modells verwenden, wird diese Bewertung auf statistischer Basis über 30 Tage durchgeführt. Ein Konvektion auflösendes regionales Wettermodell wird mit fünf verschiedenen mikrophysikalischen Schemata unterschiedlicher Komplexität aufgesetzt. Simulierte polarimetrische Radarsignale werden auf Basis der Modellvorhersagen über einen Radarvorwärtsoperator erzeugt. Ein automatisierter Zellverfolgungsalgorithmus erlaubt den objektiven Vergleich zwischen Beobachtungen und Simulationen auf Basis von konvektiven Zellobjekten.

Der sich daraus ergebende Datensatz konvektiver Zellobjekte wird auf verschiedene Weise analysiert, um die angewandten mikrophysikalischen Verfahren statistisch zu bewerten. Erstens werden die makrophysikalischen Eigenschaften konvektiver Wolken, z. B. die Wolkengeometrie, analysiert. Zweitens werden die vertikalen Profile der polarimetrischen Radarsignaturen durch konvektive Wolken verglichen. Drittens wird die Fähigkeit des Modells zur Vorhersage von Starkregen oder Hagelereignissen an der Oberfläche bewertet. Im Allgemeinen zeigt die Auswertung in dieser Dissertation das Potenzial von polarimetrischer Radarmessungen als Beobachtungsgrundlage für die statistische Bewertung von mikrophysikalischen Schemata in Wettermodellen. Probleme der mikrophysikalischen Schemata bei der Reproduktion von bestimmten gemessenen Radarsignaturen

deuten darauf hin, dass Verbesserungen bei der Darstellung von Teilchengrößenverteilungen und von Annahmen zur Teilchendichte erforderlich sind. Komplexere Schemata liefern nicht unbedingt bessere Ergebnisse. Das unterstreicht die Notwendigkeit zunächst die existierenden Mikrophysik-Parameterisierungen zu verbessern, auf Grundlage von Beobachtungen die das Potenzial haben mikrophysikalische Parameter abzuleiten.
Es wurden mehrere Aspekte mit Verbesserungspotenzial ermittelt: 1) Die Größenverteilung der Regentropfen werden nicht korrekt simuliert. Die meisten Schemata erzeugen zu viele große Regentropfen und zu wenige kleine Regentropfen, und nur das „spectral bin“ Schema erzeugt zu wenige große Tropfen. 2) Alle Schemata erzeugen im Vergleich zu den Beobachtungen zu große Gebiete mit Starkregenereignissen. 3) Graupelpartikel oberhalb der Schmelzschichthöhe werden in den meisten Schemata zu groß simuliert. 4) Keines der Schemata ist in der Lage, extreme Reflektivitäten von mehr als 55 dBZ unterhalb der Schmelzschichthöhe zu erzeugen, was wahrscheinlich auf fixe Dichteannahmen zurückzuführen ist.

Abstract

Clouds and precipitation are weather phenomena that have the potential to cause massive damage to people or property. Typically, numerical weather prediction models are used to predict the weather, including such precipitation processes. In these models, the representation of microphysical processes in clouds contributes significantly to the uncertainty of precipitation forecasts. Convective weather situations are particularly difficult to predict. This is partly due to some fundamental gaps in our knowledge of the underlying microphysical processes. There are three inherent problems in observing microphysical processes: 1) The processes occur on small scales of millimeters or less. 2) Precipitation processes are complex because many different particle shapes, sizes, or phases may be involved. 3) Precipitation processes are variable; observations of processes in one cloud are not necessarily representative of other clouds.

Towards improving the prediction of convective precipitation, this dissertation explores polarimetric and dual-wavelength radar observations as a new observational basis for evaluating cloud microphysics schemes in a weather model. A setup is developed for systematic comparison between model simulations and polarimetric radar observations of convective weather situations. Unlike conventional methods that typically use single case studies to evaluate a model, this evaluation is performed on a statistical basis over 30 days. A convection-permitting regional weather model setup is established using five different microphysics schemes of varying complexity. Simulated polarimetric radar signals are generated based on the model predictions using a radar forward operator. An automated cell tracking algorithm allows objective comparison between observations and simulations on a convective cell object basis.

The resulting data set of convective cell objects is then analyzed in several ways to statistically evaluate the applied microphysics schemes. First, macrophysical properties of convective clouds, such as cloud geometry, are analyzed. Second, the vertical profiles of polarimetric radar signatures through convective clouds are compared. Third, the ability of the model to predict high-impact weather events, such as hail or heavy rain, is evaluated. In general, the evaluation in this dissertation demonstrates the potential of polarimetric radar measurements as an observational basis for the statistical evaluation of microphysics schemes in weather models. Problems of the microphysics schemes in reproducing certain observed radar signatures indicate that improvements are needed in the representation of particle size distributions and particle density assumptions. More complex schemes do not necessarily lead to better results in the prediction of heavy precipitation. This underlines the need for observational constraints from measurements that have the potential to infer microphysical parameters.

Several aspects with the potential for improvement were identified: 1) Raindrop size distributions

are not simulated correctly. Most schemes produce too many large raindrops and too few small droplets, and only the spectral bin scheme produces too few large drops. 2) All schemes produce areas of heavy rainfall events that are too large compared to observations. 3) Graupel particles are simulated too large above the melting layer height in most schemes. 4) None of the schemes is able to produce extreme reflectivities of more than 55 dBZ below the melting layer height, likely as a result of fixed density assumptions.

Publications

Parts of this dissertation are published in:

Köcher, G., Zinner, T., and Knote, C.: Influence of cloud microphysics schemes on weather model predictions of heavy precipitation, Atmospheric Chemistry and Physics Discussion [preprint], https://doi.org/10.5194/acp-2022-835, 2022a

Köcher, G., Zinner, T., Knote, C., Tetoni, E., Ewald, F., and Hagen, M.: Evaluation of convective cloud microphysics in numerical weather prediction models with dual-wavelength polarimetric radar observations: methods and examples, Atmospheric Measurement Techniques, 15, 1033– 1054, https://doi.org/10.5194/amt-15-1033-2022, 2022b

- Parts of chapter 1 in Köcher et al. (2022b,a)
- Sections 3.1–3.5 of chapter 3 in Köcher et al. (2022b)
- Sections 3.7 of chapter 3 in Köcher et al. (2022a)
- Sections 4.3.1 and 4.4 of chapter 4 in Köcher et al. (2022b)
- Sections 4.5 of chapter 4 in Köcher et al. (2022a)
- Parts of chapter 5 in Köcher et al. (2022b,a)

The content of Köcher et al. (2022b,a) has been slightly adapted when incorporated into this dissertation to avoid repetition, align naming conventions, and maintain clarity.

Contents

Chapter 1

Introduction

Algebra applies to the clouds

Victor Hugo

Of all the phenomena that nature has to offer, clouds are, in my opinion, one of the most fascinating. They can appear in every imaginable shape and size. Starting with a beautiful summer cloud, to a gray, stratiform winter cloud, or a mighty cumulonimbus cloud. There are liquid clouds, ice clouds, mixed phase clouds, precipitating clouds, non-precipitating clouds, high altitude clouds, low altitude clouds, even fog is basically nothing but a cloud. Naturally, many people from different backgrounds have studied clouds – from artists to photographers, or from children who see flowers or animals in the shape of a cloud to researchers trying to unlock nature's secrets. One of the most common subjects ever photographed is probably the sunset, which is really only half as beautiful without clouds reflecting the reddish light to the observer. What the sunset so beautifully demonstrates shows an aspect of clouds that makes them interesting to scientists: they can interact with radiation. If sunlight is reflected into space, we would expect a cooling effect on the Earth, but if longwave radiation originating from the Earth is "trapped" and emitted back towards Earth, then that would lead to warming. This makes the net effect that clouds have on the Earth's climate difficult to predict. In fact, the Intergovernmental Panel on Climate Change (IPCC) cites clouds as the aspect with the greatest uncertainty due to various feedbacks of the climate response to a radiative forcing (Arias et al., 2021, their Fig. TS.17). However, clouds are not only a problem for climate predictions; they are also difficult to predict accurately for weather forecasts that focus on much shorter time periods. Clouds, in fact, not only affect radiation, but are also critical to precipitation formation (Fig. 1.1). Rain always falls from clouds - no one has ever seen rain under a clear blue sky. But not every cloud rains. So what happens inside a cloud to make it rain? And how can it be predicted?

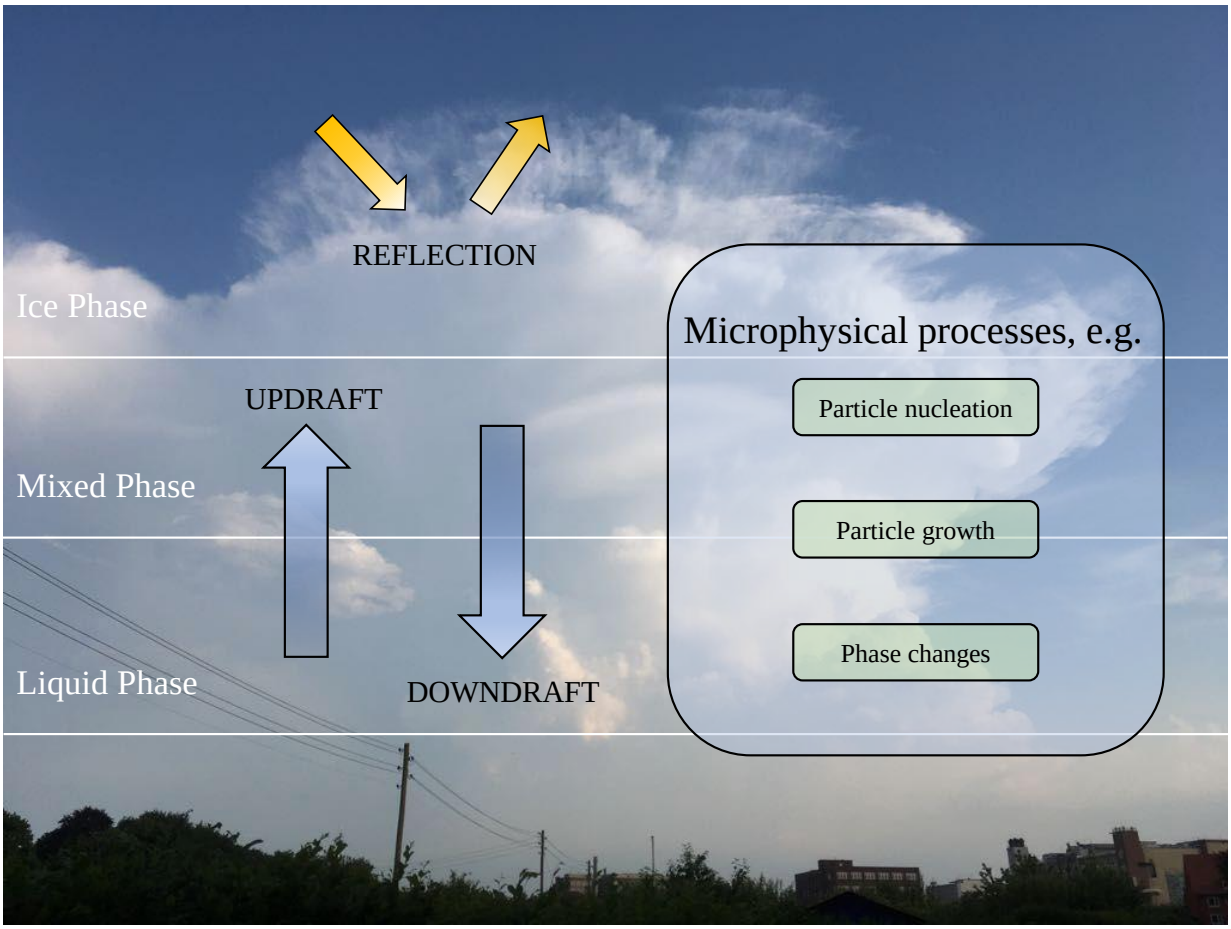

Figure 1.1: A thunderstorm over Germany.

1.1 What is Numerical Weather Prediction?

Primarily, the atmosphere consists of a mixture of gases: air. Therefore, if one wants to make predictions about the evolution of the atmosphere, physical laws are required that describe the flow of air, or more generally of fluids. Such equations have been known for a long time and were already widely used at the beginning of the 20th century (Coiffier, 2011b, p. 1). Bjerknes (1904) was the first to recognize the potential for weather prediction and the difficulty of solving these equations, which cannot be solved analytically, i.e., there is no exact solution (Coiffier, 2011b, p. 2). The exact solution of this equation is instead approximated by numerical methods: the *numerical weather prediction* (NWP). Not long after that, the first actual NWP system to solve them was developed by Richardson (1922), which remains the basis of NWP until today (Inness and Dorling, 2013b, p. 2). However, at that time there were no computers and the calculations had to be done by hand. In the end, it took Richardson six weeks just to predict the air pressure in Central Europe for a few hours. To make matters worse, the prediction turned out to be completely wrong (Durran, 2010b, p. 1). The idea, however, of using physical equations to describe and

predict the weather was not lost. Eventually, Charney et al. (1950) were able to do the first NWP that was considered successful, though far from perfect (Arakawa, 2000, p. 6).

The physical equations describing atmospheric fluid dynamics in a NWP model are a non-linear system of partial differential equations (Inness and Dorling, 2013c, p. 10). For non-linear systems, there may be feedbacks that amplify or attenuate the initial changes, which can lead to very large changes as the state of the atmosphere evolves. This was demonstrated accidentally by Ed Lorenz in the 20th century (Inness and Dorling, 2013c, p. 10–11). Lorenz performed a NWP using numbers from a paper printout up to three decimal places, while the computer used numbers to six decimal places. This tiny change in initial conditions, resulted in a prediction that very soon deviated from the original. This effect is often referred to as the *butterfly effect* and essentially means that no matter how accurately we define the initial conditions, instrument error alone (not to mention poor observational coverage of the Earth's atmosphere) will cause the prediction to deviate from reality, no matter how perfect the model physics. Of course, many studies have been done to examine the limits of atmospheric predictability, and the current limit for weather forecasts is estimated to be about 14 days (Inness and Dorling, 2013c, p. 11–12).

Forecasting convective weather is a particular challenge. As early as 1969, Lorenz (1969) claimed that "cumulus-scale motions" can only be predicted up to one hour. Convective clouds are clouds formed by the vertical transport of heat (Doswell III, 2001, p. 1). Warm air that rises eventually cools, resulting in condensation of water vapor: a convective cloud forms. A convective cloud can be a boring summer cumulus cloud, but it can also be a powerful thunderstorm. Convective processes take place on a scale of about 10 km (Doswell III, 2001, p. 1). Until recently, these processes were too small to be resolved by NWP models and were instead parameterized, i.e., the processes were not explicitly calculated, but their effect on important variables was estimated with other, known parameters (Clark et al., 2016). In recent years, the grid spacing of many models has been reduced to the point where convective processes can be explicitly simulated (e.g., Pinto et al., 2015, Baldauf et al., 2011, Seity et al., 2011, Lean et al., 2008). This has been a major advance for numerical prediction of thunderstorms and convective precipitation (Clark et al., 2016), leading for example to much more accurate predictions of precipitation amounts. Despite this progress, however, the prediction horizon for features at the thunderstorm scale is still on the order of a few hours (Zhang et al., 2015, 2016). For example, Bachmann et al. (2019) show that even with an absolutely idealized model setup, they were unable to predict the exact location of convective precipitation without the aid of data assimilation. The predictability of convective precipitation depends on several factors, including orography, the prevailing synoptic weather regime, or microphysical uncertainties (Kühnlein et al., 2014, Hanley et al., 2011, 2013, Barrett et al., 2014). Although it seems too ambitious to try to predict the exact location of convective storms, NWP models show some skill in predicting convective weather situations in general. In some cases, for example, rainfall intensity or daily precipitation totals are accurately predicted over several days, even if the exact location or timing of the precipitation is not correct (e.g., Spiridonov et al., 2020, Zhu et al., 2022). Therefore, the ability of NWP models to predict convective precipitation should be evaluated on a statistical basis over a longer period of time and over some area, rather than on the basis of exact locations.

Today's national weather services typically use NWP models to forecast weather, including the

cloud processes that lead to precipitation (e.g., ICON-DE from the German Meteorological Service, Zängl et al., 2014). Some of these processes include the formation and growth of "minute particles" (Houze, 1994, p. xiii), with scales of millimeters and smaller: the microphysical processes. Microphysical processes are important for precipitation formation, but are too small to be resolved by a NWP model and must be parameterized instead. This has the potential to introduce uncertainties, as important processes could be misrepresented or missed out completely. As such, modeling microphysics is challenging and subject to large uncertainties (Morrison et al., 2020, Fan et al., 2017). A variety of different microphysics schemes are used in current operational NWP models, varying greatly in their complexity. Often, microphysics schemes make very simple assumptions. For example, some of the simulated hydrometeors (meteorological particles, i.e., particles consisting of liquid or frozen water) are typically simply assumed to be spherical. Even though these simple assumptions do not capture the complexity of real microphysical processes, increasing the scheme's complexity does not automatically improve the prediction accuracy. For example, simply allowing other than spherical particle shapes will not improve a prediction if it is not known under which circumstances the involved particles will take on other shapes. Furthermore, as the complexity of the microphysics scheme increases, so does the computational power required, which is often the limiting resource in weather prediction. The weather prediction published by the German Meteorological Service (Deutscher Wetterdienst, DWD), for example, takes about two hours to compute, on a super computer that covers a nearly $1000\,\mathrm{m}^2$ large hall (Deutscher Wetterdienst, 2023b). Thus, more complex microphysics schemes must provide significant better prediction results to justify their use in a weather model. Arguably the most complex schemes by design are spectral bin schemes that resolve the particle size distribution (PSD) explicitly and require high computational effort (Khain et al., 2015). There are some intercomparison studies that find bin schemes to give better results compared to more traditional "bulk" schemes (e.g. Fan et al., 2015, Li et al., 2009, Khain et al., 2015). However, other studies demonstrate that the spread among different bin schemes is equally large compared to the spread between bulk schemes (vanZanten et al., 2011, Xue et al., 2017) or find no clear advantage of bin schemes over bulk schemes in ice microphysics dominated convection simulations (Han et al., 2019, Stanford et al., 2017). It is known that many processes, especially those involving ice microphysics, are poorly represented in NWP models (Morrison et al., 2020). One reason is that direct observation of these complex processes is very difficult due to the size of the particles involved at millimeter scales and below, as well as the many different shapes, sizes, or phases of the particles involved. Therefore, in order to constrain more complex microphysical processes implemented in a NWP model and to assess the benefit of the additional complexity, novel observations are needed that provide such information.

1.2 Evaluation of Microphysics with Radar Observations

Direct (in situ) measurements in clouds, for example with aircraft, provide the potential for information about small-scale microphysical cloud processes, but such measurements are expensive and require much effort. Moreover, it is not possible to cover several parts of the cloud or several

clouds at the same time; in situ measurements are spatially limited. Satellite observations do have the potential to cover many clouds at once, but due to their distance to the clouds the spatial resolution is limited. Ground-based radar observations, in contrast, provide measurements over a large atmospheric volume with high temporal and spatial resolution. In recent years, polarimetric radar measurements have become available. In 2009 DWD began upgrading the national radar network to full dual-polarimetric radars that perform operational polarimetric volume scans over all of Germany with a temporal resolution of 5 min (Helmert et al., 2014). The polarimetric radar data is highly useful because the polarimetric information is affected by many particle population properties, such as particle phase, density, orientation, shape, or number concentration. Polarimetric information can be used for many different applications, such as improved quantitative precipitation estimation (QPE) from radar measurements (Ryzhkov et al., 2022), hydrometeor identification (HID) algorithms (e.g., Park et al., 2009), or microphysical ice retrievals (e.g., Tetoni et al., 2022). Especially important for this work is that polarimetric radar variables are affected by many microphysical aspects which could be useful to evaluate and improve NWP models (Ryzhkov et al., 2020). However, radar information cannot be directly integrated in a weather model, because a typical NWP model does not know any radar variables, such as for example the radar reflectivity. Therefore, to compare NWP model output with radar observations, an additional step is required that transforms the radar variables to model variables or the other way around. In principle, NWP model output can be compared to polarimetric radar signals in two different ways (Fig. 1.2): 1) converting the model output to polarimetric radar signatures using a polarimetric radar forward operator (e.g., Ryzhkov et al., 2011, Augros et al., 2015, Snyder et al., 2017) or 2) retrieving microphysical information from the polarimetric radar signal (e.g., Cao et al., 2010). These two approaches and related literature are described in a review paper by Ryzhkov et al. (2020).

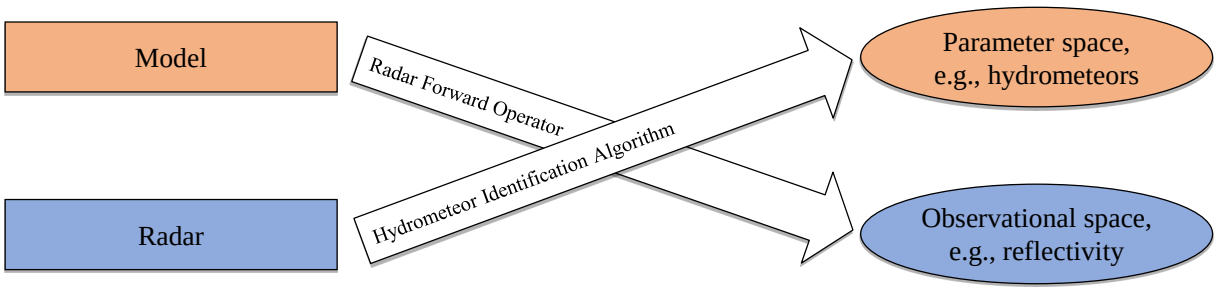

Figure 1.2: Schematic of the two ways to compare radar observations with weather model output.

Another approach to obtain microphysical information of a cloud is to use two radars of different wavelength: the dual-wavelength approach. The reflectivity that a radar measures depends, among others, on its wavelength and the PSD of the hydrometeors that are measured. This means that the difference in reflectivity between the two radars in the dual-wavelength approach is sensitive to the characteristic size of the measured hydrometeors. The advantage of the dual-wavelength approach

is that it is independent of the particle number concentration. Used as a complementary variable to the polarimetric data, this helps to further constrain the microphysical parameters. This work was initiated within the framework of the project IcePolCKa (Investigation of the initiation of convection and the evolution of precipitation using simulations and polarimetric radar observations at C- and Ka-band), a subproject of the German Research Foundation (Deutsche Forschungsgemeinschaft, DFG) priority programme 2115 PROM (Polarimetric Radar Observations meet Atmospheric Modelling – Fusion of Radar Polarimetry and Numerical Atmospheric Modelling Towards an Improved Understanding of Cloud and Precipitation Processes; Trömel et al., 2021).

1.3 Outline and Scientific Objectives

In this thesis, the polarimetric and dual-wavelength radar observations will be used to address two open research questions:

1. ***Can polarimetric radar observations provide sufficient microphysical information to statistically evaluate microphysics schemes?***
2. ***Does greater complexity in microphysics schemes improve numerical weather predictions of convective weather?***

The remainder of this work is structured as follows. In chapter 2, the theoretical background that is required to understand the results of the main chapters is explained. This includes a section on radar theory and a section on NWP. In chapter 3, the methods and data set are described. The main results are shown and discussed in chapter 4. This includes a discussion of the synoptic situation of the underlying dataset (Sect. 4.1), a demonstration of the model's behavior on an example case (Sect. 4.2), an evaluation of the macrophysical and microphysical cloud characteristics that were produced by the model (Sect. 4.3 and Sect. 4.4, respectively), and an analysis of the influence of the cloud microphysics schemes on high-impact weather predictions, such as heavy precipitation and hail (Sect. 4.5). The conclusions are drawn in chapter 5, together with a short summary and an outlook about the way to proceed from here.

Chapter 2

Theory

2.1 Numerical Weather Prediction

The primary goal of this work is to utilize polarimetric radar observations to evaluate and improve weather prediction with a *numerical weather prediction* (NWP) model. In this section, the fundamentals of NWP modeling are introduced, explaining all aspects that are required to understand the results derived later. There are now a number of textbooks that explain the basics of NWP. This section largely follows four of them: "Fundamentals of Numerical Weather Prediction" by Coiffier (2011a), "Numerical Weather and Climate Prediction" by Warner (2011a), "Operational Weather Forecasting" by Inness and Dorling (2013a), and "Numerical Methods for Fluid Dynamics" by Durran (2010a). Whenever literal quotations, equations, or figures have been taken directly from these textbooks, this is indicated with the appropriate source citation.

2.1.1 Basic Principle

In principle, the development of a numerical weather model consists of two main steps:

1. establishing a set of equations suitable to describe the continuous behavior of the atmosphere: the governing equations.

2. replacing the equations involving continuous variables with equations involving discrete variables: the *discretization*.

Mathematically, weather prediction can be thought of as an *initial value problem*. The physical equations are covered by the governing equations, which describe how a fluid will change with time t. Thus, to make a prediction for tomorrow, we must determine the state of the atmosphere today, and then use the governing equations to project into the future. Therefore, even if we had a perfect model that is 100 % physically correct in describing how the atmosphere behaves, we would still produce an incorrect prediction if the initial conditions are not correct. It is therefore critical to set the initial conditions as accurately as possible. A good way to specify the

initial conditions is to use what is called *reanalysis data*. Reanalysis data is a mixture of past short-range weather forecasts and current observations combined through a process called data assimilation. The reason for this is that observations are 1) not available everywhere, much less evenly distributed around the globe, and 2) observations are also subject to measurement error. Therefore, better results are obtained when short-term weather forecasts are used in combination with actual observations to fill in the gaps for which observations are not available and to account for measurement errors. In this work, the reanalysis data of the Global Forecast System (GFS; National Centers For Environmental Prediction/National Weather Service/NOAA/U.S. Department Of Commerce, 2015) at 0.25° horizontal grid spacing and hourly time steps is used.

In the following, the two main components of a NWP model are discussed in more detail, in particular with an emphasis on methods used by the Weather Research and Forecasting (WRF; Skamarock et al., 2019) model, which is the NWP model used for this work.

2.1.2 Basic Equations

In order to make a weather forecast, the physical laws that describe how the atmosphere changes over time must be defined. These equations are referred to as the *governing equations*, and in the context of a weather model, they are often referred to as the *dynamical equations* or simply the *model dynamics*. These are, for the most part, fundamental laws of physics that relate to the conservation of certain quantities: momentum, mass, energy, and water, as well as an *equation of state* relating certain thermodynamic quantities of state. Depending on the applied assumptions, the set of equations could be simplified. The model used in this work employs the *non-hydrostatic Euler* equations as the governing equations.

$$\frac{\mathrm{d}\vec{v}}{\mathrm{d}t} = -\frac{1}{\rho}\nabla p - 2\vec{\Omega}\times\vec{v} + \vec{g} \quad \text{(Momentum equation)} \tag{2.1}$$

$$\frac{\mathrm{d}T}{\mathrm{d}t} = \frac{\dot{Q}}{c_\mathrm{p}} + \frac{RT}{pc_\mathrm{p}}\frac{\mathrm{d}p}{\mathrm{d}t} \quad \text{(Thermodynamic equation)} \tag{2.2}$$

$$\frac{\mathrm{d}\rho}{\mathrm{d}t} = -\rho\nabla\cdot\vec{v} \quad \text{(Continuity equation)} \tag{2.3}$$

$$\frac{\mathrm{d}q}{\mathrm{d}t} = \dot{Q}_\mathrm{v} \quad \text{(Water vapor equation)} \tag{2.4}$$

$$p = \rho RT \quad \text{(Ideal gas law)} \tag{2.5}$$

These equations and their quantities will be explained in the following.

Momentum equation

Newton's second law essentially describes the conservation of momentum, which can be used to predict how the momentum of a body (or fluid) changes in response to a force acting on the

body. This law states that the acceleration experienced by a body is the sum of all the forces acting on it. In the case of a fluid, these forces are the *gravitational forces*, *frictional forces*, and *pressure gradient forces*, usually expressed as accelerations (mass-specific forces). The change in velocity of a fluid is described by the famous *Navier-Stokes* equation, which can be expressed for an incompressible fluid following Vallis (2017, p. 12) as

$$\frac{\partial \vec{v}}{\partial t} + (\vec{v} \cdot \nabla)\vec{v} = -\frac{1}{\rho}\nabla p + \nu \nabla^2 \vec{v} + \vec{f}\,, \tag{2.6}$$

where $\frac{\partial \vec{v}}{\partial t}$ is the local change of the velocity $\vec{v}$ with time t, $\vec{v} \cdot \nabla \vec{v}$ describes the spatial advection, ρ is the fluid density, p is the fluid pressure, ν is the kinematic viscosity coefficient of the fluid, and $\vec{f}$ describes any external forces, i.e., the gravitational force for a fluid on Earth. The advection term $\vec{v} \cdot \nabla \vec{v}$ is a nonlinear term, and thus this equation generally cannot be solved analytically (Holton and Hakim, 2012b, p. 455). The sum on the left side of this equation is the *Lagrangian* change of the fluid velocity $\frac{\mathrm{d}\vec{v}}{\mathrm{d}t} = \frac{\partial \vec{v}}{\partial t} + \vec{v} \cdot \nabla \vec{v}$. Technically, this equation is only valid for an inertial system, i.e., the coordinate system is not accelerated. However, for an accelerated system (such as the Earth, which is constantly rotating), the same formula applies, provided that the so-called *apparent forces*, i.e., the apparent relative forces due to the acceleration of the coordinate system, are taken into account. For a body on Earth, these are the *centrifugal force* and the *Coriolis force*. Substituting all these forces into Eq. (2.6) we obtain the *momentum equation*. Following Holton and Hakim (2012a, p. 37) under the assumption of a frictionless atmosphere, i.e., assuming inviscid fluids so that the viscosity term can be omitted, the momentum equation is defined as

$$\frac{\mathrm{d}\vec{v}}{\mathrm{d}t} = \underbrace{-\frac{1}{\rho}\nabla p}_{\text{Pressure gradient force}} \quad \underbrace{-2\vec{\Omega} \times \vec{v}}_{\text{Coriolis force}} \quad \underbrace{-\vec{g}}_{\text{Effective gravity}} \tag{2.7}$$

In the formula, underbraces indicate which term belongs to which force. Gravitational and centrifugal forces have been merged to an *effective gravity* with $\vec{g} = (0, 0, -g)$ and $g = 9.81\,\mathrm{m\,s^{-2}}$ the acceleration due to gravitational and centrifugal forces. $\vec{\Omega}$ is the rotation vector of Earth with $\vec{\Omega} = (0, \Omega\cos(\phi), \Omega\sin(\phi))$, where $\Omega = 7.292 \times 10^{-5}\,\mathrm{s^{-1}}$ is the angular speed of the Earth's rotation and ϕ is the latitude.

Ideal gas law

The ideal gas law is a diagnostic relationship (that is, there is no time derivative in the equation) between certain meteorological variables, and is defined following Inness and Dorling (2013d, p. 60) and Warner (2011b, p. 7) as

$$p = \rho R T\,, \tag{2.8}$$

where ρ is air density, R is the specific gas constant for dry air, p is atmospheric pressure, and T is air temperature. If two of the meteorological variables p, T, or ρ are known, the ideal gas law allows the third to be calculated.

Thermodynamic energy equation

The thermodynamic energy equation is derived from the first law of thermodynamics, which means that the equation describes the conservation of energy. Following Coiffier (2011c, p. 16), the thermodynamic energy equation as it is used in NWP models can be defined as

$$\frac{\mathrm{d}T}{\mathrm{d}t} = \frac{\dot{Q}}{c_\mathrm{p}} + \frac{RT}{pc_\mathrm{p}}\frac{\mathrm{d}p}{\mathrm{d}t}\,. \tag{2.9}$$

Physically, this equation describes the rate of temperature change $\mathrm{d}T$ with a time change $\mathrm{d}t$. The first term on the right describes any diabatic heat sources or sinks. This can be, for example, absorbed solar radiation. This term is only affected by the heating rate $\dot{Q}$ and the specific heat capacity c_p of the medium, for example air. The second term on the right describes the change in temperature due to expansion or compression. R is the specific gas constant, T is temperature and p is pressure. The expansion or compression of air is work, which accordingly affects the temperature of the air.

Continuity equation

The continuity equation is derived under the assumption that mass can neither be created nor destroyed. Following Holton and Hakim (2012a, p. 47), the continuity equation is defined as

$$\frac{\mathrm{d}\rho}{\mathrm{d}t} = -\rho\nabla\cdot\vec{v}\,, \tag{2.10}$$

where ρ is density and $\vec{v}$ the fluid speed vector, i.e., the wind vector. The term $\nabla\cdot\vec{v}$ is referred to as the velocity *divergence*. This equation states that the density change of an air parcel changes with the velocity divergence. If the divergence is greater than 0, the density of that air parcel decreases; if it is smaller, the density increases.

Water vapor equation

Just like the conservation of mass, the conservation of water vapor can be described in an equation. According to Coiffier (2011c, p. 16), this can be defined as

$$\frac{\mathrm{d}q}{\mathrm{d}t} = \dot{Q}_\mathrm{v}\,. \tag{2.11}$$

$\frac{dq}{dt}$ describes the Lagrangian change (following an air parcel) with time t of some humidity variable q, for example the water vapor mixing ratio. $\dot{Q}_v$ represents any sinks and sources that change the humidity, for example by evaporation or condensation.

2.1.3 Solving Equations Numerically: The Discretization

In the previous section, the physical equations describing the behavior of the atmosphere were derived and explained. But when attempting to use these equations for a prediction, one faces a problem: they cannot be solved analytically, i.e., there is no exact solution (or no exact solution is known). That is, it is not (yet?) possible to write down an equation for, say, the temperature at time t: $T(t)$. What we can solve for, however, is how T *changes* at time t: $\mathrm{d}T/\mathrm{d}t$. This is exactly what is described by the governing equations. However, of course, we are actually not so much interested in how T will change *at* a given time, but how T will change *over* some finite time. For a perfect prediction, using the governing equations, we would have to start with an initial value and then calculate an infinite number of infinitesimally small time steps over the time range of interest. Of course, this is not possible in reality; calculating an infinite number of time steps would take an infinite amount of time. Instead, one must choose a finite time step Δt in which the temperature then changes by ΔT. As long as the chosen Δt is small, this is a reasonable approximation and is called a finite difference or grid point (Fig. 2.1) approximation (Inness and Dorling, 2013d, p. 80). For spatial derivatives, for example $\partial p/\partial x$ from the pressure gradient force, an analogous approach can be taken.

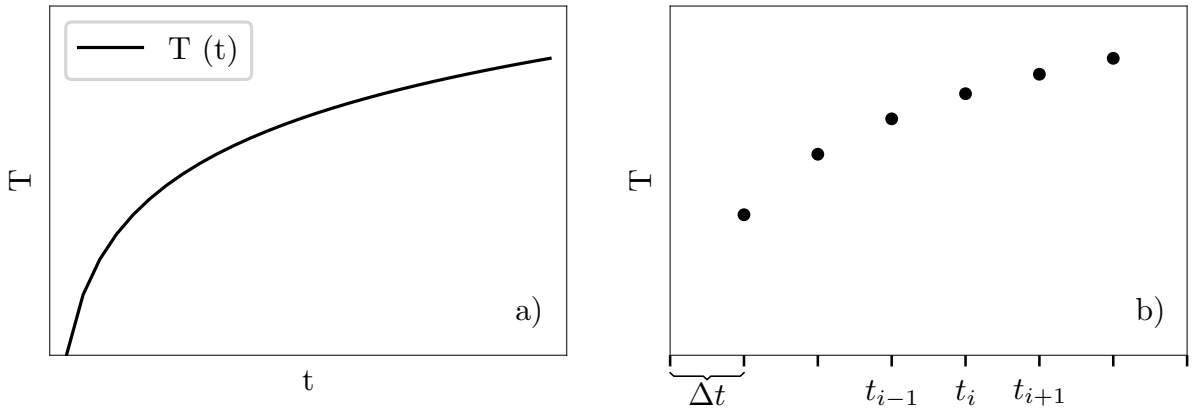

Figure 2.1: **(a)** Continuous function of some meteorological variable T, e.g., temperature. **(b)** The same meteorological variable expressed on a discrete grid, which can be both, a time or a spatial (x, y, z) grid. Figure adapted from Lunkeit (2015).

It should be noted that the finite difference approximation is not the only way to numerically solve a continuous equation. Other common options are, for example, the spectral method, finite element, or finite volume methods. However, to explain them all is beyond the scope of this theory chapter,

especially since the numerical model used in this work only uses the finite difference approximation. Instead, the reader is referred to the literature, for example Warner (2011a, chapter 3), Inness and Dorling (2013d, chapter 4), or Coiffier (2011a, chapters 3, 4, and 5).

Time integration

There are different approaches for integrating the discretized equations over time. Let us say, for example, that the change of a variable T with time t is described by some function $\upsilon(T)$ with $\upsilon(T) := \frac{\partial T}{\partial t}$, just like it is the case for many of the governing equations. The simplest methods to integrate such equations over time are called single-step schemes and defined following Durran (2010c, p. 43)

$$\frac{T_{\mathrm{i+1}} - T_{\mathrm{i}}}{\Delta t} = (1-\alpha)\upsilon(T_{\mathrm{i}}) + \alpha\upsilon(T_{\mathrm{i+1}})\,, \tag{2.12}$$

When the factor α is set to 0, this method is referred to as the forward-Euler method. Setting α to 1, the backward-Euler method is obtained. In the case of the forward-Euler method, the temperature at time step $i+1$ is calculated from the gradient at time step i. Therefore, this method is called an *explicit* method. For the backward-Euler method, on the other hand, the temperature at $i+1$ depends on the gradient at $i+1$ as well. This is an *implicit* method method (Durran, 2010c, p. 47). These two simple time integration schemes are visualized in Fig. 2.2.

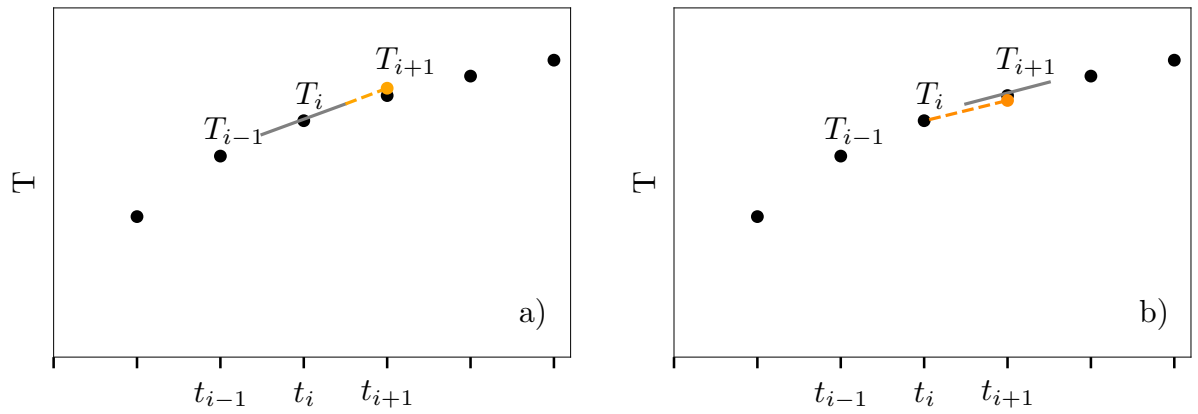

Figure 2.2: Time integration schemes. **(a)** Forward-Euler (explicit) scheme. **(b)** Backward-Euler (implicit) scheme. The gray line visualizes the gradient at T_{i}. The orange line visualizes the integration from time steps t_{i} to $t_{\mathrm{i+1}}$. Figures adapted from Lunkeit (2015).

In practice, many different types of schemes are in use. Of particular note is the *Runge–Kutta* scheme (Durran, 2010c, p. 49–55), which is employed in the numerical model used here. The idea of the Runge–Kutta scheme is to use not one gradient to calculate the next value, but several (usually four) between t_{i} and $t_{\mathrm{i+1}}$ and average them. This makes the Runge–Kutta method more computationally intensive, but also leads to better results.

Numerical stability

In order to decide on a suitable time integration scheme, one must know which advantages and disadvantages a scheme brings to the model. To evaluate a time integration scheme, there are criterions such as consistency, convergence, accuracy, and numerical stability. The most important evaluation measure is the stability. Typically, numerical stability is violated when the time steps are large compared to the grid spacing. Since the finite difference method uses local gradients to calculate a rate of change over the entire path length, it can cause problems if an air parcel crosses several grid boxes at once over a single time step. This would make local gradients inappropriate for the calculation, and can cause variables to grow very quickly in an unrealistically short time and "blow up" the model, thus violating the stability criterion of a limit. A famous criterion for diagnosing numerical instability is the so-called *Courant–Friedricks–Lewy* (CFL) condition, which is defined following Inness and Dorling (2013d, p. 85) as

$$\max(u)\frac{\Delta t}{\Delta x} \leq 1\,, \tag{2.13}$$

where $\max(u)$ is the fastest possible atmospheric motion. In other words, this criterion states that an air parcel must never move over more than one grid box during a time step.

Model grid spacing

The previous part already explained why a numerical model requires a discretization of continuous functions. For a good prediction, a forecaster wants to have as small time or grid steps as possible, so that the deviations from the truth are as small as possible. However, each additional step means an additional computation, which increases the computation time. In practice, the forecast must be available quickly. A forecast for tomorrow that is not available for a week, for example, is not very useful. Therefore, there will always be a trade-off between model accuracy and model grid spacing (in time and space). In this work, a grid spacing of 400 m is applied, which is about a factor of 5 better than current operational NWP models (e.g., ICON-DE at 2.2 km, Zängl et al., 2014).

Model resolution

An important consideration in deciding what grid resolution a model should have, is the scale of the processes that this model should represent. Atmospheric processes can span many different scales. If one is interested in processes at a particular scale, the grid spacing of the model must resolve that process. For example, to resolve a process that occurs at the scale of 10 km, a much smaller grid spacing is required. This is illustrated in Fig. 2.3.

In meteorology, processes are often referred to as *resolved* if the grid spacing of the model is at least a factor of 5 smaller than the size scale on which the process typically occurs. Processes that are resolved by the model are usually referred to as *grid-scale* processes, while processes that remain unresolved are referred to as *subgrid-scale* processes.

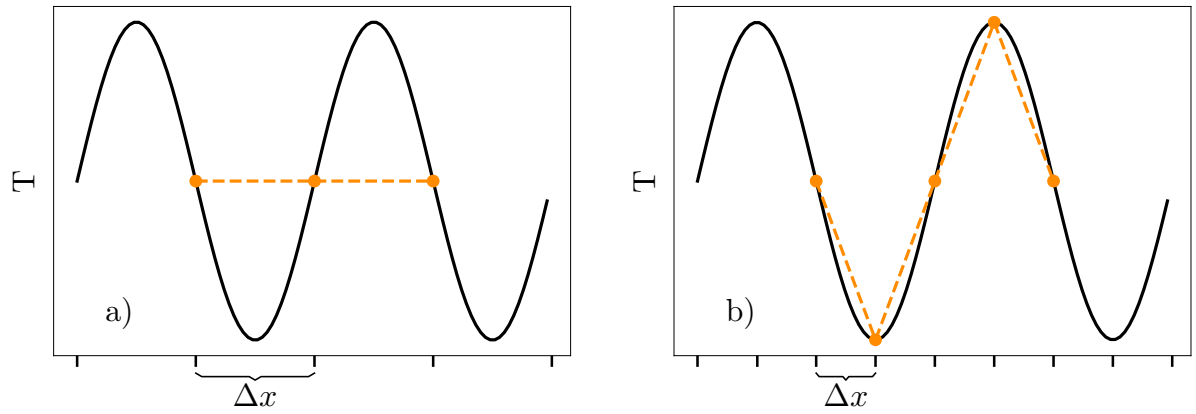

Figure 2.3: Schematic diagram illustrating grid resolution. A wavelike meteorological variable T, for example temperature, along the x-direction of the grid, is represented by the black solid line. The resolution of a given grid spacing is represented by the orange dashed line. **(a)** A grid spacing that is not capable of resolving the wave. **(b)** A grid spacing that resolves the wave. Figure adapted from Inness and Dorling (2013a, p. 87).

2.1.4 Parameterizations

The governing equations 2.1 – 2.5 are not a completely closed system. There are sinks and source terms in the water vapor, thermodynamic, and momentum equations. This means that the equations are not a complete description of atmospheric processes. Also, processes that are not resolved by the model grid (subrid-scale, see explanation from previous section) cannot be represented by the discretized model equations. Thus, the effect of such processes must be accounted for in some other way. This is then called a *parameterization*. In essence, the physical processes are not explicitly calculated, but their effect on one variable is described with some other but known parameters. Thus, a parameterization is not a physically realistic way of representing a process, but it is often better to represent a process with a parameterization than not to include it at all. Sometimes the effect of these processes can be neglected, but there are also processes that occur on a small scale but can still have a large effect on important model variables. In such cases, parameterization is required.

Typical parameterizations concern radiative transfer, surface and boundary layer processes, convection, and cloud microphysics. Below is a short description of radiative transfer and surface and boundary layer parameterizations. As convection and cloud microphysics are in the focus of this dissertation, they will be explained in more detail in the sections thereafter.

1. **Radiative transfer**

   Radiation propagating through the atmosphere interacts with molecules and particles. It can be transmitted, reflected, absorbed, or scattered by atmospheric gases, by aerosols, by clouds, or by the Earth's surface. How the energy is propagating through the atmosphere also depends on its wavelength. The resulting heating (or cooling) rates are determined by radiative transfer parameterizations.

2. **Surface and boundary layer processes**

   Friction is the most important sink for atmospheric momentum. The amount of friction depends strongly on the surface properties. Of course, it is too complex to consider every surface detail to calculate the exact friction, so this effect must be parameterized.

2.1.5 Cloud Microphysics

The processes that determine cloud extent and precipitation particle growth occur on scales of millimeters and smaller. These scales are far too small for an operational numerical weather model to calculate explicitly. Therefore, these processes must be parameterized. Cloud microphysics is an aspect in numerical weather models that leads to large uncertainties and is a focus of this work. There are several reasons for this, as the formation and growth of cloud particles (especially in the ice phase) is still only partially understood and extremely difficult to measure accurately due to the high complexity of the particles involved and the small scales. There are a number of different microphysics schemes of widely varying complexity that attempt to parameterize the particle growth processes in a cloud. Typically, these schemes are categorized as either *bulk* or *bin* schemes, although other categories also exist. Bulk schemes predict one or more "bulk" moments of multiple hydrometeor classes, such as the total mass mixing ratio of cloud droplets in a grid box. This mass is then distributed among different particle sizes by assuming a predefined particle size distribution (PSD) shape. Bulk schemes are further categorized by the number of predicted bulk moments. A one-moment scheme (e.g., Kessler, 1969) predicts only the mass mixing ratio. Two-moment schemes (e.g., Morrison et al., 2009) predict the mass mixing ratio and the number concentration of a hydrometeor class. Three-moment systems often predict the radar reflectivity as a third moment in addition to the mass mixing ratio and number concentration (e.g., Milbrandt and Yau, 2005). In contrast to bulk schemes, bin schemes predict mass and number concentrations for a set of variables ("bins") without prescribing a particular PSD. The variables are predicted independently for each of the bins. This is much more computationally expensive, since all processes must be computed for each bin. For a 33-bin scheme, as used in this work, this means an increase in computational power by a factor of 33.

In recent years, other alternative methods have been developed. The "Predicted Particle Properties" (P3; Morrison and Milbrandt, 2015) scheme departs from dividing ice particles into categories of hydrometeor classes, each with constant particle properties, and instead predicts the properties of ice particles, such as the riming mass mixing ratio. This is considered more flexible and is in fact closer to nature. In reality, there is not a one single class of cloud ice with a particular density or shape. Instead, cloud ice can have different densities and shapes. For example, it can

be partially rimed, which would make it a mixture of the cloud ice and graupel classes, but this does not exist in traditional bulk schemes. Although the P3 scheme allows for more flexible ice properties, this does not necessarily mean that they will be simulated correctly; this depends on the parameterization applied to associate other meteorological variables with the ice properties.

Another recent development are Lagrangian cloud models (LCM; Shima et al., 2009), which calculate cloud microphysics based on individual particles (super droplets) representing a family of particles with the same properties. This has the advantage that a larger variety of different particles can be considered. However, the computational power required and the diversity covered depend heavily on the number of particles used, and since this is a fairly new technique, most LCMs to date can only account for liquid droplets.

2.1.6 Convection

Convection is the vertical transport of sensible and latent heat. Convective processes often occur on scales that are not captured by weather models. In this case, the effect must be parameterized. However, the simulations with the model in this work have been performed with a grid spacing good enough to resolve convective processes of 2 km and larger. Therefore, no convection parameterization was used. This also means that convective processes smaller than 2 km in size cannot be simulated correctly. The driving force behind convection is the buoyancy force, which results from temperature and thus density differences between rising air and the environment. Mathematically, the acceleration due to the buoyancy force can be described following Doswell III (2001, p. 1)

$$B = g\frac{T - T'}{T'}\,, \tag{2.14}$$

where T is the temperature of the rising air and T' is the environmental temperature.

Two conditions are required for a convective cloud to form: 1) conditional instability and 2) a trigger. Conditional instability results from the state of the atmosphere, i.e., the moisture and temperature profile. An air parcel rising to altitudes with lower pressure expands and cools accordingly. If, for example, the environmental temperature increases with altitude, the air parcel will quickly be cooler than its surroundings and will not continue to rise – the atmosphere is considered stable and convection cannot occur. Conditional instability is usually expressed in terms of *Convective Available Potential Energy* (CAPE), a measure that describes how much energy a hypothetical parcel of air would have if it were to rise adiabatically in a given environment and is defined following McMurdie and Houze (2005, p. 345)

$$CAPE = R\int_{p_{\mathrm{EL}}}^{p_{\mathrm{LFC}}} (T_{\mathrm{v,p}} - T_{\mathrm{v,0}})\,\mathrm{d}\ln p\,, \tag{2.15}$$

where B is buoyancy, p is pressure, $T_{\mathrm{v,p}}$ and $T_{\mathrm{v,0}}$ are the virtual temperatures of a rising air parcel and the environment, respectively, and R is the specific gas constant. p_{EL} is the pressure at the *equilibrium level*, at which the air begins rising freely and accelerates, due to higher temperature

than the environment. p_{LFC} is the pressure at the *level of free convection*, at which the temperature of the parcel is again the same as the environment and hence the buoyancy is 0 again. The CAPE value determines how strong potential thunderstorms can get. Situations with 0 CAPE would not have the potential to develop thunderstorms, which is often the case with stable weather. In principle, any CAPE value greater than 0 can produce at least convective clouds. However, the CAPE value determines how severe showers or thunderstorms can become. The German Meteorological Service (Deutscher Wetterdienst, DWD) categorizes CAPE values up to $500\,\mathrm{J\,kg^{-1}}$ as a typical potential for weak thunderstorms, up to $1000\,\mathrm{J\,kg^{-1}}$ for moderate thunderstorms, 1000–$2000\,\mathrm{J\,kg^{-1}}$ for strong thunderstorms, and anything above $3000\,\mathrm{J\,kg^{-1}}$ with the potential for extreme thunderstorms (Deutscher Wetterdienst, 2023a).

Even if conditional instability is present, this does not necessarily mean that convection will occur. For example, there may be a warm, stable layer of air above the surface, measured by *Convective Inhibition* (CIN), that blocks any potential convection, even if the layers above are unstable. CIN describes the energy required to adiabatically lift an air parcel to the level of free convection. CIN sometimes prevents thunderstorms, even when there is theoretically plenty of potential energy available, because air parcels are unable to overcome CIN to reach heights where they can rise freely and make use of the CAPE. To generate actual deep convection, a trigger is required in addition to conditional instability. In principle, a trigger can be any mechanism that causes air to rise to the level of free convection, so the air subsequently continues to rise freely and is accelerated by the potential energy of atmospheric instability. Typical triggers include local convergence, heating of the surface due to solar radiation, or forced lift due to terrain, such as when air overflows a hill. By definition, convective clouds are formed by vertical air transport. However, if one measures the reflectivity of a cloud with a radar, it usually cannot be inferred from this whether it was really the vertical air movement that led to the cloud formation. Convective precipitation, however, is usually characterized by higher radar reflectivity values than stratiform precipitation. This fact is exploited by automatic convective cloud tracking algorithms that identify and track convective precipitation based on reflectivity thresholds. For example, the tracking algorithm used in this work uses a reflectivity threshold of 32 dBZ to identify convective cells (Raut et al., 2021).

2.1.7 Nested Models

The possible model grid spacing is often limited by the available computing power. Global weather forecasts therefore typically have horizontal grid spacing greater than 10 km and even with advances in computer science, it is currently too costly to reduce horizontal grid spacing further. However, this means that only processes on scales larger than 50 km are resolved (see Sect. 2.1.3 on grid resolution). Thunderstorms, for example, are often on a much smaller scale, however, and are still important to forecast because of their damage potential. The solution that many forecasters use to address this problem are *Limited Area* or *regional* models (LAMs), in which the simulation does not run over the entire globe, but only over a limited area called the model *domain* (Fig. 2.4). When the same number of grid points are distributed over a smaller area, the distance between two grid points is naturally much smaller, and thus the grid spacing is much smaller for the same computational power. Not only does this allow for more accurate

results due to the smaller spacing steps Δx, it also has the advantage that some processes that must be parameterized at the grid spacing used at the global scale can now be explicitly resolved.

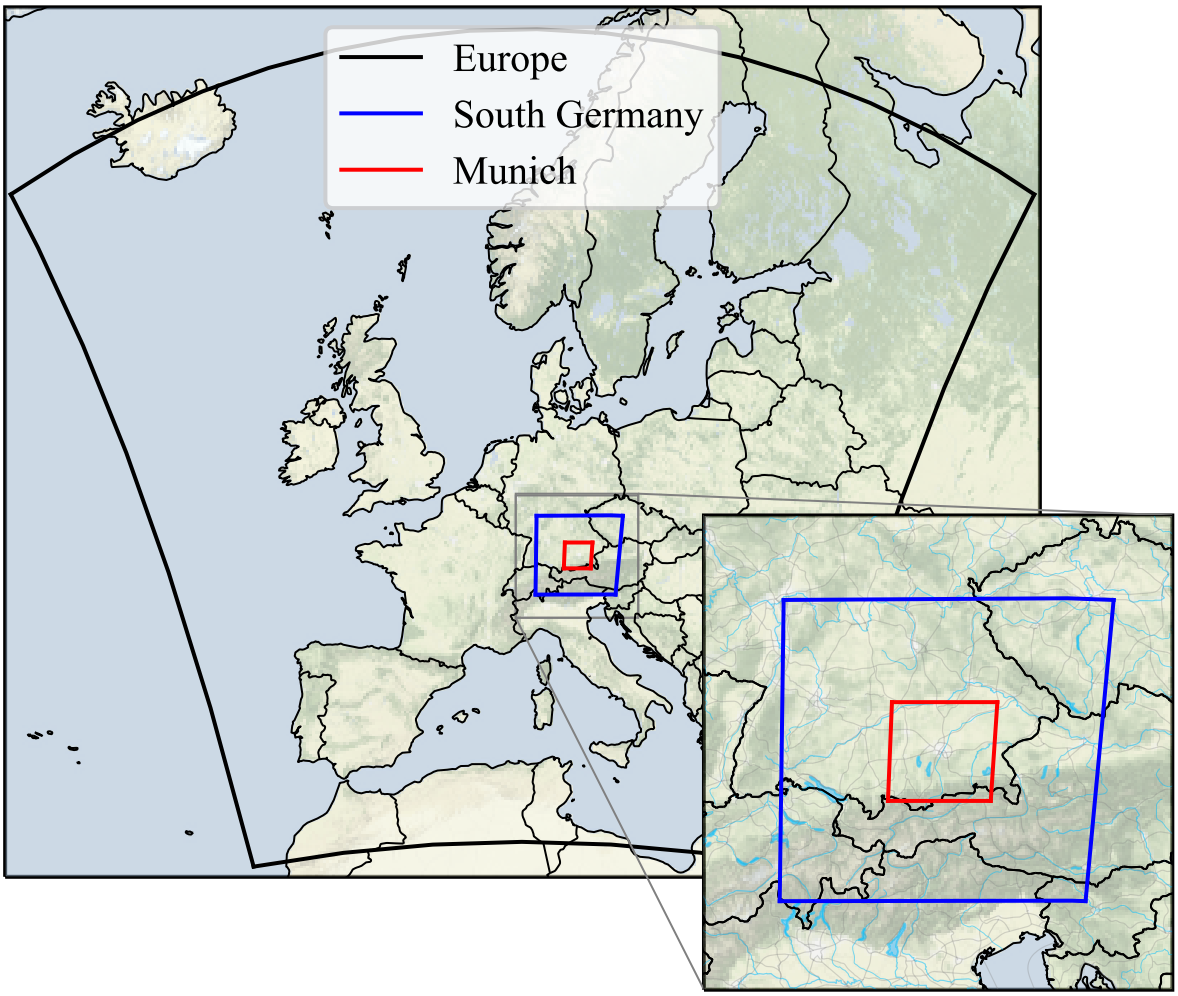

Figure 2.4: A setup of nested domains that was used in this work. Background map tiles by Stamen Design (Stamen Design, 2023). Background map data by OpenStreetMap (OpenStreetMap, 2023). Roads, rivers, and lakes made with Natural Earth (Natural Earth, 2023).

However, the atmosphere over this limited area naturally interacts with the atmosphere of the rest of the globe. There will be weather systems, such as a cyclone, that propagate from somewhere else into the domain simulated by the LAM. Therefore, in addition to the initial conditions, a LAM also needs so-called *boundary conditions* that provide information about the transport of variables from outside into the model domain. A LAM can therefore never run alone, but a global model is always required to define the boundary conditions at the boundaries of the LAM domain.

A LAM that is run within a global model is called a *nest*. The global model is run first, and the meteorological values predicted by the global model at the boundaries of the LAM domain are

used as boundary conditions for the LAM. In principle, any number of nests is possible. One can run multiple nests within the global domain, for example, if there are multiple areas where it is of interest to resolve mesoscale features or orography. One can also use multiple levels of nests: nests within nests. This might be useful to keep the resolution at which the boundary conditions are passed to the child domain at a roughly similar scale. It is common to use a grid spacing ratio of 3:1 or 5:1 between the child and parent domains. However, there are also studies that suggest that a ratio of 10:1 or even 30:1 does not significantly change the quality of the prediction (Liang et al., 2019).

A basic distinction is made between *one-way* and *two-way* nested grids. One-way nesting means that information is passed in only one direction, from the parent nest to the child nest. Two-way nests mean that the information is passed in both directions. The boundary conditions are passed to the lower-level nest, where the meteorological variables are predicted with a smaller grid spacing, and the corresponding high-resolution (and thus arguably better) simulation results are returned to the higher-level domain, which then uses these values to continue its prediction for the higher-level domain.

2.2 Radar Theory

In this work, radar measurements are utilized to compare and evaluate microphysical aspects of a weather prediction model. Hence, several aspects of radar theory are necessary to correctly interpret and discuss the results obtained in the main chapters. Therefore, some background information on radar theory is given in this section, along the lines of several textbooks dealing with quite different (or the same) aspects of radar. These include mainly "Radar for Meteorologists" by Rinehart (1997a), but also "Radar Technology" by Detlefsen et al. (1989a), "Introduction to RADAR Systems" by Skolnik (2001a), "Doppler Radar and Weather Observations" by Doviak (1984a), "Radar Meteorology" by Fabry (2017a), "Polarimetric Doppler Weather Radar" by Bringi and Chandrasekar (2001a), "Radar Observation of the Atmosphere" by Battan (1973a), and "A Short Course in Cloud Physics" by Rogers and Yau (1989a). Whenever literal quotations, equations, or illustrations have been taken directly from these textbooks, this is marked with the appropriate source citation.

The best way to explain how radar works is to start with the word *radar*. Radar is the abbreviation for *radio detection and ranging*. This already describes the origin pretty clearly: radio waves. It did not take long to discover that radio waves could be used to detect metallic objects. During World War II, this proved to be very useful, and so great effort was put into the development of radar. One notable development is the *cavity magnetron* (Boot and Randall, 1946), which allowed the wavelength of radars to be reduced. With shorter wavelengths, radar systems could also be made much smaller and more compact than before. However, these *microwave* radars also detected spurious echoes from other origins that did not belong to any metallic objects. It was soon discovered that radars in the microwave range could detect not only aircraft or ships, but also precipitation. After World War II, military radars soon became available for civilian use and were further developed for civilian purposes, such as precipitation monitoring (Rinehart, 1997b, p. 1–3). But how exactly does a radar work?

2.2.1 Basic Principle

A radar is an active remote sensing device. A *remote sensing* device, unlike an in situ measuring device, does not have to be in direct contact with the quantity to be measured. *Active* means that, unlike *passive* remote sensing devices, an electromagnetic signal is generated by the radar itself and actively radiated into the atmosphere. Potential targets, such as raindrops or aircraft, scatter some of this energy back, which is then measured by the radar. Most radars are so-called pulsed radars. They emit a short pulse of energy and wait for the signal to return. From the time that elapses between transmission and reception of the signal, the distance to the target can be determined. The power received gives an indication of the number, size, or type of the particles that scattered the signal. Some time must elapse for all echo signals to return to the radar before the next pulse is transmitted. If this is not assured, an echo from a distant target arriving after the next pulse has already been sent could be incorrectly assigned to a shorter distance. This means that the rate at which pulses can be sent is limited. Given a specific pulse repetition frequency (f_{pr}), the distance beyond which objects are assigned to an incorrect range gate is called the *maximum*

unambiguous range (R_{un}) and following Skolnik (2001b, p. 3) defined as

$$R_{\mathrm{un}} = \frac{c}{2\, f_{\mathrm{pr}}}\,, \tag{2.16}$$

where c is the speed of light and the factor 2 results from the fact that the pulse must travel the distance to the target twice before being received back at the radar. Not all radars are pulsed radars. There are also radars that emit a continuous signal, called *continuous-wave* (CW) radars. A simple CW cannot measure distance. However, by modulating the frequency or phase slightly during the transmission of the wave, a CW can also be used to determine range information. All radars used for this work are pulsed radars, so only these will be introduced in the following.

2.2.2 Radar Hardware

A radar consists of three main components:

1. **Transmitter**. The transmitter generates the microwave signal. There are different types of transmitters. For example, the MIRA-35 radar used in the following and operated at the Meteorological Institute Munich (MIM) uses a magnetron.

2. **Antenna and reflector**. The antenna focuses the signal in one direction, radiates it into the atmosphere, and receives the backscattered signal. The actual antenna is only the radiation source, usually a *feedhorn*, which is then combined with a reflector that directs the signal away from the radar (Fig. 2.5).

   In radar meteorology, the term antenna usually includes the reflector. An isotropic reflector would radiate energy uniformly in all directions. However, this would obviously not be very practical for any application to locate targets. Instead, most antennas have parabolic-shaped reflectors that focus the outgoing signal in a specific direction. Antennas cannot focus the signal perfectly in one direction. They also transmit (and receive) signals that are off the main direction (Fig. 2.6). The terms used are *main lobe* (main direction) and *side lobes* for signals radiated in a direction different from the main direction. Some of the radiated energy even is emitted into backward directions as so-called *back lobes*.

   To describe how much of the transmitted power is focused on the main direction, the *antenna gain* (G) is used. Antenna gain describes how much power P_1 is focused along the center of the beam axis compared to the power P_2 of an isotropic antenna that would radiate equally in all directions (Battan, 1973b, p. 29)

   $$G = \frac{P_1}{P_2}\,. \tag{2.17}$$

   However, most of the power is usually transmitted to the main lobe, and the power density falling into a side lobe is generally less than $\frac{1}{100}$th of the peak density in the main lobe (Doviak, 1984c, p. 24). The antenna gain of the MIRA-35 antenna, for example, is 48.9 dB (Bauer-Pfundstein, 2012). To describe how fast the beam power decreases away from the center

Figure 2.5: MIRA-35 radar, located at the Meteorological Institute Munich (MIM).

of the beam axis, the term *beamwidth* is used. The beamwidth is defined as the angular width at which the power is exactly half the power from the center of the beam axis at the same distance. It depends on the wavelength emitted and the size of the reflector. The relationship between beamwidth (ω), wavelength (λ), and reflector diameter (D_A) is according to Fabry (2017b, p. 15)

$$\omega \approx 1.22 \frac{\lambda}{D_\mathrm{A}} \,. \tag{2.18}$$

This essentially means that for a given wavelength, the beamwidth is only affected by the size of the reflector: the larger the reflector, the smaller the beamwidth. So, from a meteorological point of view, one would always prefer a larger antenna yet. However, small antennas are also easier to handle, cheaper, and often the available space is limited.

3. **Receiver**. The receiver detects and amplifies the signals received by the antenna, which are usually weak. The received signal can be up to 20 orders of magnitude smaller than the transmitted signal (Fabry, 2017c, p. 205).

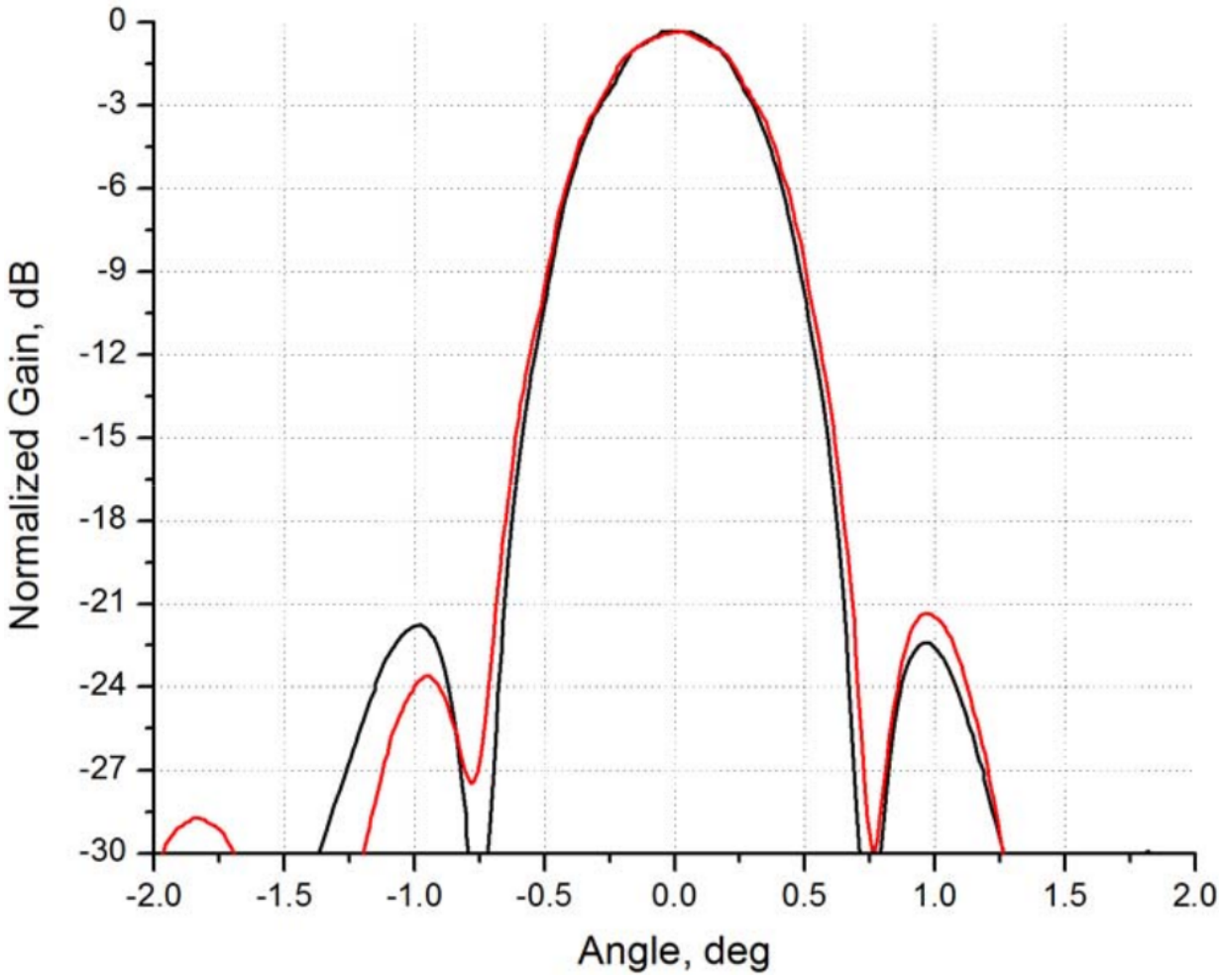

Figure 2.6: Beam pattern of the MIRA-35 antenna for both polarizations (Bauer-Pfundstein, 2012).

Of course, there are many other parts involved in a radar, such as modulators to generate the correct waveform, waveguides to connect the transmitter and antenna, transmit/receive switches to protect the receiver, a signal processor to remove clutter and to calculate basic radar quantities, or simply a computer that communicates with the radar. However, radar data can be used in most cases without a deep understanding of these parts, and no further knowledge about these hardware components are needed for this work. For more information, refer to Rinehart (1997a), Detlefsen et al. (1989a), or Skolnik (2001a).

2.2.3 Electromagnetic Radiation

It has already been mentioned that radars, as active remote sensing devices, emit *electromagnetic* radiation into the atmosphere. But what is electromagnetic radiation? Again, the name gives a clue to this: electromagnetic radiation consists of two force fields, one electric and one magnetic, which

oscillate at a certain frequency and propagate in space at the speed of light c. The electric and magnetic fields are always perpendicular to each other and also perpendicular to the direction of propagation. Two important quantities to characterize electromagnetic radiation are its frequency f and wavelength λ. These are connected by

$$f = \frac{c}{\lambda} . \tag{2.19}$$

Electromagnetic spectrum

Nowadays, conventional weather radars operate in the microwave range, i.e., with electromagnetic radiation with wavelengths between 1 mm and 1 m which equals frequencies between 300 GHz and 300 MHz, respectively (Doviak, 1984b, p. 4). These frequencies were not chosen by chance. For radiation to propagate through a medium, that medium hast to be transparent in the first place. In our atmosphere, the transmissivity strongly depends on the wavelength of the electromagnetic radiation. At some wavelengths, the atmosphere absorbs the radiation completely, making those wavelengths unsuitable for remote sensing. However, there are so-called *atmospheric windows* through which electromagnetic radiation of certain wavelength can penetrate the atmosphere. In the microwave range, where radars operate, a number of atmospheric windows at different wavelengths exist. The names for these so-called *radar bands* originated in the military, but are still used today (Fabry, 2017b, p. 19). The most commonly used radar bands and their corresponding wavelengths are shown in Table 2.1.

Table 2.1: Most frequently used radar bands and their frequencies. Table adapted from Raghavan (2003, p. 26).

Band designation	Frequency range	Important applications
S	2–4 GHz	Precipitation measurements, local severe storms
C	5–7 GHz	Local severe storms, precipitation measurements
X	9–11 GHz	Thunderstorm and gust front detection
Ka	27–40 GHz	Cloud physics, attenuation measurements
W	94 GHz	Cloud microphysics and dynamics

Propagation of electromagnetic radiation

As electromagnetic radiation propagates through the atmosphere, interactions with the atmosphere occur. This is what makes electromagnetic radiation useful in the first place. If there were no interactions, accordingly no radiation would be scattered back to the radar and no information on the target location could be derived. However, electromagnetic radiation not only interacts with objects of interest, but there are other, often undesirable, interactions as well. Therefore, it is

important to understand how electromagnetic radiation propagates in the atmosphere in order to properly interpret radar signals.

There are different possibilities of interaction between electromagnetic radiation and the medium through which it propagates. Electromagnetic radiation that enters a different medium can change its direction due to *refraction*, it can be *scattered*, it can even be *absorbed*, resulting in a temperature increase of the medium.

Refraction

The speed at which light travels depends on the medium through which it travels. The ratio between the speed of light in a vacuum c and the speed in a medium c_m is called the *refractive index* (n) of that medium, and is defined following Rinehart (1997c, p. 50)

$$n = \frac{c}{c_\mathrm{m}} \,. \tag{2.20}$$

For example, air has a refractive index of 1.0003 near the surface, which means that electromagnetic radiation propagates about 0.03 % slower in air than in vacuum. Normally, the refractive index is greatest at the surface and decreases with height, due to the decrease in air density with height. This means that radar waves propagate faster at altitude than near the surface, causing the waves to bend downward (Fig. 2.7).

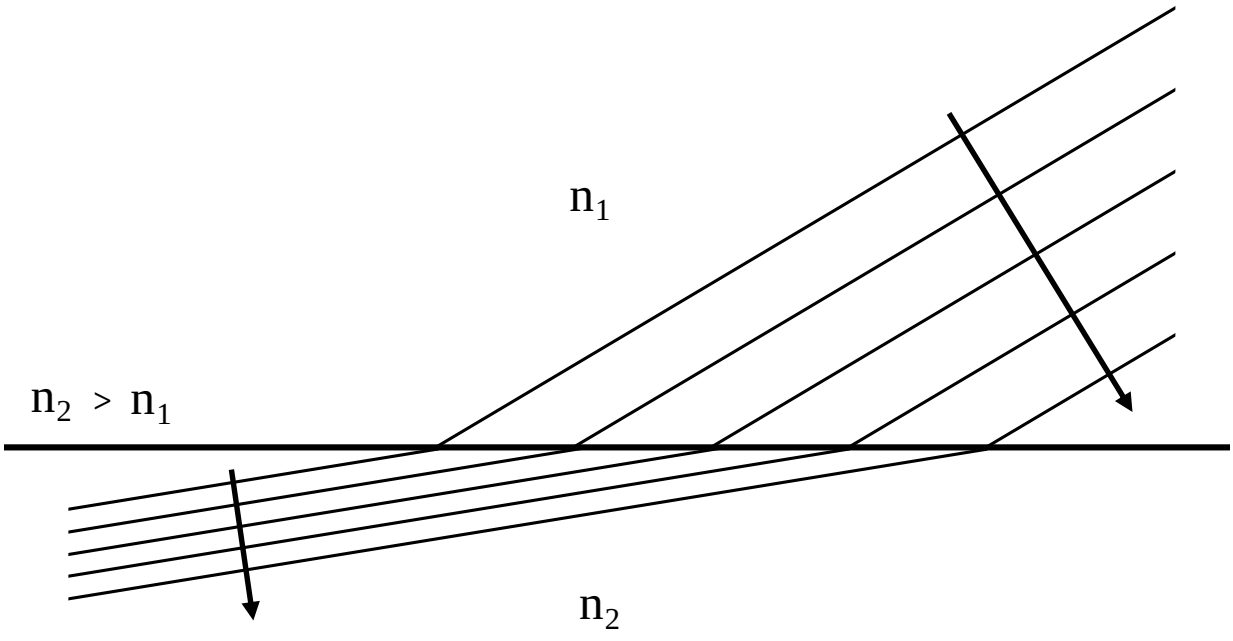

Figure 2.7: Schematic of an electromagnetic wavefront changing its direction due to refraction when entering a medium of different refractive index.

For a pulse of radiation emitted by a radar located at the Earth's surface, this backward refraction is not negligible, but still small compared to the curvature of the Earth for typical gradients of refractive indices in the atmosphere. Therefore, the height of the beam above the surface generally still increases with distance from the radar.

To simplify the curved radar beam problem, radar meteorologists sometimes consider the beam path to be a straight line, and instead increase the radius of the Earth to an *effective radius* $a_e = k_e a_o$, so that the refraction is exactly compensated by this increased radius of the Earth. In that equation, a_o is the actual radius of the Earth and k_e is a factor that increases the earth radius to compensate for the effect of beam refraction. Using this approach, the height h of the radar beam above the surface for any distance r (along the radar beam) is calculated as

$$h = \sqrt{r^2 + {a_e}^2 + 2ra_e \sin\theta} - a_e\,, \tag{2.21}$$

where θ is the elevation of the radar (the derivation of this formula is described in Doviak, 1984b, p. 13). In the remainder of this work, Eq. (2.21) is used whenever the height of a radar beam above the surface is required.

Technically, the exact beam height can only be predicted with this formula, if the refractive index of the air along the beam path is known (which determines a_e). However, the refractive index of air depends on several atmospheric variables, e.g., temperature, atmospheric pressure, or water vapor pressure. Therefore, the exact refractivity along the entire optical path is usually unknown. Under most atmospheric conditions, it has been found empirically that for the wavelengths of conventional weather radars, the gradient of the refractive index within the lowest 10–20 km is typically $-1/(4a_o)$ according to Doviak (1984b, p. 13). This is equivalent to an effective Earth radius of $a_e = 4/3a_o$. However, under certain atmospheric conditions, for example, strong temperature inversions, the actual refractive index may differ significantly from this, and then the beam propagation cannot be predicted accurately.

Scattering

When electromagnetic radiation encounters a medium with a change in refractive index they are not only refracted, a fraction of the radiation can also be scattered in different directions.

Scattering cross section

A particle that interacts with electromagnetic radiation intercepts a fraction of the incoming energy and scatters it in different directions. To describe this fraction, one uses the *scattering cross section*. The scattering cross section of an object is defined as an area, namely exactly the area that a perfectly spherical and isotropic scatterer would have to reflect the power actually reflected by that object. While the scattering cross section has the unit of an area, it is not only related to the physical size of the target. Often the shape rather than the size determines the scattering cross section (Skolnik, 2001c, p. 49–64). For example, thin metallized fibers (also called chaff, used by the military to disturb radar signals) may have a very small physical cross section, but their

scattering cross section is many times larger. A chaff element of 0.1 mm diameter and a length of 5 cm along the electric field, for example, has at a wavelength of 10 cm a radar cross section of 8.6×10^{-3} m^2, while the geometric area is only 5×10^{-6} m^2 according to Doviak (1984c, p. 27) and Nathanson (1969). While the light can be scattered in all directions, only the portion that is directly scattered back to the radar is of interest. The relevant parameter is then called *backscatter cross section*, *radar cross section*, or sometimes simply *cross section*.

Scattering regimes

The radar cross section σ depends, among other things, on the diameter D of the object and the wavelength λ of the incident radiation. The relationship between these two quantities is described by the size parameter γ, following Fabry (2017b, p.13)

$$\gamma = \frac{\pi D}{\lambda} . \tag{2.22}$$

The size parameter helps to distinguish between three regimes in which the scattering (and hence the radar cross section) have different characteristics: the optical regime, the Rayleigh regime, and the Mie regime.

1. **Optical regime**

   If a spherical particle is significantly larger than the incident wavelength ($\gamma > 10$), then the radar cross section of this particle is independent of the wavelength and actually corresponds to its geometric area (Rinehart, 1997d, p. 69)

   $$\sigma = \frac{\pi}{4} D^2 . \tag{2.23}$$

   However, this is a special case for spherical particles. For any other shape, the actual radar cross section can be very different from the geometric area – and usually is, especially in the optical regime. For example, a flat square plate reflector of 1 m^2 geometrical area has at 10 cm wavelength a radar cross section of 1257 m^2 (Rinehart, 1997d, p. 74).

2. **Rayleigh regime**

   If the object is significantly smaller than the wavelength ($\gamma < 0.1$), then we speak of so-called *Rayleigh scattering* (Rayleigh, 1899). In this range, the scattered energy is usually emitted almost isotropically (Doviak, 1984c, p. 28). The radar cross section then depends only on the incident wavelength λ, the diameter of the target particle D, and the dielectric factor $|K|^2$ and is defined following Bringi and Chandrasekar (2001b, p. 17) and Battan (1973b, p. 38) as

   $$\sigma = \frac{\pi^5}{\lambda^4} |K|^2 D^6 . \tag{2.24}$$

The dielectric factor $|K|^2$ is calculated from the particle's relative permittivity ϵ_r following Bringi and Chandrasekar (2001b, p. 17)

$$|K|^2 = \left|\frac{\epsilon_r - 1}{\epsilon_r + 2}\right|^2 . \tag{2.25}$$

From Eq. (2.24), it can be seen that in addition to the dielectric factor, the radar cross section also depends on the diameter of the particle and the incident wavelength. The radar cross section depends on the particle diameter to the sixth power ($\sigma \sim D^6$). That is why, in the case of several particles in the same volume, the total radar cross section is usually strongly dominated by the largest particles. At the same time, the radar cross section is proportional to $1/\lambda^4$. This essentially means that the radar cross section is larger for smaller wavelengths, a fact that was used by Rayleigh (1899) to explain why the sky is blue (Doviak, 1984c, p. 28): blue light is scattered more efficiently by air molecules than red light when propagating through the atmosphere because of the smaller wavelength.

3. **Mie regime**

   For size parameters between the Rayleigh and the optical range ($0.1 < \gamma < 10$), the scattering is referred to as *Mie scattering* (Mie, 1908). In this range, the scattering in the propagation direction (forward scattering) can be 100–1000 times larger than the backscattering in the radar direction (Mie-effect; Doviak, 1984c, p. 28). The Mie regime is much more complicated than the other two regimes. This is due to the fact that in the Mie regime constructive and destructive interferences significantly influence the scattered signals. As a result, the radar cross section in the Mie region is an oscillating function (Fig. 2.8) that depends on the size parameter γ, which is why the Mie region is sometimes referred to as the *resonance region* (Fabry, 2017b, p. 12).

Attenuation

On its way through the atmosphere, electromagnetic radiation is often attenuated. *Attenuation* is any reduction in radiated power on its way from the radar to the target and back again. It does not matter whether the attenuation is caused by scattering, i.e., deflection in a direction other than to the radar, or whether the radiation is absorbed by particles along the way. Radar meteorologists usually distinguish between attenuation by gases and attenuation by hydrometeors. Attenuation by gases is dominated by oxygen and water vapor and has a smaller, but often non-negligible, effect on overall attenuation compared to hydrometeor attenuation. Attenuation is situation dependent and is influenced by humidity, whether precipitation occurs within the radar beam, and it depends on radar wavelength: long wavelength radiation is less affected than short wavelength radiation. Since attenuation can significantly change the power received by the radar depending on the wavelength, it must be taken into account whenever quantitative statements are to be derived from the measured radar reflectivity. However, since it depends strongly on the atmospheric state along the path, it is usually difficult to determine.

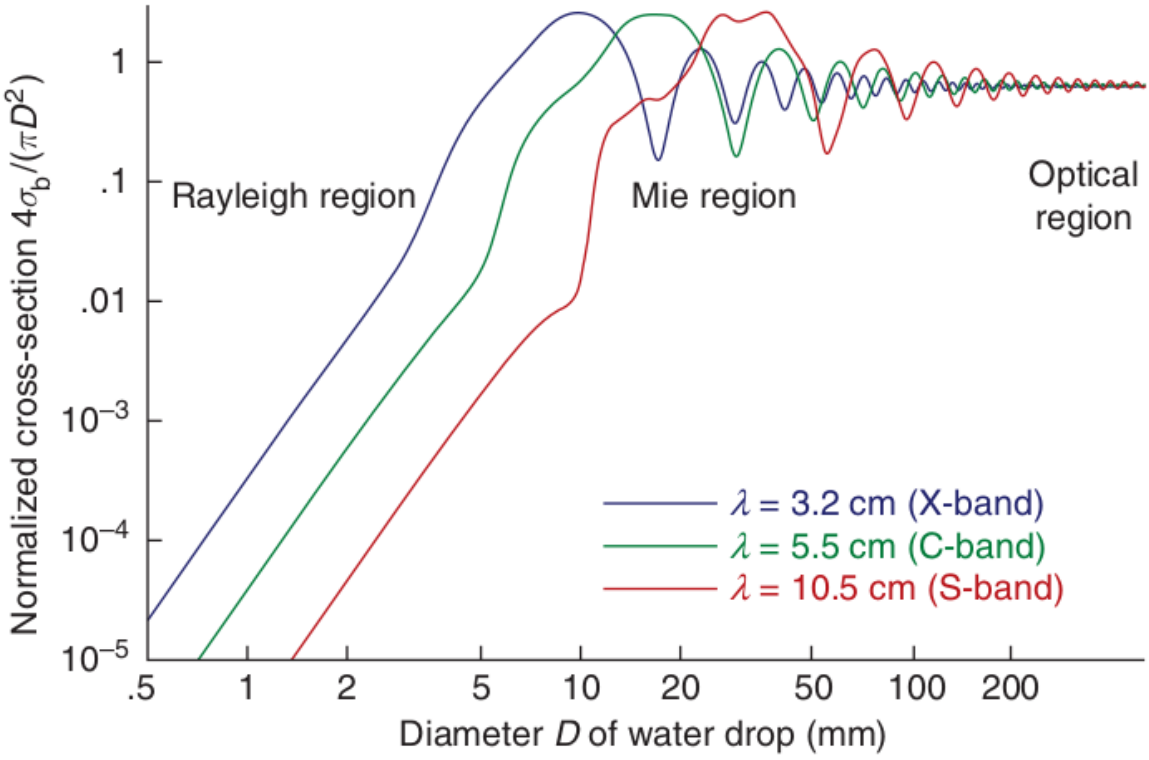

Figure 2.8: Normalized backscattering cross section of spherical water drops at three different radar wavelengths. From "Radar meteorology Principles and Practice" by Fabry (2017a), reproduced with permission of Cambridge University Press through PLSclear.

2.2.4 Radar Equation

Radar devices are not only able to determine the location of the target object, but can also measure the strength of the returning signal, which can provide information about the characteristics of the targets. However, not only the target influences the returning signal, but also many other parameters, such as the propagation of the beam in space, certain device parameters, or the transmitting power. All these factors can be related with an equation: the radar equation.

Radar equation for point targets

The derivation of the radar equation for point targets follows Rinehart (1997d, p. 65–69), Detlefsen et al. (1989b, p. 10–12) and Rogers and Yau (1989b, p. 187–188).

When a radar with an isotropic antenna emits a pulse of energy, that energy radiates into space and forms a spherically expanding shell with a surface area of $4\pi r^2$, where r is the distance from the radar. The power density S (power per unit area) is then simply the transmitted power P_t divided by this area

$$S = \frac{P_\mathrm{t}}{4\pi r^2} \,. \tag{2.26}$$

This is only valid for an isotropic antenna. Real radar antennas usually focus the power in the main beam direction. The power increase along the main beam path is described by the antenna gain G, as defined in Eq. (2.17). Therefore, for non-isotropic radar antennas, the power density along the main beam path changes to

$$S = \frac{GP_\mathrm{t}}{4\pi r^2} \,. \tag{2.27}$$

The fraction of the transmitted power that is scattered back to the radar is defined by the radar cross section σ, as explained in the previous section. The power scattered back from the target towards the radar P_σ is then

$$P_\sigma = \frac{G\sigma P_\mathrm{t}}{4\pi r^2} \,. \tag{2.28}$$

This scattered energy in turn forms a spherically expanding shell with the same surface area $4\pi r^2$, reducing the power density arriving at the radar by exactly this amount. The power received by the radar P_r additionally depends on the effective area A_e of the antenna

$$P_\mathrm{r} = \frac{A_\mathrm{e}\sigma G P_\mathrm{t}}{(4\pi r^2)^2} \,. \tag{2.29}$$

Finally, one can take advantage of the fact that the radar wavelength λ, the effective antenna area A_e, and the antenna gain G are related to each other

$$A_\mathrm{e} = \frac{G\lambda^2}{4\pi} \,, \tag{2.30}$$

which then means for the power received at the radar

$$P_\mathrm{r} = \frac{\lambda^2 \sigma G^2 P_\mathrm{t}}{(4\pi)^3 r^4} \,. \tag{2.31}$$

This is the radar equation for point targets.

Radar equation for distributed targets

The derivation of the radar equation for distributed targets follows Rinehart (1997e, p. 81–87) and Rogers and Yau (1989b, p. 188–189).

In reality, a radar beam rarely hits a single target. Instead, the radar beam covers a volume that depends on the distance to the radar, and usually covers several targets at once. Therefore, it is not

the radar cross section of a single target that determines the backscattered power but the total radar cross section σ_t of all targets within the volume. This is calculated as the sum over the radar cross sections σ_i of all targets in a unit volume Vol, multiplied by the actual radar beam volume V

$$\sigma_t = V \sum_{Vol} \frac{\sigma_i}{Vol} \,. \tag{2.32}$$

Of course, this only applies to beams that are uniformly filled with objects. This is an assumption frequently made in radar meteorology, which often does not hold true in reality. For large radar beam volumes, for example from space-based radars, non-uniform beam filling can actually lead to significant biases (Nakamura, 1991). Following Eq. (2.32) to calculate the total radar cross section, the actual radar beam volume is needed. In principle, the radar beam can be defined as a cone with a beamwidth ω and a length $l = c\tau$ corresponding to the pulse length, which can be calculated from the pulse duration τ and the speed of the light c. This would assume that the entire power of the beam is uniformly distributed in the beam. However, the power decreases away from the center of the cone. By definition, the power at the beamwidth is only *half* of the power at the center of the beam. A better approach, which takes into account the power distribution within the radar beam, is the assumption of a Gaussian beam pattern. According to Probert-Jones (1962), the radar beam volume under this assumption can be expressed as

$$V = \frac{\pi r^2 \omega^2 l}{16 \ln(2)} \,, \tag{2.33}$$

where ω is the beamwidth, and it was assumed that vertical and horizontal beamwidths are equal.

What has not been considered yet are possible power losses. These can be e.g. losses within the radar or losses during beam propagation due to attenuation. These losses can be described by one (or more, if one wants to break down the losses individually) loss function. Here, we distinguish between the attenuation loss l_a and other losses l_b. If we substitute the total radar cross section σ_t from Eq. (2.32) instead of a single point radar cross section σ together with the beam volume Eq. (2.33) and the loss functions l_a and l_b into the radar equation for point targets (Eq. 2.31), we obtain a radar equation for distributed targets, which is defined as

$$P_r = \frac{\lambda^2 G^2 P_t \omega^2 h \sum_{Vol} \frac{\sigma_i}{Vol} {l_a}^2 l_b}{1024 \ln(2) \pi^2 r^2} \,. \tag{2.34}$$

The one-way loss factor l_a appears quadratic in this equation because the beam must travel the distance r twice – once to the target and then back to the radar.

Radar reflectivity η

The only parameter in Eq. (2.34) that is determined by the actual targets (which is usually the interesting part) is the sum of the radar cross sections $\sum_{Vol} \sigma_i$. This part is called *reflectivity* (η) and expressed following Rinehart (1997e, p. 87) as

$$\eta = \sum_{Vol} \frac{\sigma_\mathrm{i}}{Vol} \,. \tag{2.35}$$

Radar reflectivity factor z

For spherical particles that are small compared to the wavelength, i.e., Rayleigh scatterers, the radar cross section can be expressed by Eq. (2.24). This means that the radar reflectivity η depends on the radar wavelength λ

$$\eta = \frac{\pi^5}{\lambda^4} |K|^2 \sum_{Vol} \frac{D_\mathrm{i}^6}{Vol} \,. \tag{2.36}$$

This is impractical, because most of the time the meteorologist is interested in the properties of the target – independent of the radar used. For this reason, the *radar reflectivity factor* z_fac was introduced, which depends solely on the properties of the target and is expressed following Rinehart (1997e, p. 89) and Rogers and Yau (1989b, p. 190) as

$$z_\mathrm{fac} = \sum_{Vol} \frac{D_\mathrm{i}^6}{Vol} = \int_0^\infty N(D) D^6 \,\mathrm{d}D \,. \tag{2.37}$$

$N(D)\,\mathrm{d}D$ is the number of particles per unit volume with sizes at $\mathrm{d}D$. $N(D)$ is referred to as the particle size distribution (PSD). Since the meteorological targets of interest usually have sizes in the millimeter range, z_fac is usually expressed in units of $\mathrm{mm}^6\,\mathrm{m}^{-3}$.

The radar equation is then

$$P_\mathrm{r} = \frac{G^2 P_\mathrm{t} \omega^2 l \pi^3 |K|^2 z_\mathrm{fac} {l_\mathrm{a}}^2 l_\mathrm{b}}{1024 \ln(2) \lambda^2 r^2} \,. \tag{2.38}$$

Equivalent radar reflectivity factor z_e

Equation (2.38) is valid only if the beam is uniformly filled, all particles scatter in the Rayleigh regime, and $|K|^2$ is constant for all illuminated particles. In reality, of course, this is usually not the case. To get around this problem, radar meteorologists use the *equivalent radar reflectivity factor* z_e instead of z_fac (Rinehart, 1997e, p. 94–95)

$$P_\mathrm{r} = \frac{G^2 P_\mathrm{t} \omega^2 l \pi^3 |K|^2 z_\mathrm{e} {l_\mathrm{a}}^2 l_\mathrm{b}}{1024 \ln(2) \lambda^2 r^2} \,, \tag{2.39}$$

where $|K|^2$ is the dielectric factor of liquid water (0.93). This is the radar reflectivity factor that *would* be measured if all scatterers were liquid Rayleigh scatterers and uniformly distributed within the beam. The equivalent radar reflectivity factor is commonly used to quantify the contribution of all targets measured in a radar beam volume.

Final expression of the radar equation

For a given radar, most of the parameters in Eq. (2.39) are constants. They can be calculated once and combined into the hardware-dependent radar constant C. This leads to a much simpler form of the radar equation

$$P_\mathrm{r} = \underbrace{C}_{\text{Constants}} \underbrace{\frac{{l_\mathrm{a}}^2}{r^2}}_{\text{Path}} \underbrace{|K|^2 z_\mathrm{e}}_{\substack{\text{Target}\\ \text{properties}}} \tag{2.40}$$

Equation (2.40) is called the general radar equation for distributed targets or sometimes simply the weather radar equation. This equation relates all the parameters that affect signal power on the way to and from the target, making it the most important equation in radar meteorology. The equation is used to quantify the contribution of the targets hit to the power received. To do this, the equation only needs to be solved for z_e. However, the range of values that z_e covers for typical weather situations spans many orders of magnitude. In order to make the range of values more manageable, it is often expressed on a logarithmic scale, indicated by Z_e

$$Z_\mathrm{e}[\mathrm{dBZ}] = 10 \log_{10} \left(\frac{z_\mathrm{e}}{\mathrm{mm}^6\,\mathrm{m}^{-3}} \right) . \tag{2.41}$$

For simplicity, I will use "reflectivity" in the remainder of this work when referring to the equivalent radar reflectivity factor Z_e in logarithmic units.

2.2.5 Polarization

The electric and magnetic fields of electromagnetic radiation oscillate in certain spatial directions. The direction of oscillation of the electric field determines the so-called *polarization* of the radiation. Most of the time, electromagnetic radiation is unpolarized; it consists of a random mixture of electromagnetic waves oscillating in different directions. However, it is possible to align the electromagnetic waves, or rather, to allow only waves to pass that oscillate in a particular spatial direction. This is called polarized radiation. For example, most conventional radars transmit and receive horizontally polarized radiation, meaning that when the radar is pointed at the horizon, the electric field of the outgoing electromagnetic radiation oscillates in a horizontal plane. Some radars emit horizontally polarized radiation, but can receive both horizontal and vertical polarization. The MIRA-35 Ka-band radar at the MIM is an example of such a radar. Other radars are so-called *dual-polarization* radars, which both transmit and receive horizontally and vertically polarized radiation. The advantage of polarized radar radiation is that further particle properties can be derived from the amount of horizontal or vertical polarization, or from the change in polarization.

Differential reflectivity Z_{DR}

The differential reflectivity Z_{DR} is defined as the difference between the measured horizontal and vertical polarization signal, following Rinehart (1997f, p. 209)

$$Z_{DR} = 10 \log_{10} \left(\frac{z_{hh}}{z_{vv}} \right) = Z_{hh} - Z_{vv} \,, \tag{2.42}$$

where z_{hh} is the equivalent reflectivity factor received with a horizontal polarization from a transmitted signal of horizontal polarization (hence the two "h" indices), and z_{vv} is the equivalent reflectivity factor for transmitted and received signals in vertical polarization. Z_{hh} and Z_{vv} are the corresponding reflectivities in units of dBZ. Unlike the normal reflectivity Z_e, Z_{DR} is independent of particle concentration, since an increase in particle concentration would simply increase z_{hh} and z_{vv} proportionally. This makes differential reflectivity a great variable for describing the aspect ratio of the particles measured. For flat and horizontally oriented particles, one would expect a higher return signal in the horizontal polarization and thus $Z_{DR} > 0\,\text{dB}$. For perfectly spherical particles, Z_{DR} would be 0 dB.

Linear depolarization ratio L_{DR}

Another commonly used variable is the *linear depolarization ratio* L_{DR}. This variable is very similar to differential reflectivity in that it is also calculated from the difference between the received signals in horizontal and vertical polarization, following Rinehart (1997f, p. 207)

$$L_{DR} = 10 \log_{10} \left(\frac{z_{hh}}{z_{hv}} \right) = Z_{hh} - Z_{hv} \,, \tag{2.43}$$

However, unlike differential reflectivity Z_{DR}, only a pulse with horizontal polarization is transmitted, so the received signal with vertical polarization was in fact originally a horizontally polarized pulse – the *depolarization* is measured. For perfect spheres (which have no depolarization effect), z_{hv} is zero and thus L_{DR} approaches $-\infty$. For long, thin targets, L_{DR} reaches 0 dB. L_{DR} is also independent of particle concentration. It is often used to detect the melting layer, since melting particles tend to have a strong depolarizing effect.

Specific differential phase shift K_{DP}

The speed at which an electromagnetic wave propagates through a medium depends on the refractive index of that medium. This means that a wave traveling through a medium with a higher refractive index (e.g., through a drop of water) is slower and therefore performs more wave oscillations than a wave traveling through a medium with a lower refractive index. This results in a phase shift between the two waves. Applying this concept to the waves in horizontal and vertical polarization, a phase shift between these two differently polarized waves would occur exactly when the hit particles are non-spherical. A group of flattened raindrops, for example, would cause

a measurable phase shift between horizontal and vertical polarized waves. This principle has been nicely explained and visualized by Kumjian (2018, p. 38–41). One half of the range derivative of the phase shift between horizontally and vertically polarized wave is called specific differential phase shift K_{DP}, defined following Kumjian (2018, p. 4) as

$$K_{\mathrm{DP}} = \frac{\Delta\phi_{\mathrm{dp}}}{2\Delta r}\,, \tag{2.44}$$

where $\Delta\phi_{\mathrm{dp}}$ is the differential phase shift between vertically and horizontally polarized wave per radial range unit Δr. The factor 2 results from the fact that $\Delta\phi_{\mathrm{dp}}$ is measured as the two-way differential phase shift – towards the target and back to the radar. K_{DP} is affected by number concentration, size, and relative permittivity of non-spherical particles. Also, unlike all other radar variables, K_{DP} is not affected by attenuation because it is based on measurements of phase, not power.

Co-polar correlation coefficient ρ_{hv}

Another frequently used polarization quantity is the co-polar correlation coefficient ρ_{hv}. ρ_{hv} describes the correlation between the received co-polar signals at horizontal and vertical polarizations. This measure is typically close to 1. Whenever there is a high diversity of tumbling particles with varying aspect ratios, types (e.g., ice or liquid), or orientations, this will decrease ρ_{hv} (Kumjian, 2018, p. 41).

Often, only the combination of several radar quantities makes a clear statement about the type of measured particles possible. For example, in a mixture of rain and hail, Z_{e}, Z_{DR}, and L_{DR} will be dominated by the large spherical hail particles, leading to large Z_{e} values and to Z_{DR} and L_{DR} values of 0 dB. Information about the rain in this mixture is not possible from these variables alone. K_{DP} however, is not influenced by the spherical hail. If, for example, K_{DP} would increase in the presence of Z_{DR} near 0 dB, this suggests an increasing rain fraction in the presence of hail. The combination of polarimetric quantities is used for many different applications, for example, to classify hydrometeors or to for improvements of quantitative precipitation estimation (QPE) by better constraining the shape or PSD of precipitation.

2.2.6 Dual-Wavelength

The only radar variable that is directly related to particle size is the reflectivity Z_{e}. Unfortunately, the reflectivity is also influenced by other parameters, such as particle number concentration, type, phase, or density of the particles. To constrain the particle sizes, a second radar with a different wavelength is required. This is called the dual-wavelength concept. By definition, the reflectivity Z_{e} is independent of the radar wavelength, but this is only valid if the scattering takes place in the Rayleigh regime. For scattering outside the Rayleigh regime, the measured reflectivities are no longer wavelength independent. This fact can be exploited: if two radars with different wavelengths measure different reflectivities, the observed particles must have sizes

that scatter outside the Rayleigh regime for at least one of the radars. This can be used, for example, to detect hail. At wavelengths of 10 cm and 3 cm raindrops at millimeter size scatter according to the Rayleigh regime for both radars (Raghavan, 2003, p. 25). Hail, on the other hand, is larger, and Mie scattering occurs for the 3 cm radar, which reduces the measured reflectivity. The 10 cm radar, on the other hand, still measures in the Rayleigh regime. Thus, a difference in the measured reflectivities suggests hail. This approach can also be used for smaller particles if shorter wavelengths are used. In this work, wavelengths of 5 cm and 0.8 cm are combined. A radar with a wavelength of 0.8 cm is categorized as a "cloud radar", and particles with a size larger than a few 100 µm, i.e. larger cloud droplets or drizzle, already scatter according to the Mie regime. Therefore, at these frequencies, the difference in measured reflectivities is sensitive to the size of cloud and precipitation particles, and can be used to detect changes in particle diameters, e.g., due to particle growth processes, melting, or other processes that influence the particle size. The logarithmic difference in reflectivity for two radars with different wavelengths is called the dual-wavelength ratio dwr, defined according to Hogan et al. (2012) as

$$dwr = Z_{\mathrm{e},\lambda 1} - Z_{\mathrm{e},\lambda 2}\,, \tag{2.45}$$

where $Z_{\mathrm{e},\lambda 1}$ and $Z_{\mathrm{e},\lambda 2}$ are the reflectivities of the two radars with wavelengths λ_1 and λ_2 respectively ($\lambda_1 > \lambda_2$).

Chapter 3

Data and Methodology

This chapter includes sections previously published in Atmospheric Measurement Techniques (Sect. 3.1 - 3.6) by Köcher et al. (2022b) and in Atmospheric Chemistry and Physics (Sect. 3.7) by Köcher et al. (2022a).

In this work, the benefit of polarimetric radar observations is investigated to evaluate numerical weather predictions with different cloud microphysics schemes. For this purpose, radar observations were collected over 30 days using two radars of different frequencies, and numerical weather predictions were performed using five different microphysics schemes of varying complexity. In this chapter, the underlying data set, and all applied methods are described. In Sect. 3.1, the observational dataset is described, as well as the radar characteristics. The NWP model, its domain, and key settings are described in Sect. 3.2. The microphysics schemes are explained in detail in Sect. 3.3. To compare the NWP model output with the radar observations, a radar forward operator capable of simulating polarimetric radar signals was used (Sect. 3.4). The radar data are originally available on a spherical grid, whereas the model data are available on a Cartesian grid. To ensure a fair comparison, the grids are matched by interpolation to a common Cartesian grid taking into account the radar beam characteristics (Sect. 3.5). Since the focus of this work is on convective weather, an automatic cell tracking algorithm is applied (Sect. 3.6). This algorithm identifies convective cells based on reflectivity thresholds and can be applied to simulated and observed reflectivities in the same way. Part of this work focuses on high-impact weather, i.e., hail or heavy precipitation events. To define such events, a hydrometeor identification (HID) algorithm is applied (Sect. 3.7).

In total, 30 convective days were observed and simulated over 2 years in 2019 and 2020. The majority of these days were in spring and summer. For all of them, convective precipitation was forecasted. A table listing the dates can be found in Appendix A.

3.1 Radar Data

The observational data basis is provided by two research radar systems in the area of Munich, Germany, at C- and Ka-band frequencies, and a complementary second C-band radar operated by the DWD (Fig. 3.1). C-band radars are typically used for precipitation measurements, while Ka-band radars are typically used for cloud observations. The combination of both allows to measure the dual-wavelength ratio, and thus provides a measure of the hydrometeor sizes present in precipitating convective clouds.

The C-band research radar POLDIRAD (Schroth et al., 1988), operated by the German Aerospace Center (DLR), is located in Oberpfaffenhofen southwest of Munich. At 23 km distance, the research Ka-band radar MIRA-35 is operated by the Meteorological Institute Munich (MIM) of the Ludwig-Maximilians-Universität (LMU) in the center of Munich. The third radar is an operational C-band radar located in Isen at a distance of 40 km to the MIRA-35 radar.

All three radars are polarimetric Doppler radars. POLDIRAD and the ISEN radar are fully polarimetric, sending out electromagnetic waves with horizontal and vertical polarization. Both radars receive the co-polar components backscattered by atmospheric targets. Therefore, polarimetric variables such as differential reflectivity (Z_{DR}) or specific differential phase (K_{DP}) are available. POLDIRAD additionally receives the cross-polar components, and hence measures the linear depolarization ratio (L_{DR}). The MIRA-35 radar is a single-polarization ground-based cloud radar manufactured by METEK GmbH (Görsdorf et al., 2015). It only transmits horizontally polarized waves but receives co- and cross-polar components. Thus, it is possible to measure L_{DR} in addition to the standard reflectivity.

POLDIRAD and MIRA-35 are two research radars without any operational obligations. This allows for synchronized and targeted scan patterns of convective clouds and precipitation on demand. The absolute calibration of reflectivity Z_{e} of POLDIRAD is estimated to have an error of ± 0.5 dB from calibration with an external electronic calibration device (Reimann, 2013), while the reflectivity error of MIRA-35 is estimated to be ± 1.0 dB (Ewald et al., 2019). POLDIRAD Z_{DR} is estimated to have an offset of about 0.15 dB from measurements in a liquid cloud layer, where Z_{DR} near 0 dB is to be expected. This offset is corrected before any of the subsequent analysis is done. The ISEN radar is part of the DWD operational radar network with a fixed observation strategy. For a complete description of the measurement strategy, refer to Helmert et al. (2014). More radar characteristics and configurations can be found in Table 3.1. This setup allows for dual-wavelength and polarimetric measurements of convective clouds and precipitation in the area of Munich.

Two measurement strategies have been applied. For spatial coverage, only data of the operational DWD ISEN radar are utilized in scan strategy A. The ISEN radar is running operationally a volume plan position indicator (PPI) scan every 5 min at 11 elevations from 0.5° to 25°, and over the whole azimuth circle of 360°. This provides a good spatial coverage at a high temporal resolution. In Fig. 3.1, the green circle depicts the area that is covered by this strategy. In strategy B, POLDIRAD and MIRA-35 are used for coordinated and targeted scan patterns of the same convective cloud. Strategy B starts with a POLDIRAD overview scan in PPI mode:

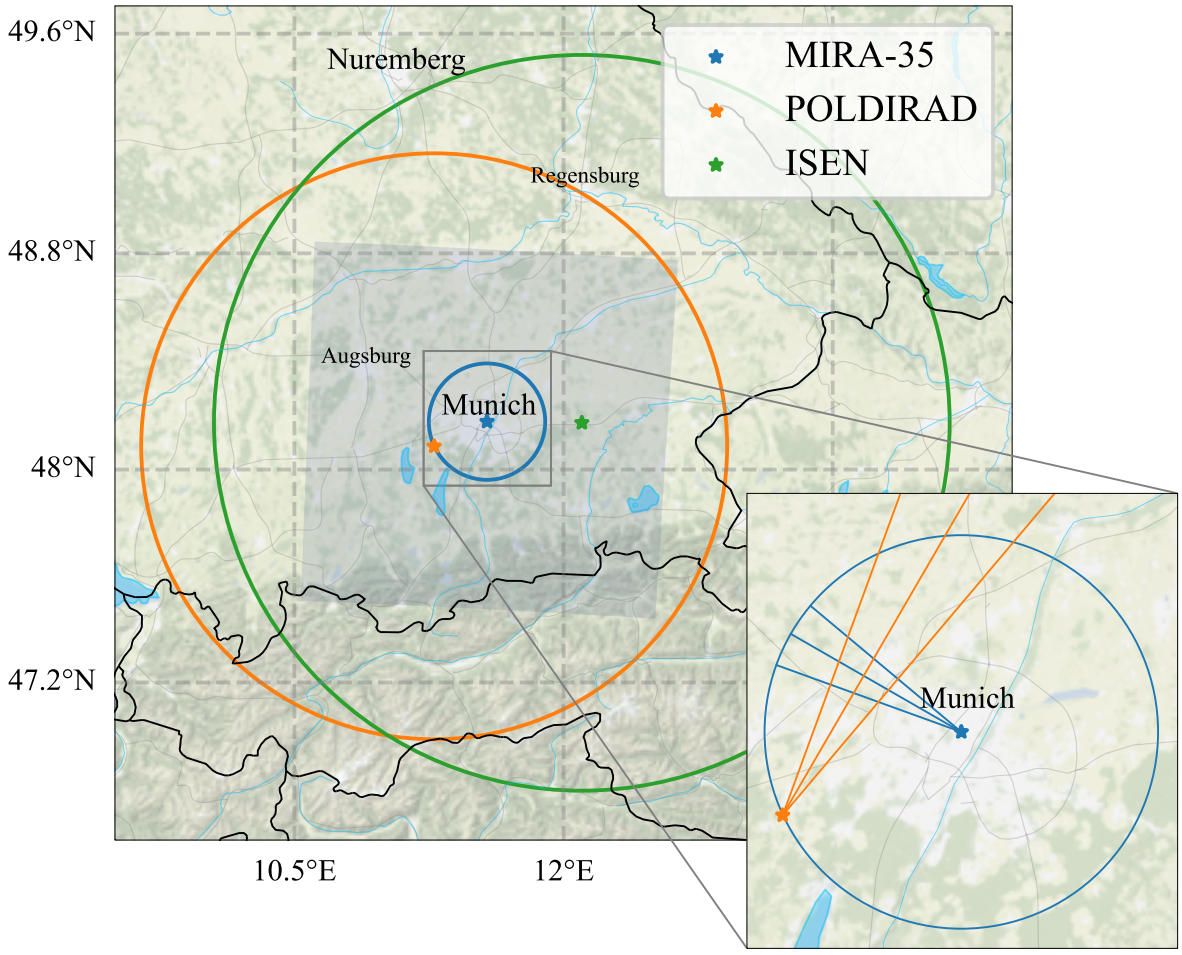

Figure 3.1: Radar locations and model domain. The filled blue area shows the model domain. Stars show the radar locations and the circles show the radar range around each radar. The straight blue and orange lines visualize range height indicator (RHI) scans executed by the MIRA-35 and POLDIRAD radar. Background map tiles by Stamen Design (http://stamen.com, last access: April 13, 2023), distributed under the Creative Commons Attribution (CC BY 3.0) license. Background map data by OpenStreetMap (http://openstreetmap.org, last access: April 13, 2023; © OpenStreetMap contributors YEAR. Distributed under the Open Data Commons Open Database License (ODbL) v1.0.). Roads, rivers, and lakes made with Natural Earth (https://www.naturalearthdata.com, last access: April 13, 2023).

the elevation angle is kept constant, and the azimuth angle is varied. After manually choosing a convective cell from this overview PPI, both radars start to execute three fast scans towards this convective target cloud in the range height indicator (RHI) scan mode; i.e., the azimuth angle is kept constant, while the elevation angle is varied. The first scan is executed exactly towards the direction that was chosen; one is directed to 2° azimuth angle to the left; and one is directed to 2° azimuth to the right. This scan mode is referred to as sector range height indicator (S-RHI). The

Table 3.1: Radar characteristics. For the ISEN radar, the precipitation scan at 1.5° elevation was referenced. For the full configuration of the volume scan, see Helmert et al. (2014).

	POLDIRAD	MIRA-35	ISEN
City	Oberpfaffenhofen	Munich	Isen
Location	48.087°N, 11.279°E	48.148°N, 11.573°E	48.175°N, 12.102°E
Wavelength	5.45 cm	0.85 cm	5.3 cm
Frequency	5.5 GHz	35.2 GHz	5.66 GHz
Beamwidth	1°	0.6°	0.9°
Range	120 km	24 km	150 km

nine intersection profiles resulting from these S-RHIs give an idea about the variation within the cloud and compensate for potential pointing inaccuracies. In Fig. 3.1, the six straight lines (three orange and three blue) visualize these RHI scans. After each S-RHI scan, the azimuth direction is adjusted slightly, according to the projected movement of the cell. This cell movement is projected using two previous POLDIRAD overview PPI scans by calculating the displacement at which the cross-correlation between the two PPI images is at maximum. After a few minutes, the S-RHI scans are stopped (manual), and the procedure starts over with another overview PPI scan. This strategy allows for targeted dual-wavelength observations of convective clouds in high vertical resolution over a significant fraction of their lifetime.

In total, we collected data of strategy B over 5 convective days during summer 2019. The strategy A comprises a larger data set. It consists of the same 5 convective days as well as 25 additional convective days during 2019 and 2020.

3.2 Numerical Weather Prediction Model

The simulations are performed using version 4.2 of the Weather Research and Forecasting (WRF; Skamarock et al., 2019) model. Initial and lateral boundary conditions are provided by reanalysis data at 0.25° grid spacing from the Global Forecast System (GFS; National Centers For Environmental Prediction/National Weather Service/NOAA/U.S. Department Of Commerce, 2015), available every 6 h and with hourly forecast data in between. Horizontally, the setup includes a parent Europe domain (3750 km by 3750 km), a two-way nested Germany domain (442 km by 442 km), and a two-way nested Munich domain (144 km by 144 km). The vertical domain extends from the surface to 5 hPa at 40 vertical levels. The nesting ratio is 5:1 with the Europe domain at a horizontal grid spacing of 10 km, the Germany domain at 2 km, and the Munich domain at 400 m. Currently, operational limited area weather models operate at 2 km grid spacing (e.g., 2.8 km in COSMO-DE of the German Weather Service; Baldauf et al., 2011), which means the inner domain has a resolution that is effectively about 5 times higher and should represent the future of operational limited area weather models, most likely including advanced microphysics handling. The Munich domain is centered over the MIRA-35 instrument (48.15°N, 11.57°E). It

covers the MIRA-35 range (48 km) and an edge region of an additional 48 km around. All analyses are performed on the innermost Munich domain excluding the edge region, only considering the MIRA-35 range (Fig. 3.1). This area is completely covered by the POLDIRAD and ISEN radar observations. Each simulation consists of 6 h spin-up and 24 h simulation time. The spin-up always starts at 18:00 UTC (Coordinated Universal Time) on the previous day, which corresponds to 20:00 LT (Local Time). Thus, the 24 h forecast exactly covers the day of interest (00:00 to 24:00 UTC). The dynamics can freely evolve during the simulation time. The parent Europe domain is nudged towards the global GFS data, by appending a nudging term to the prognostic equations for humidity, temperature, and wind that "nudges" the WRF grid value towards the closest GFS grid value for each grid point of the Europe domain above the planetary boundary layer (grid analysis nudging). The inner Germany and Munich domain are not nudged. All days are simulated with five different microphysics schemes. Hence, there are five simulations available for each of the convective days, and the simulation setups only differ in the choice of the microphysics scheme. Other physics options include the Noah land surface model (Ek et al., 2003, Chen and Dudhia, 2001), the MYNN2 planetary boundary layer scheme (Mellor–Yamada scheme by Nakanishi and Niino; Nakanishi and Niino, 2006), and the RRTMG radiation scheme (Rapid Radiative Transfer Model for General Circulation Models; Iacono et al., 2008). For any other options, please refer to the WRF namelist that is provided in Appendix E.

3.3 Description of the Microphysics Schemes

Five different microphysics schemes are employed: three two-moment bulk schemes, as well as one spectral bin scheme and the P3 scheme (Table 3.2). The FSBM scheme explicitly resolves the PSD with a number of bins, while all other schemes generally represent the PSD by a gamma function

$$N(D) = N_0 D^{\mu} \mathrm{e}^{-\Lambda D}\,, \tag{3.1}$$

where N_0 is the intercept parameter, D is the particle maximum diameter, μ is the shape parameter, and Λ is the slope parameter. The only exception is snow in both Thompson schemes following a bimodal gamma function as described below.

Table 3.2: The employed microphysics schemes.

Name	WRF-ID	Publication
Thompson 2-mom	8	Thompson et al. (2008)
Morrison 2-mom	10	Morrison et al. (2009)
Thompson aerosol-aware	28	Thompson and Eidhammer (2014)
Fast spectral bin (FSBM)	30	Shpund et al. (2019)
Predicted Particle Properties (P3)	50	Morrison and Milbrandt (2015)

The mass–size relationships are given by a power law,

$$m = aD^b \,, \tag{3.2}$$

where m is the particle mass, and D is the particle diameter. The parameters a and b depend on the hydrometeor class and the scheme used, and are described below.

a. *Thompson 2-mom.* The Thompson 2-mom bulk scheme predicts integral moments of the PSD for five hydrometeor species: cloud ice, cloud water, rain, snow, and graupel. Rain and cloud ice are two-moment species which predict mass mixing ratio and number concentration. Snow, graupel, and cloud water are one-moment; i.e., only the mass mixing ratio is predicted.

   The PSDs of rain, cloud ice, graupel, and cloud water are represented by gamma distributions Eq. (3.1). For rain, graupel, and cloud ice $\mu = 0$; i.e., the PSD is an exponential function. Snow and cloud ice have a fixed non-zero μ.

   The mass–size relation follows a power law (Eq. 3.2). Rain, graupel, cloud ice, and cloud water are assumed to be spherical ($b = 3$), with the parameter a depending on the hydrometeor bulk density ρ_b, with

$$a = \rho_\mathrm{b} \frac{\pi}{6} \,. \tag{3.3}$$

   The bulk density of rain, graupel, cloud ice, and cloud water is constant and size-independent.

   Snow is treated differently in the Thompson 2-mom scheme compared to other bulk schemes. Instead of the simple gamma function shown in Eq. (3.1), a bimodal gamma distribution (sum of an exponential and a gamma function) from Field et al. (2005) that is dependent on temperature is used. Snow is not considered to have a constant density across the PSD; the mass is proportional to D^2 ($b = 2$) to better fit observations. The parameter a of the mass–size relation is constant at $a = 0.069$.

b. *Thompson aerosol-aware.* The Thompson aerosol-aware bulk scheme (Thompson and Eidhammer, 2014) is very similar to the older version (Thompson et al., 2008) described in the previous section but includes some changes. While the older version of the Thompson 2-mom scheme only uses two two-moment species (rain and cloud ice) and a prescribed number of cloud droplets, the newer version includes activation of aerosols as cloud condensation nuclei (CCN) and ice nuclei (IN). Therefore, it explicitly predicts the droplet number concentration of cloud water and two aerosol variables (CCN and IN).

c. *Morrison 2-mom.* The Morrison 2-mom bulk scheme predicts integral moments of the PSD for five hydrometeor species: cloud ice, cloud water, rain, snow, and graupel. All are double-moment species. PSDs follow a general gamma distribution (Eq. 3.1). Rain, cloud ice, snow, and graupel have shape parameter $\mu = 0$, again transforming the PSDs into an exponential distribution. For cloud water, μ is a function of droplet number concentration, following Martin et al. (1994). All particles are assumed to be spherical with fixed and size-independent bulk densities.

d. *FSBM.* In contrast to the bulk schemes, a spectral bin scheme explicitly resolves the PSD by approximation with a number of independent size bins. This has the advantage that no prior assumption about the shape of the PSD is necessary. However, computational costs are much higher, as all microphysical processes are computed for each bin separately. In this study the FSBM is used that applies 33 mass-doubling bins; i.e., the mass of the bin i is twice the mass of the bin i-1. Five hydrometeor classes are included: cloud water, cloud ice, rain, graupel, and snow.

e. *P3.* The P3 scheme uses three bulk categories: rain, cloud water, and, unlike all the previous schemes, only a single ice category. Instead of predicting mixing ratio and number concentration for multiple ice categories, the P3 scheme predicts properties of this single ice category. Four prognostic ice mixing ratio variables are predicted: total ice mass, rime mass, rime volume, and number mixing ratio. Based on these variables, more properties are derived, such as rime mass fraction F_r (ratio of rime mass and ice mass mixing ratio) or rime density ρ_r (ratio of rime mass and rime volume mixing ratio). All PSDs follow a general gamma distribution (Eq. 3.1). For cloud droplets, the shape parameter μ follows observations of Martin et al. (1994). For rain, μ follows observations of Cao et al. (2008). For ice, μ follows observations of Heymsfield (2003).

   Mass–size relationships follow a power law (Eq. 3.2). The parameters a and b depend on the size of the ice. The scheme distinguishes between small ice, unrimed ice, partially rimed ice, and fully rimed ice (graupel/hail). Small ice and graupel are considered spherical ($b = 3$) with parameter a given by Eq. (3.3), where the ice bulk density ρ_b equals $917\,\mathrm{kg\,m^{-3}}$ for small ice and varies for graupel/hail.

   Unrimed ice, grown by vapor diffusion or aggregation, and partially rimed ice have an effective density that is generally less than that of an ice sphere ($b = 1.9$). The parameter a follows an empirical relationship from Brown and Francis (1995, $a = 0.0121\,\mathrm{kg\,m^{-3}}$) for unrimed ice and depends on the rime mass fraction F_r for partially rimed ice ($a = 0.0121/(1 - F_\mathrm{r})\,\mathrm{kg\,m^{-3}}$); i.e., a increases with the rime mass fraction. Rain and cloud water are considered spherical, with $b = 3$ and a following Eq. (3.3) and a bulk density ρ_b of $1000\,\mathrm{kg\,m^{-3}}$.

3.4 Radar Forward Operator

To compare the WRF model output against radar observations, version 3.33 of the "Cloud-resolving model Radar SIMulator" (CR-SIM; Oue et al., 2020) is used. CR-SIM is based on the T-matrix method to compute the scattering characteristics of hydrometeors and is able to simulate polarimetric and Doppler radar variables for several radar frequencies, including C-band and Ka-band that are used in this study. The variables include, among many others, the reflectivity (Z_e) and specific attenuation (A_s) at vertical and horizontal polarization, differential reflectivity (Z_DR), and specific differential attenuation (A_DP). Given that CR-SIM supports both C- and Ka-band frequencies, it is possible to simulate the dual-wavelength ratio (dwr) by performing the forward simulation for the C-band radar as well as the Ka-band radar. The dielectric constant of water is 0.92. Solid-phase hydrometeors are assumed to be dielectric dry oblate spheroids and are

represented as air in an ice matrix. The refractive index hence depends on the hydrometeor density and is computed using the Maxwell Garnett (1904) mixing formula. There are no mixed-phase particles simulated. This means mixed-phase radar signatures (for example the "bright band", Austin and Bemis, 1950) will not be reproduced by the simulation. In order to simulate polarimetric radar observables, a radar forward operator must assume particle shapes and particle orientation. The particle orientation assumptions are the same for all schemes. It is assumed that the particle orientations are 2D Gaussian-distributed with zero mean canting angle, as in Ryzhkov et al. (2011). The width of the angle distributions is specified for each hydrometeor class: 10° for cloud, rain, and ice and 40° for snow, unrimed ice, partially rimed ice, and graupel. Regarding the shape assumptions, cloud droplets are simulated as spherical (aspect ratio (ar) of 1), and raindrops are simulated as oblate spheroids with a changing axis ratio dependent on the drop size according to Brandes et al. (2002) in all schemes. For ice hydrometeor classes, the same aspect ratio assumptions are applied for all schemes except the P3 scheme: cloud ice is assumed as oblate with a fixed aspect ratio of 0.2. Snow is assumed as oblate with a fixed aspect ratio of 0.6. Graupel is assumed to be oblate with an aspect ratio that is changing from 0.8 to 1, dependent on the diameter according to Ryzhkov et al. (2011):

$$\begin{aligned} ar &= 1.0 - 0.02D \quad \text{if } D < 10\,\text{mm}\,, \\ ar &= 0.8 \qquad\qquad\ \ \text{if } D > 10\,\text{mm}\,. \end{aligned}$$

The P3 scheme does not provide the standard ice hydrometeor classes. Instead, the aspect ratio of small ice (spherical, fixed aspect ratio of 1), unrimed ice (oblate, fixed aspect ratio of 0.6), partially rimed ice (oblate, fixed aspect ratio of 0.6) and graupel (spherical, fixed aspect ratio of 1) is assumed by CR-SIM. This means in comparison to the other schemes that the P3 simulation deviates for small ice (aspect ratio of 1 in P3, while cloud ice in other schemes is assumed to have an aspect ratio of 0.2) and graupel (0.8–1 in other schemes, while graupel particles in P3 are assumed to have an aspect ratio of 1). Resulting differences in the radar signal are discussed in the results whenever it might influence the simulated radar signal.

3.5 Grid Matching and Attenuation Correction

Radar data and model output are available on different grids. To allow for a comparison, these grids must be matched first. In a first step, the model data are transformed to a spherical grid of the corresponding radar. For example, simulated MIRA-35 radar data are transformed to a spherical grid with a range resolution of about 31 m and a maximum range of 24 km. The transformation utilizes the source code radar_filter, which is available on the website of Stony Brook University, together with the CR-SIM source code (https://you.stonybrook.edu/radar/research/radar-simulators/). The radar_filter considers beam propagation effects; i.e., for the interpolation to a grid point of the target spherical grid, all Cartesian input grid points that are within the beamwidth are included with a weight depending on the distance to the radar volume center. If no Cartesian grid point falls into the radar beam, the nearest grid point is used. In the next step, attenuation correction

is applied along the beam. The correction is applied by subtracting the accumulated (along the range coordinate) simulated attenuation from the uncorrected reflectivity

$$Z_{\mathrm{corr,r}} = Z_{\mathrm{e,r}} - 2 \cdot \Delta r \cdot \sum_{i=0}^{i=r} A_{\mathrm{s,i}} \,. \tag{3.4}$$

Here, the simulated reflectivity without attenuation correction at range gate r is given by $Z_{\mathrm{e,r}}$. $A_{\mathrm{s,i}}$ is the simulated specific attenuation at range gate i, and Δr is the radar range resolution in meters. The factor 2 takes into account the fact that the beam travels twice through each grid box (from antenna to target and back). In the same way, the differential reflectivity Z_{DR} is corrected with the simulated differential attenuation A_{DP}.

In a last step, all data (model and radar) are transformed back to a Cartesian grid that exactly covers the Munich domain of the model (144 km by 144 km) with a 400 m by 400 m by 100 m (vertical) grid spacing. Only grid boxes within the lowest and highest radar beam are considered. All grid boxes below the lowest or above the highest beam are masked out. Simulated and measured radar signals are converted to a regular Cartesian grid using inverse range interpolation. This interpolation includes the four nearest data points, weighted by their distance $(1/\mathrm{distance})^2$.

The original horizontal model grid spacing is 400 m. The original DWD radar data is provided with bins every 250 m along the range axis and every 1° along the azimuth. The beamwidth is about 265 m at the closer domain edge, about 685 m at the domain center, and about 1100 m at the far edge. Both the radar and the model require a sufficient spatial sampling to observe a physical phenomenon like a strong precipitation cell. Here, this translates into the question of an effective resolution, which is coarser than the nominal resolution. Skamarock (2004) estimates the effective resolution of WRF to be 5–7 times the nominal resolution, which would result in around 2 km effective model resolution in this case. Given that a radar with a nominal sampling of around 700 m (at the domain center) also needs at least 2–3 samples of a precipitation cell to begin resolving its true intensity, the "effective resolution" of such observations seems to be in a comparable range.

3.6 Cell Tracking

This study focuses on convective clouds and precipitation. To identify and track convective cells in simulations and observations, the open-source Python package "TINT is not TITAN" (TINT; Raut et al., 2021) is used. TINT is based on TITAN (Thunderstorm Identification, Tracking, Analysis, and Nowcasting; Dixon and Wiener, 1993). Convective cells are identified using minimum thresholds for reflectivity (32 dBZ) and cell area (8 km^2); 32 dBZ is at a common magnitude to identify convective storms (e.g., Dixon and Wiener, 1993, Jung and Lee, 2015). Higher thresholds potentially miss moderate or weaker convective cells, while lower thresholds will misidentify more non-convective echoes as convective cells. A cell motion vector is found by calculating cross-correlation of the reflectivity field in the cell neighborhood of two subsequent time steps and a correction based on prior cell movement. Possible convective cell pairs are compared and

matched using an algorithm from TITAN that uses a cost function combining travel distance and volume change of the possible cell pairs. The cell tracking is applied to simulated and observed reflectivity of the ISEN radar only. The simulated and observed reflectivity from MIRA-35 and POLDIRAD is not used for cell tracking. This way it is ensured that there is one unique definition to locate convective cells and prevent varying cell definitions depending on the radar that is simulated. TINT is applied to the Cartesian grid in exactly the same way for model and radar data, by passing Py-ART grid objects (Helmus and Collis, 2016) created from the Cartesian grid data to TINT. More detailed information about TINT can be found in Raut et al. (2021), Fridlind et al. (2019) and Dixon and Wiener (1993). TINT does not deal with splits (one cell splits into multiple cells) or mergers (multiple cells merge into one cell), but it was specifically designed for the tracking of convective cells over large data sets and is straightforward to apply to this data (Fig. 3.2).

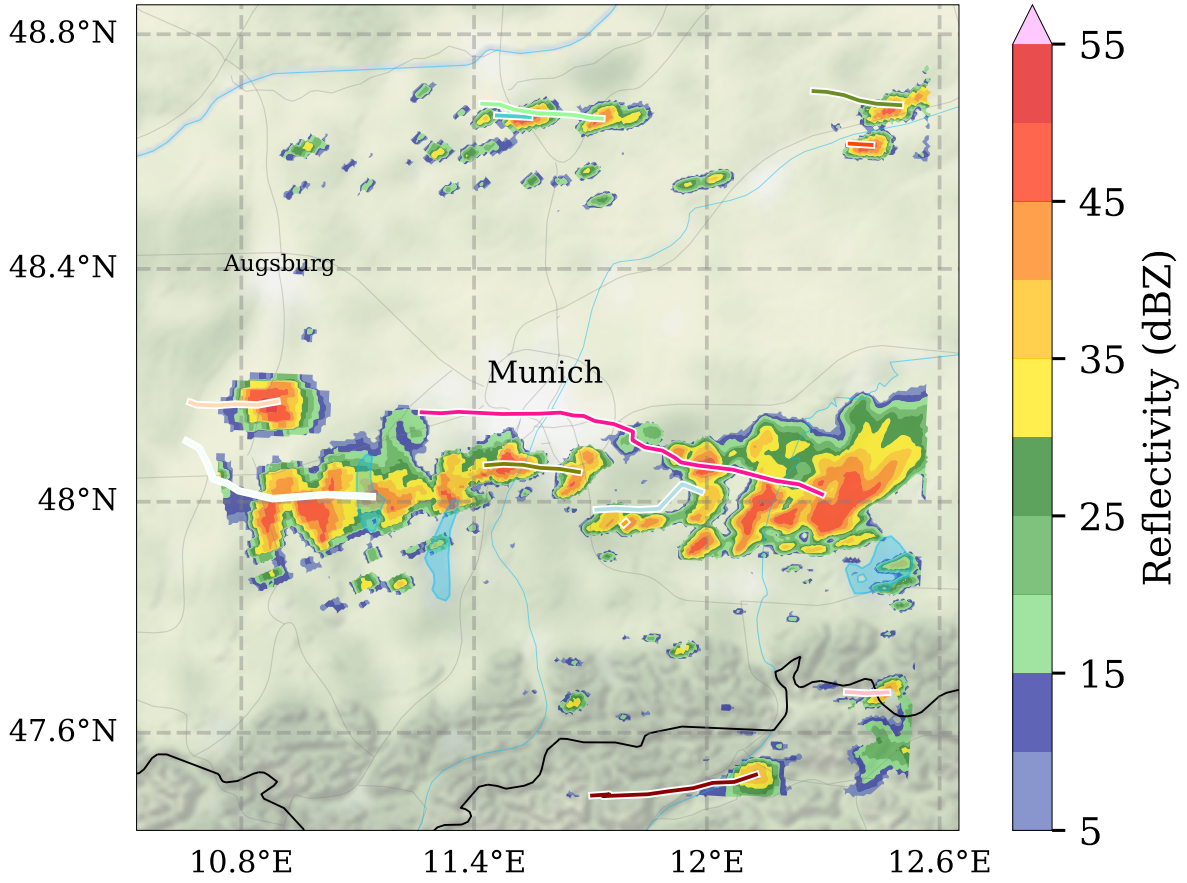

Figure 3.2: Example of cell tracking with TINT is not TITAN (TINT): colored background is the reflectivity simulated with the Weather Research and Forecasting (WRF) model and with the Cloud-resolving model Radar SIMulator (CR-SIM), and solid lines and numbers represent the TINT tracks and TINT cell identifier.

3.7 Hydrometeor Identification

Another focus of this work is high-impact weather events, i.e., hail and heavy rainfall events. To distinguish between, hail, rain, or any other hydrometeor type, a hydrometeor identification (HID) algorithm is required. Polarimetric radar signals can provide information on the type of hydrometeors present in the measurement volume. There are HID algorithms that use polarimetric radar signals to determine the dominant hydrometeor species. In this study, the algorithm of Dolan et al. (2013) for C-band radar is applied for this purpose. This algorithm uses a fuzzy logic approach (Zadeh, 1965) based on theoretical scattering simulations using the T-matrix (Barber and Yeh, 1975) and Mueller-matrix (Vivekanandan et al., 1991) from Dolan and Rutledge (2009), originally for X-band. Based on the polarimetric radar variable ranges derived from the T-matrix scattering simulations, the method defines fuzzy logic membership functions for each hydrometeor type. These functions are then used to calculate a score describing how well the input radar signals match a hydrometeor type. There are 10 different categories available. Drizzle and rain are combined into a common class, hereafter referred to as "rain". Of all the ice classes, technically, only the hail and graupel classes are of interest for high-impact weather. However, the microphysics schemes applied in this study do not provide exactly the same ice classes. Therefore, for a fair comparison, all ice classes are included into a common ice category. It is assumed that all these classes almost exclusively occur related to hail/graupel events during the summer study period. Thus, vertically aligned ice, wet snow, aggregates, ice crystals, high density graupel, low density graupel, hail, melting hail/big drops are combined and referred to as "ice". The HID algorithm is unable to distinguish between melting hail and big drops and therefore uses a common class for both. This class is considered to be part of the ice category because the melting hail/big drops classification typically always relates to hail events and is typically associated with very large reflectivities. For classification, the HID algorithm uses four radar quantities: reflectivity Z_e, differential reflectivity Z_{DR}, specific differential phase K_{DP}, and correlation coefficient ρ_{hv}. These variables are available from both the observed radar data set and the simulations after applying the CR-SIM radar forward operator. Accordingly, the HID algorithm is applied to both simulated and observed radar signals in the same way.

Chapter 4

Statistical Evaluation of Weather Predictions with Varying Cloud Microphysics

This chapter includes sections previously published in Atmospheric Measurement Techniques (Sect. 4.3.1 and 4.4) by Köcher et al. (2022b) and in Atmospheric Chemistry and Physics (Sect. 4.2 and 4.5) by Köcher et al. (2022a).

This chapter presents the main results of this work. The statistical evaluation is based on a dataset of 30 convection days, as presented in chapter 3. The first section presents a synoptic overview of these days, including stability metrics that describe the potential strength of convection (Sect. 4.1). In Sect. 4.2, the NWP model's performance is demonstrated with an example hail case. The influence of the cloud microphysics schemes on the model's ability to reproduce cloud macrophysical convective cloud properties, such as the strength or height of convective cell cores, is evaluated in Sect. 4.3. In Sect. 4.4 the model's ability to reproduce vertical profiles of polarimetric radar signatures is analyzed. This helps to identify issues of the microphysics schemes in specific microphysical aspects that translate into wrong polarimetric radar signatures. In Sect. 4.5, the influence of the microphysics schemes on the model's ability to simulate high-impact weather events, such as hail or heavy rainfall, is evaluated.

4.1 Synoptic Overview

The dataset used in this work consists of 30 days in 2019 and 2020. Most of the measurement days were in May, June, July, and August and only 5 of the measurement days were in April, September, or October. For all the 30 measurement days, convective showers or thunderstorms

were forecasted. A complete table of the measurement days can be found in Appendix A. This section describes the synoptic situation on these days.

4.1.1 Surface Winds

Figure 4.1 shows the surface winds during the 30 days of measurements and during a 30 year climatology. The measurements are 10 min surface winds from the DWD station "München Flughafen" (Deutscher Wetterdienst, 2023c). The overall picture of surface winds is similar. Westerly surface winds were measured most of the time, both in the climatology and during the 30 days of measurements. Differences can be seen in the proportion of easterly winds. While a significant fraction of about 20 % of the climatology winds are easterly and northeasterly winds, we almost never had easterly winds on the measurement days. Winds from easterly directions over Munich are usually associated with a high pressure system in the north that brings cold, dry air from the east to Munich. Cold, dry air is unfavorable for the development of thunderstorms, and this is why easterly winds were rarely observed during the convection measurements.

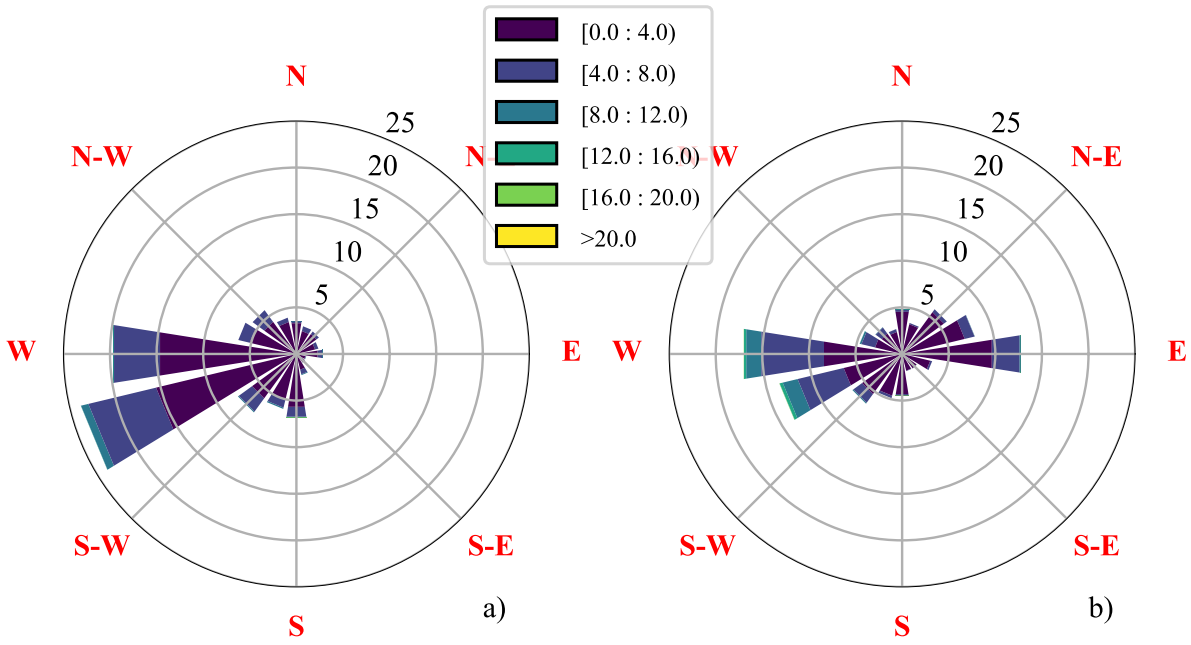

Figure 4.1: Wind rose according to 10 min wind data from the German Meteorological Service (DWD) station "München Flughafen" (Deutscher Wetterdienst, 2023c, station 1262, last access January 19, 2023). **(a)** Wind rose over the 30 d dataset applied in this work. **(b)** 30 year climatological wind rose. The percentage occurrences of a wind direction are visualized by the length of the spokes. The wind strength is visualized in color.

Another difference is the slight shift to more southerly winds. This could be related to the orography – south and southwest of Munich the terrain becomes gradually hilly, while the wind measurements have been taken at a flat countryside just north of Munich. While direct southerly winds are usually associated with dry descending air in the lee of the Alps, southwesterly winds do not necessarily come over the Alps and are still influenced by the orography. This can serve as a forced lift to trigger convection, which then moves further northeast and over Munich.

4.1.2 Stability

In Fig. 4.2, model-based CAPE, CIN, and precipitable water are shown. The model data was chosen to be independent of the closest observational soundings that are taken only twice a day from Oberschleißheim at 0 and 12:00 ,UTC. By using model based soundings, a time of the day can be chosen that is more representative of the thunderstorm potential of that day. This must be before any convection started to reduce the available CAPE. In addition, the model soundings are likely to be very close to reality anyway, because the global GFS model that is used to provide initial and boundary conditions to the WRF simulations does include observational radiosondes.

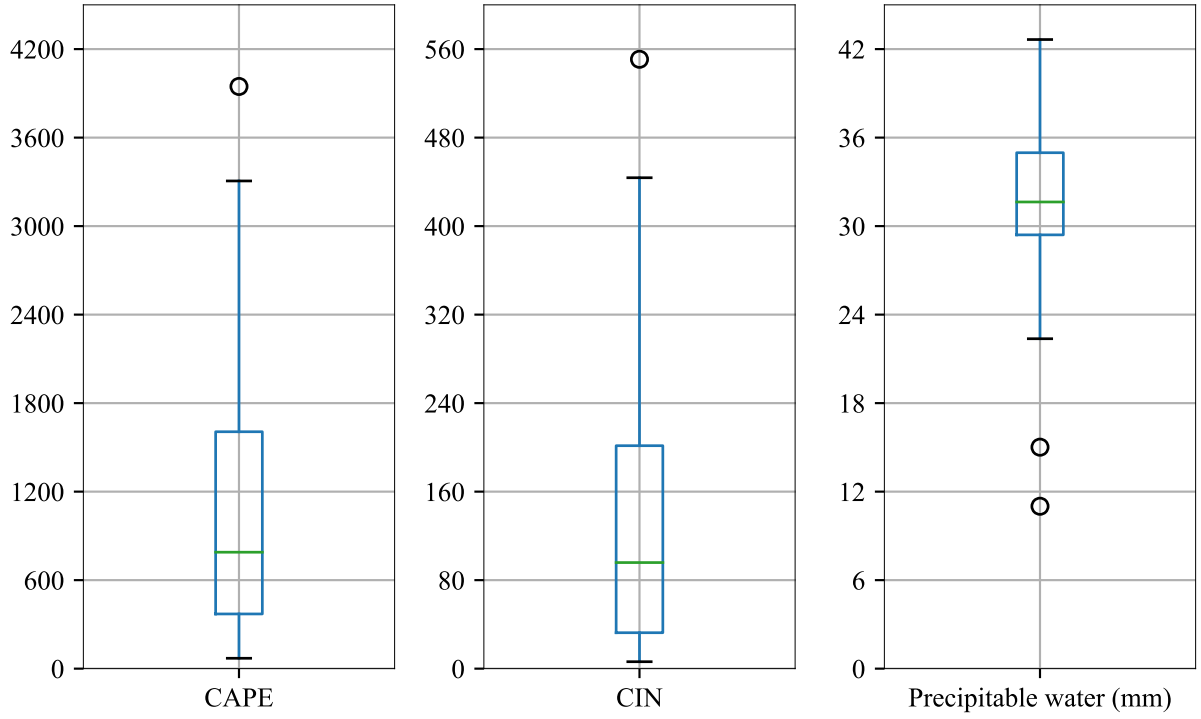

Figure 4.2: Boxplots of Convective Available Potential Energy (CAPE), Convective Inhibition (CIN) and precipitable water from model soundings at 09:00 UTC in the Munich domain over the whole 30 d dataset.

For the data in Fig. 4.2, the time at 09:00 UTC was chosen and the domain maximum was selected. This is in the late morning relative to local time, so usually before summer thunderstorms triggered by surface heating occur. The CAPE values shown in Fig. 4.2 range from 0 to in one extreme case 4000 J kg^{-1} with a median of about 800 J kg^{-1}. The DWD categorizes CAPE values up to 500 J kg^{-1} as a typical potential for weak thunderstorms, up to 1000 J kg^{-1} for moderate thunderstorms, 1000–2000 J kg^{-1} for strong thunderstorms, and anything above 3000 J kg^{-1} with the potential for extreme thunderstorms (Deutscher Wetterdienst, 2023a). Accordingly, about 70 % of the measurement days are categorized with potential for at least moderate thunderstorms, about 40 % with the potential for strong thunderstorms, and more than 5 % with the potential for extreme thunderstorms. The simulated CIN values range from 0 to about 550 J kg^{-1}. Values greater than 200 J kg^{-1} generally prevent any convection, regardless of CAPE. In some cases, this may prevent thunderstorm development if the energy required to overcome the CIN value is insufficient. However, it must be considered that CIN can also be reduced during the course of the day, for example by surface heating, and thunderstorm initiation occurred later than 09:00 UTC on most days. On most measurement days, for example, local convergence or surface heating provided the necessary energy to overcome the CIN and trigger showers and thunderstorms. The simulated precipitable water ranges from about 10 mm to about 43 mm with a median of about 32 mm. This is the water in the atmosphere that can theoretically precipitate when precipitation is triggered. Not all of this water is necessarily precipitating in every situation. However, in the case of deep thunderstorms, virtually all precipitable water can rain out and thus arrive at the ground as precipitation. Accordingly, a mean value of 30 mm over all days shows a potentially very wet collection of cases.

In summary, it can be said that the measurement days stand out as particularly humid days. Together with frequent CAPE values of 800 J kg^{-1} and higher, this explains the partially strong thunderstorms that serve as the data basis for this work. Possible thunderstorm triggers are local convergences, the orography south of Munich, or simply surface warming on hot summer days.

4.2 The NWP Model: An Example Case

Before systematic statistical examination of the model's capabilities, an example is presented showing that the model can generally provide realistic weather forecasts. Figures 4.3 and 4.4 show simulated and observed reflectivity, and the corresponding HID respectively, using one convective case in summer 2019. In convective situations, this demonstrates that all simulations are capable of producing reasonably realistic weather forecasts, but at the same time it also shows the limitations of weather simulations in these situations. The case was chosen because convective cells were present over Munich at this time step in all simulations and in the observations.

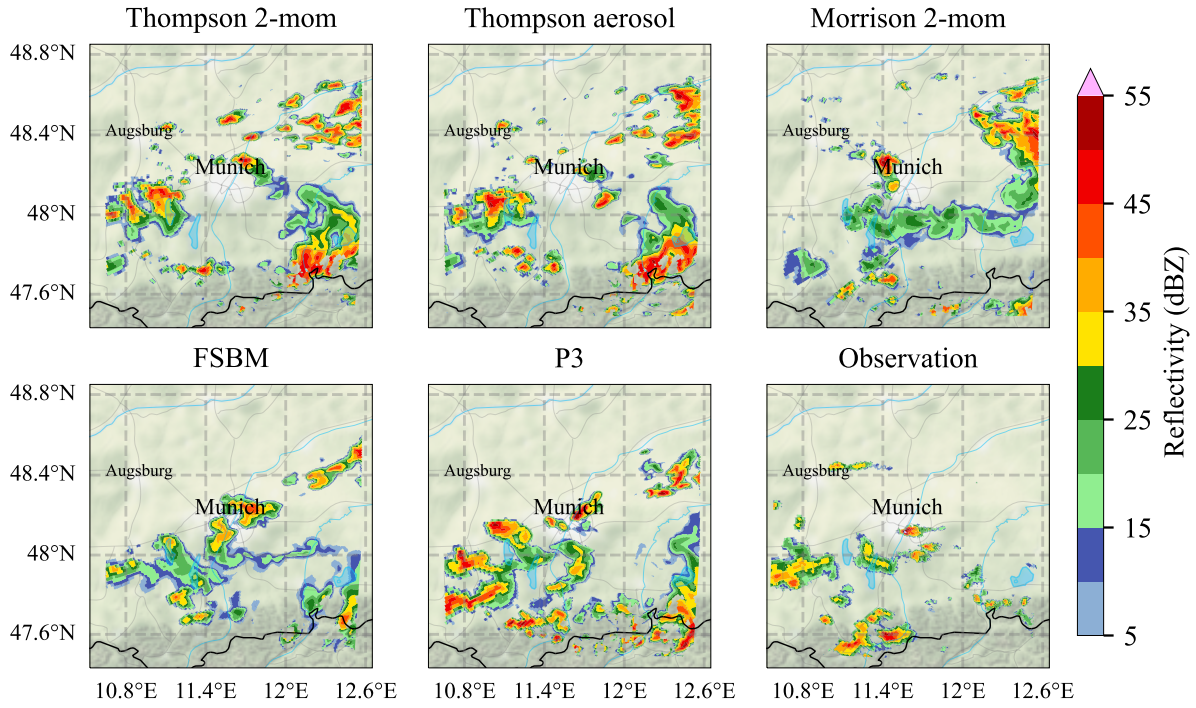

Figure 4.3: Simulated and measured reflectivity at July 7, 2019, 12:45 ,UTC over the full domain size with a grid spacing of 400 m. Simulated reflectivity from the Weather Research and Forecasting (WRF) model output after applying the Cloud-resolving model Radar SIMulator (CR-SIM). Background map tiles by Stamen Design (Stamen Design, 2023). Background map data by OpenStreetMap (OpenStreetMap, 2023, © OpenStreetMap contributors 2023. Distributed under the Open Data Commons Open Database License (ODbL) v1.0.). Roads, rivers, and lakes made with Natural Earth (Natural Earth, 2023).

The weather situation chosen as an example occurred at 12:45 ,UTC on July 7, 2019. It was characterized by widely scattered convective showers over the Alps, directly over Munich, and in the Munich vicinity (Fig. 4.3). In general, all simulations at this time produce precipitation over much of the model domain. The general convective nature of the precipitation is correctly reproduced; there are numerous scattered convective cells, some isolated, in all simulations. The

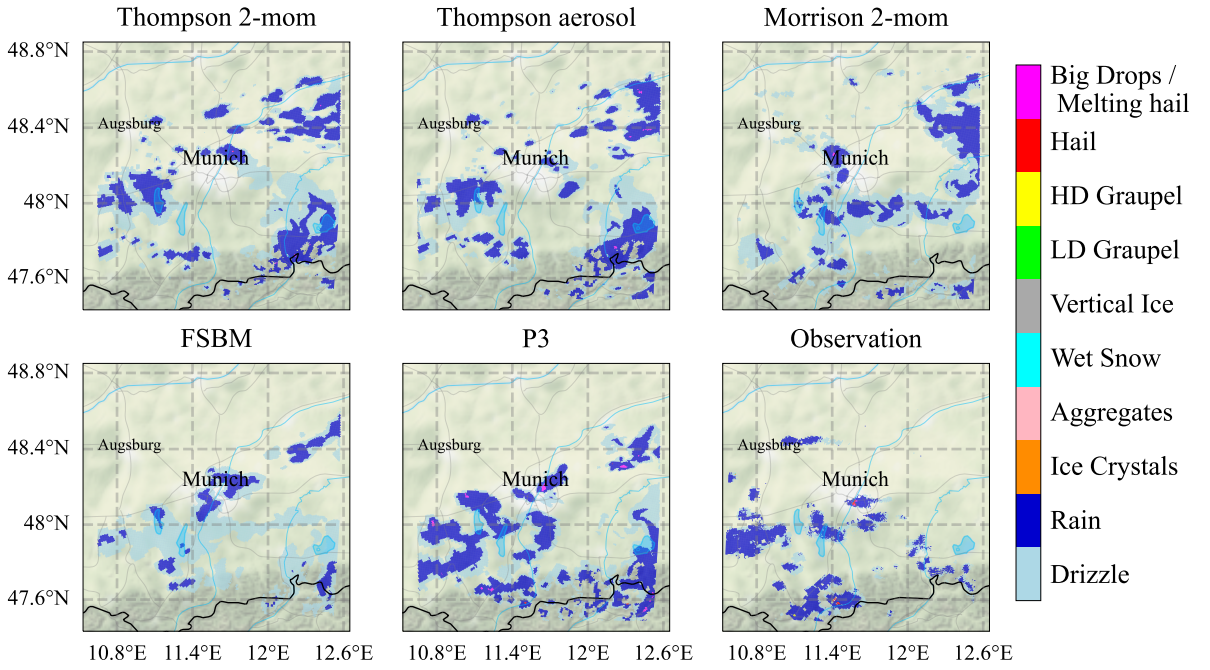

Figure 4.4: Same as Fig. 4.3, but for hydrometeor identification (HID) data, retrieved from the (simulated) polarimetric radar signals with Dolan et al. (2013). Background map tiles by Stamen Design (Stamen Design, 2023). Background map data by OpenStreetMap (OpenStreetMap, 2023, © OpenStreetMap contributors 2023. Distributed under the Open Data Commons Open Database License (ODbL) v1.0.). Roads, rivers, and lakes made with Natural Earth (Natural Earth, 2023).

magnitude of the reflectivity maxima is similar to the radar observations. However, this case also shows some limitations of NWP for convective situations: the location of the simulated convective cells does, of course, not exactly match the observations. The area covered by precipitation is larger than that observed in most simulations. This is mainly due to a simulated precipitation area northeast Munich that was not observed at that time. Further, the simulated cells are smaller and more frequent, especially in the two Thompson simulations. Here it has to be noted that this is not a general problem with these schemes. The total number of simulated convective cells from the two Thompson schemes over all 30 days is similar to those observed, as shown later. It rather emphasizes the relevance of the approach to using a larger data set in this thesis, compared to the focus on case studies to evaluate models as typically applied elsewhere.

The corresponding HID for the same case is shown in Fig. 4.4. Most of the signals are classified as rain or drizzle in both the observations and all the simulations. Embedded areas of large drops/melting hail or hail are classified in the observations and in four of the simulations: Thompson 2-mom, Thompson aerosol-aware, Morrison 2-mom, and P3 are for the most part even able to produce hail cores of very similar size to those observed at this time. At the same time, general limitations of model predictions are also evident here; the exact location of the hail and the associated convective cell is shifted compared to the observations and also varies depending on

the scheme. Not all simulations classify (melting-) hail at this time step. In addition, the hail core is partially classified as dry hail in the observations, while the simulations produce mostly melting hail at this time step. This scene shows that the choice of microphysics scheme has noticeable effects on the prediction of location, time, strength, and type of convective precipitation and that the convective weather situation can be well represented by the type of weather model setup used. But is this also relevant statistically over a longer period? For a general evaluation of the model prediction as a function of the microphysics scheme, a statistical analysis over a longer period of time is required.

4.3 Statistical Evaluation of Macrophysical Convective Cloud Properties

This section starts with macrophysical cloud characteristics, such as the cloud size, shape, or height as well as the maximum reflectivity, lifetime or the number of convective cells that were simulated. This way, tracks and evolution of individual convective cells can be analyzed over their life cycle. In turn, this helps to identify and compare specific convective cell characteristics in simulations and observations. An example of an identified convective cell and its reflectivity is shown in Fig. 4.5. This example is from a simulation with WRF and the FSBM scheme, after applying the CR-SIM radar forward operator. However, the tracking can be applied to observed convective cells in the same way. The corresponding (Euler) view of the reflectivity field over the whole domain is shown in Fig. B.1. The resulting dataset of convective cell objects allows statistical comparison of macrophysical properties and evaluation of these with the radar observations. These can be geometric properties, such as the height or volume of convective cells, but also other properties, such as maximum reflectivity or lifetime.

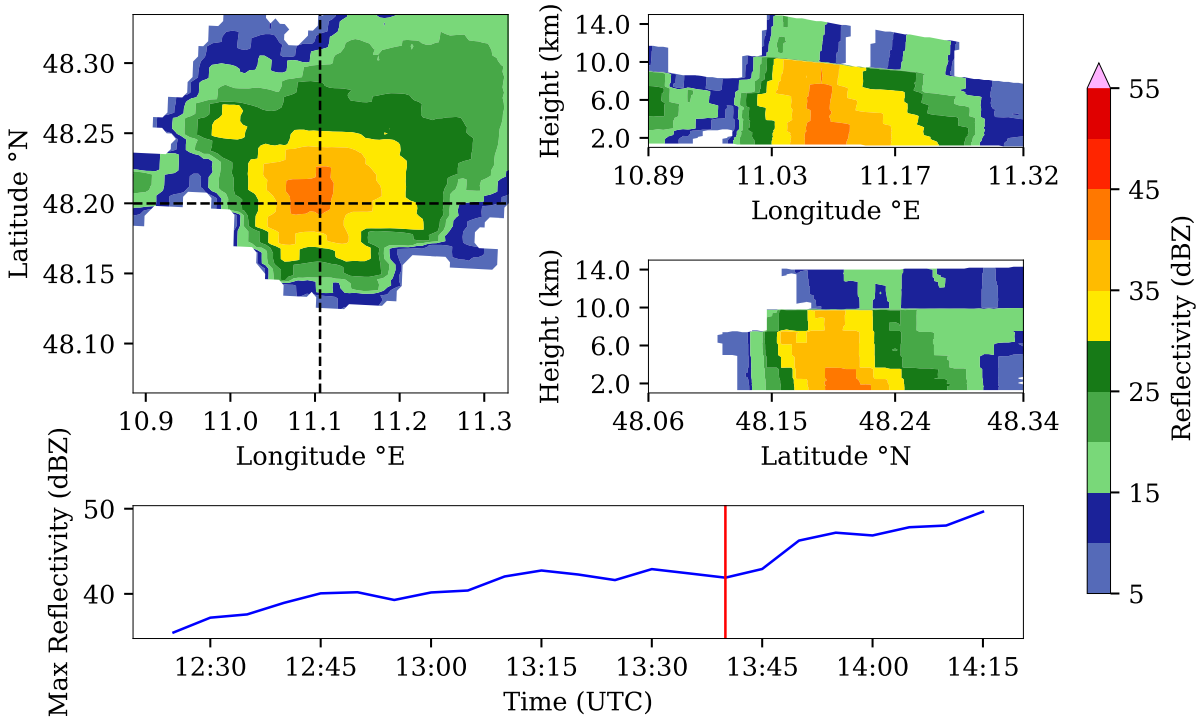

Figure 4.5: Example of a simulated convective cell, identified by the cell tracking algorithm on July 1, 2019. Top left: top–down view of the cell. Top right: latitude (top) and longitude (bottom) cross section through the center of the cell. Bottom: time series of maximum reflectivity of the convective cell over its lifetime. Red stripe: current time step corresponding to the top view and the cross sections.

In the remainder of this section, the influence of the microphysics schemes on these macrophysical cloud properties is analyzed. In Sect. 4.3.1, the simulated convective cell strengths and heights are statistically compared to radar observations. Section 4.3.2 evaluates the variability of the simulated cloud macrophysical properties in comparison to the radar observed convective cells. The influence of the cloud microphysics schemes on the 3D structure is then evaluated in Sect. 4.3.3.

4.3.1 Histograms of Convective Cell Strength and Altitude

We begin the comparison with an evaluation of the geometric properties of simulated and observed clouds. Figure 4.6 shows histograms of the convective cell core extent (altitude of continuous 32 dBZ volumes) as well as the maximum cell reflectivity provided by strategy A. Strategy A refers to the observational dataset by the DWD C-band radar in Isen, as described in chapter 3.

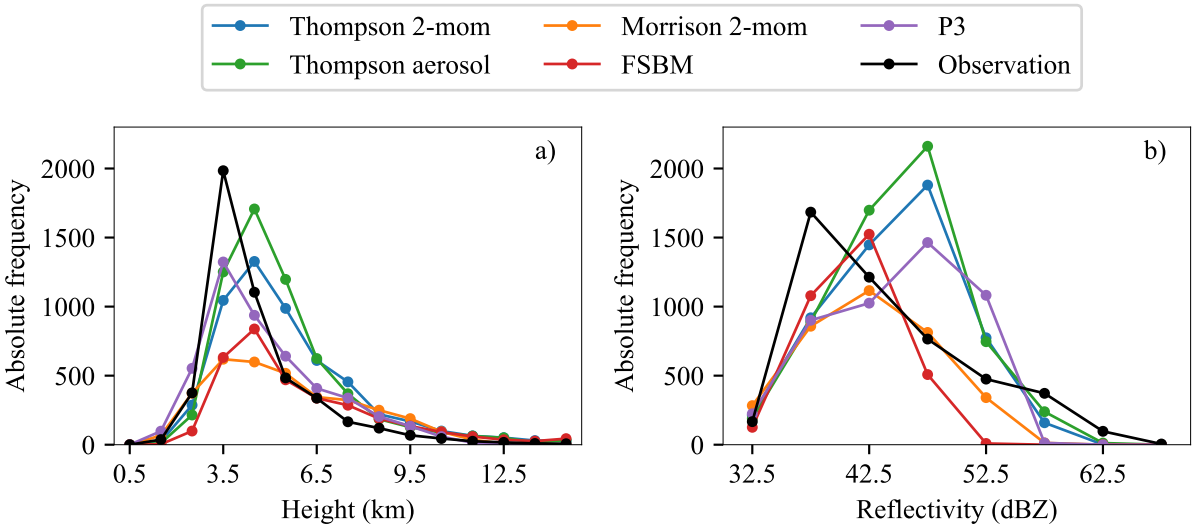

Figure 4.6: Cell core height **(a)** and cell maximum reflectivity **(b)** distribution for inner simulation domain over 30 convection days for observations and 5 microphysics scheme simulations.

At each 5 min time step during 30 convective weather days, all cell detections are summed up on DWD ISEN observation data or CR-SIM forward simulations. The cell tracking algorithm matches convective cells of consecutive time steps by applying similarity measures such as the convective cell area, as described in Sect. 3.6. Sometimes, the algorithm fails to correctly match the same convective cell in two consecutive time steps, even though the cell was identified in both time steps. By counting convective cells at each time step independently, the analysis is independent of any possible matching error; e.g., a single cell detected for 30 min would contribute to the statistics six times.

The cell core top heights of observed cells (Fig. 4.6 a) show a distinct peak with more than 2000 cell detections at an altitude of 3–4 km. This corresponds to about 40 % of all cell detections by the radar. All NWP simulations independent of the microphysics scheme are able to reproduce

a peak at a similar altitude, but none of them as pronounced as in the observations. The two Thompson schemes show a tendency towards slightly higher cell core heights of 4–5 km. Reflectivities of more than 32 dBZ above the melting layer are mostly related to big graupel particles in the simulations and, to a lesser extent, rain likely lifted by updrafts. In particular, both Thompson schemes more frequently simulate graupel particles that produce very high reflectivities of more than 45 dBZ above the melting layer (see Appendix C).

A similar approach to comparing cloud geometry in simulation and radar observation was followed in Caine et al. (2013). They objectively compare simulated cell characteristics with observations over 4.5 days after applying a cell tracking algorithm on their data. Among other things, they found the simulated convective cells to reach higher altitudes on average compared to their radar observations, which is also visible in this analysis. This is independent of the chosen cloud microphysics scheme and mainly a result of the missing small-scale cells in the simulations, which is indicative of a resolution effect: the very small cell heights correspond to small cells that might not be resolved, even at 400 m grid spacing.

Regarding the total number of cell detections, the Thompson schemes are closest to the observed number. A total of 5458 cell detections are counted, i.e., the number of cells in all 5 min observation time steps. The Thompson aerosol-aware scheme (6035) is still close to the observed number; the basic Thompson 2-mom scheme (5468) is the closest; and the P3 (4758) has fewer cells. Especially the Morrison 2-mom (3427) and FSBM schemes (3326) produce too few convective cells. This difference is mainly a result of missing small-scale development (early stages, weak cells) in the simulations. For fully developed thunderstorms (cell core top heights > 7 km), all schemes produce numbers that are slightly larger than in the observations (observations: 554, Thompson 2-mom: 1139, Thompson aerosol-aware: 948, Morrison 2-mom: 928, FSBM: 899, P3: 780).

The related distribution of maximum reflectivity of each cell provides some clarification (Fig. 4.6 b). The observed high occurrence of weaker cells is only partially visible in FSBM and Morrison 2-mom schemes. While the total number of weaker cells (max cell reflectivity at 35–40 dBZ) is still too low, the Morrison 2-mom and FSBM schemes show the highest relative occurrences for relatively weak cells between 40–45 dBZ maximum reflectivity. This still does not represent the pronounced peak of observed cells at weaker reflectivities of 35–40 dBZ well. The other three schemes produce too many medium-intensity cells and too few low-intensity cells. At the other end of the reflectivity spectrum, none of the schemes are able to reproduce the occurrence of the strongest reflectivities above 57 dBZ. In part, this is most likely related to numerical smoothing of local and rare values in the NWP model. However, this could also be related to simulated particle densities. The particle density strongly influences the radar reflectivity. Thus, the missing high reflectivities could also be a result of missing high density particles (e.g., hail) in the simulations.

4.3.2 Variation of Convective Cell Characteristics

The TINT cell tracking provides the area, volume, maximum reflectivity, maximum height, and lifetime of the convective cell objects identified in the data. Figure 4.7 shows all of these

variables as simulated by the various microphysics schemes and observed by radar. In this type of visualization, the model-simulated cell properties are on the x-axis, while the radar observations are on the y-axis. Visualized is the entire 30 d data set. Each day is shown with a dot representing the median value of that day. The color saturation (alpha value) shows the number of cells identified on that day, so that days with many convective cells appear stronger than days with few cells. The bars range from the 25th to the 75th percentile of all cases of each day. The colors show the different microphysics schemes.

Figure 4.7 shows the horizontal area covered by a convective cell 1.5 km height in the upper left. Most convective cells have an average cell area of less than 40 km^2 in both observation and simulation. The medians show positions slightly above the 1–1 line, indicating a small bias towards areas simulated too small. However, the 75th percentiles are much higher for the radar-observed convective cells than for the simulated cells. This means that although the convective cells are simulated with approximately the correct size on average, the simulations often lack the particularly large-scale convective cells of more than 40 km^2. The maximum height of the convective cells is shown in the middle left. This is the maximum height of the 32 dBZ reflectivity line within an identified convective cell. A strong bias in the simulated cell heights is visible here. Almost all the simulated convective cells extend up higher than the observations. However, the convective cell volume (middle right) is fairly well simulated on average. The medians scatter around the 1–1 line, without a clearly visible bias. This is due to the fact that cell volume depends on cell area and cell height, with two biases in the model canceling each other out here. Typically, the volume is very well simulated, but again the 75 % percentile more often reaches larger values in the observations, compared to the simulations. Probably this is related to the simulated area, which has the same bias. The maximum cell reflectivities (top right) show that the simulations were on average able to reproduce the observed cell reflectivities, although the scatter around the 1–1 line is considerable. However, a clear color gradient is evident: red and orange are primarily to the left – green, blue, and violet to the right of the 1–1 line. This means that the microphysics schemes have a significant influence here, unlike most other macrophysical quantities. The FSBM (red) and Morrison 2-mom (orange) schemes produce reflectivities that are too small compared to the observations, while P3 (purple), Thompson 2-mom (blue), and Thompson areosol-aware (green) produce reflectivities that are too high. It is also noteworthy that almost no simulations yielded reflectivities greater than 50 dBZ, although such reflectivities have certainly been observed. Regarding the number of convective cells (bottom right), a similar picture can be seen. On average, the number of cells identified is close to that of the 1–1 line, but again a color gradient can be seen. Again, FSBM and Morrison 2-mom produce too few cells, while the other three schemes produce too many cells. In the bottom left of Fig. 4.7 shows the lifetime of the convective cells. Here it can be seen that the vast majority of convective cells lived less than 30 min, both in the observations and in the simulations. However, this is more indicative of problems with the algorithm used to match the cells: while the cell tracking algorithm used successfully identified the most convective cells, matching the same convective cell across multiple time steps often failed. Instances where a convective cell was tracked over a long lifetime were rare, making statistical analysis of convective cell lifetimes difficult and ultimately leading to the decision to drop the method this from this work entirely.

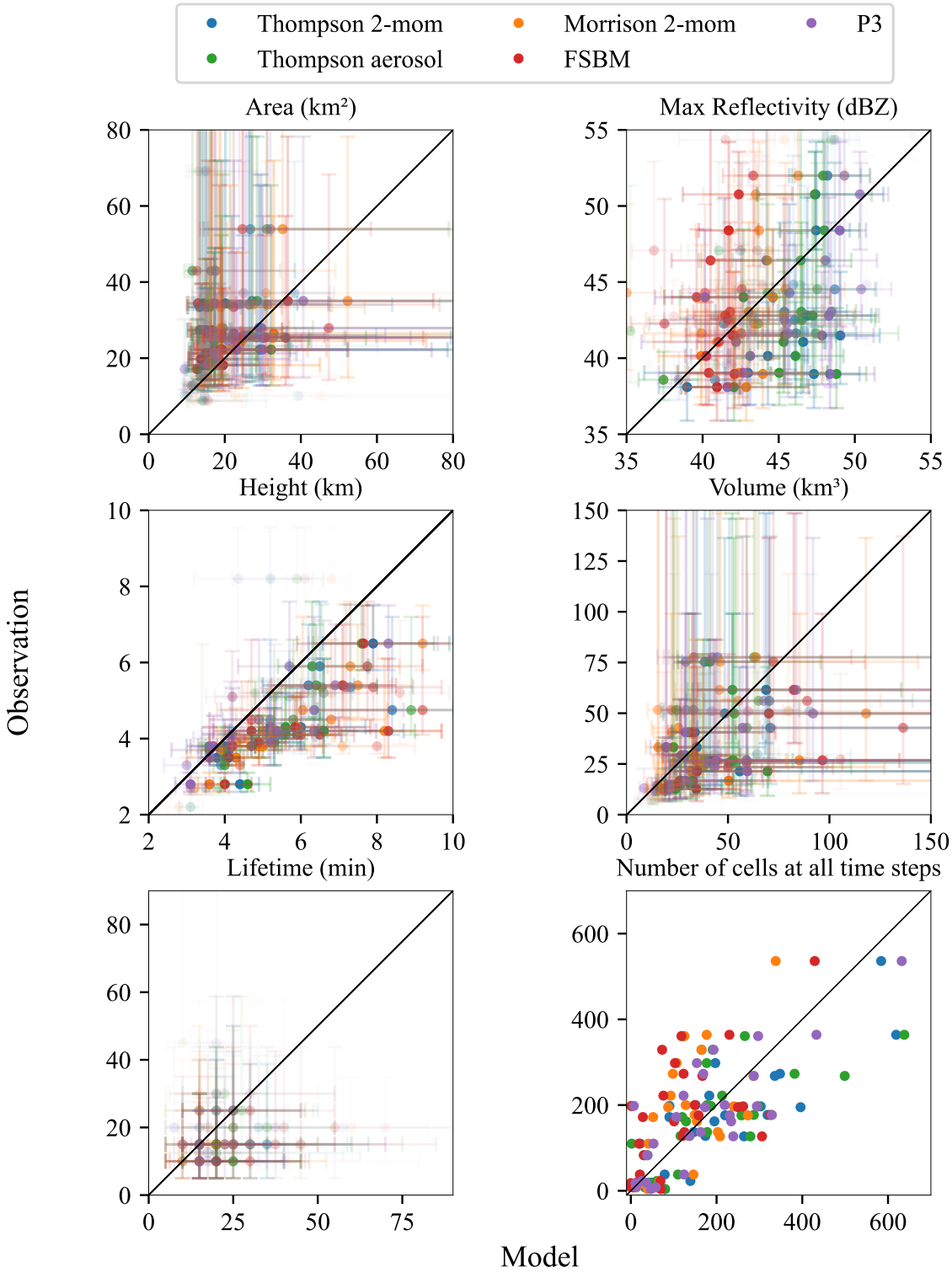

Figure 4.7: Statistics of macrophysical cell properties over the 30 d data set. The points are the daily medians, and the bars show the 25- and 75- percentiles. The alpha values of the points are scaled by the number of simulated/observed convective cells (except for the total number of convective cells, bottom right).

In summary, the simulated cell tops reach higher than observed. The horizontal area and volume are correctly simulated on average, but observed convective cells with large horizontal extent are often missed by the simulations. The maximum reflectivity of the cells strongly depends on the applied microphysics scheme, with the FSBM and Morrison 2-mom schemes underestimating the reflectivity, and the Thompson 2-mom, Thompson aerosol-aware, and P3 schemes overestimating the maximum reflectivity of the cells. High reflectivities greater than 50 dBZ are generally not simulated, even if they have been observed. The number of identified cells is similar between observations and simulations, with differences depending on the microphysics scheme: FSBM and Morrison 2-mom generally simulate fewer convective cells than the other three schemes. In general, most tracked convective clouds had lifetimes of less than 30 min. This is partly due to an imperfect tracking algorithm. In general, the variation of most macrophysical cloud features is similar in observation and simulation. The exceptions are cloud area and volume, where observed convective clouds show higher variation toward larger cloud area and larger volume.

4.3.3 3D Convective Cloud Geometry

In the previous section, several convective cell characteristics were statistically evaluated. However, all the previous analyses were based on the TINT cell tracking algorithm, which uses a 32 dBZ reflectivity threshold to identify convective cells. This is a somewhat arbitrary threshold. There are certainly cases where one would define a convective cell at lower or higher reflectivity thresholds. In addition, TINT tracking does not provide any further information about the structure within the convective cell. How large is the convective core? How fast does the reflectivity drop off to the edge? In the following section, an alternative approach is taken to visualize the 3D structure of simulated and observed reflectivity fields, similar to the approach taken in Stein et al. (2015). By simply drawing reflectivity isolines and calculating the circled area, one can get an idea of the 3D structure of the simulated and observed reflectivity fields. In Fig. 4.3 an example of the reflectivity isolines has been shown. Figure 4.8 shows the mean area enclosed by isolines of different reflectivity as a function of height over all time steps and 30 days.

In general, the 3D structure seems to fit quite well. Especially at the surface, the mean isoline radius is reproduced almost perfectly by most schemes for all reflectivity values. At most other heights, the simulated mean isoline radius is also close to the observations. However, there are discrepancies in some microphysical processes with respect to the convective cores. For example, the FSBM scheme does not produce situations with reflectivities above 50 dBZ. This was noted in the previous section and is due to microphysical reasons related to the simulated rain PSD. This will be discussed in more detail in Sect. 4.4 and Sect. 4.5. However, the extent to which the stronger convective reflectivity isolines extend upward also varies between the schemes. For example, the Thompson 2-mom and Thompson aerosol-aware schemes simulate 40 dBZ isolines extending up to 14 km and beyond, and the 50 dBZ isoline up to 10 km. This is unrealistically high and is not confirmed by observations. To generate such reflectivities, one would need very large or very dense particles (or both), such as large graupel or even hail. These particles are produced by falling processes, such as collisions of smaller ice crystals with supercooled liquid, and are therefore not expected at altitudes of 10 km or more.

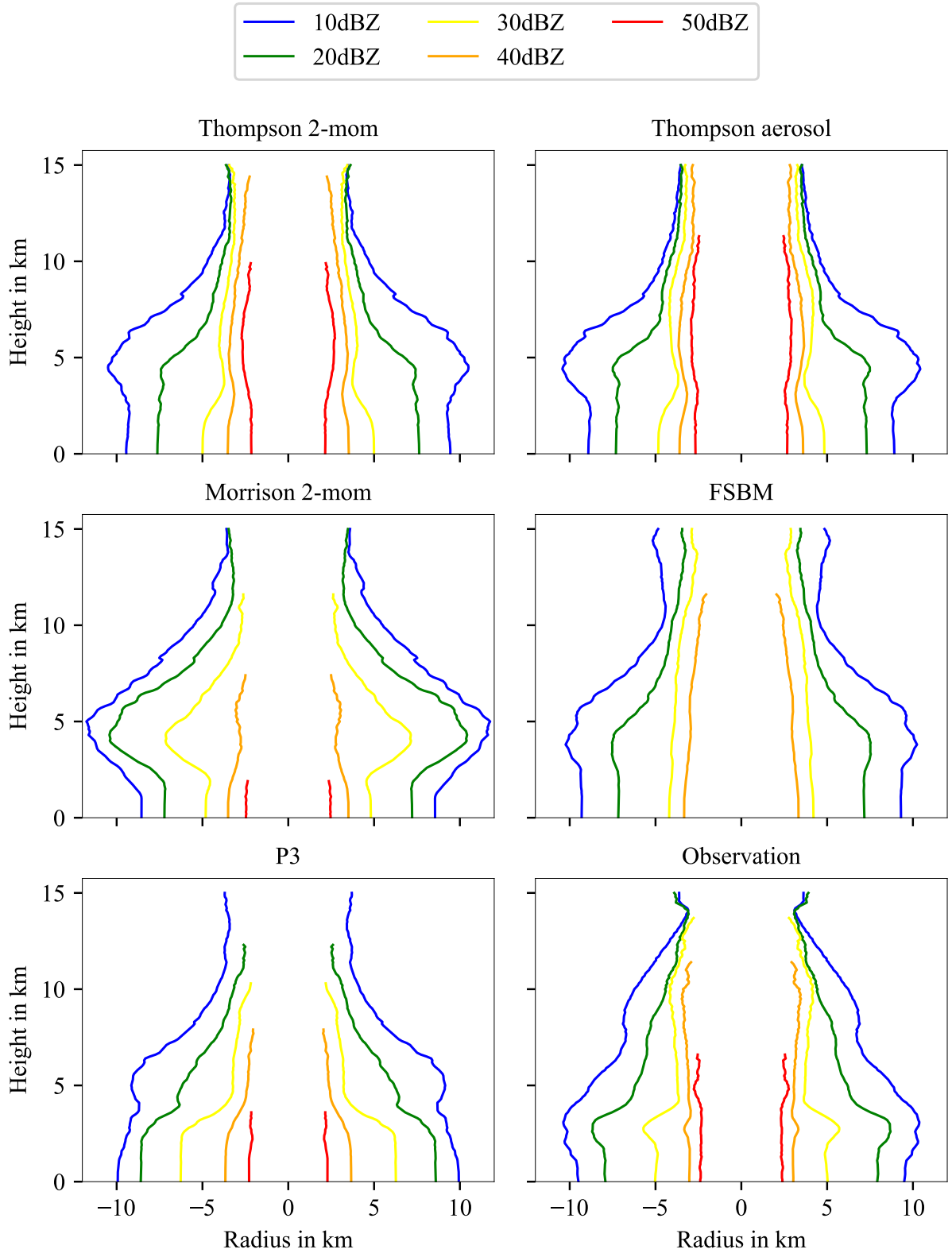

Figure 4.8: Mean reflectivity isoline radius for varying reflectivity thresholds.

In contrast to the two Thompson schemes, the Morrison 2-mom and P3 schemes produce isolines that extend to altitudes similar to those observed, but the Morrison 2-mom scheme in particular does not extend quite high enough. This is probably related to the fact that the Morrison 2-mom scheme generally produces reflectivities that are too low, as seen in the previous section. On average, the P3 scheme fits best. A notable feature is the increase in the isoline radius at intermediate altitudes from 3–6 km altitude. This is present in the observations and all simulations to varying degrees and at different altitudes. While this increase in isoline radius was observed at about 3 km altitude, the simulations show this feature more at 5 km altitude. It is most pronounced in the Morrison 2-mom scheme, while in the P3 scheme this isoline radius increase is only barely visible. At first thought this could be related to the "bright band" (Austin and Bemis, 1950), where melting particles lead to a strong increase in reflectivity, since the size is still dominated by large ice aggregates, but the dielectric constant is much higher due to the liquid coating, causing a strong increase in reflectivity. However, to simulate a bright band, the model must be able to simulate melting particles that are part ice and part water. Alternatively, the radar forward operator must apply a "melting scheme" in which this effect is parameterized by thermodynamic variables. In this work, neither of these applies; the schemes do not include partially melted particles – they are either completely melted or completely frozen. The radar forward operator used here also does not apply a melting scheme. This means that the increase in the isoline radius must have a different origin. Instead, this is probably related to melting and evaporation processes, where liquid droplets evaporate below the melt layer height, which would then lead to a decrease in reflectivity and isoline radius. At the moment, however, this is still an unproven theory.

To explain deviations in macrophysical properties, the underlying microphysical characteristics are important, such as the role of the PSD, which strongly influences the reflectivity signal. Therefore, in the following two chapters the focus is on microphysical aspects of the simulated and observed processes.

4.4 Vertical Structure of Polarimetric Radar Signals

In the previous section, macrophysical cloud properties have been evaluated. Some deviations between observations and simulations have been found, that depend on microphysical aspects, such as the PSD or the particle density. These aspects strongly influence the polarimetric radar variables. Thus, in the following section the vertical distribution of simulated polarimetric radar variables is compared to the observations, to narrow down differences in the underlying cloud microphysics.

4.4.1 Profiles of Reflectivity

Contoured frequency by altitude diagrams (CFADs; Yuter and Houze, 1995) for reflectivity Z_e of observed and simulated convective cells are shown in Fig. 4.9 provided by scan strategy B. This scan strategy provides dual-wavelength profiles of high vertical resolution through convective clouds.

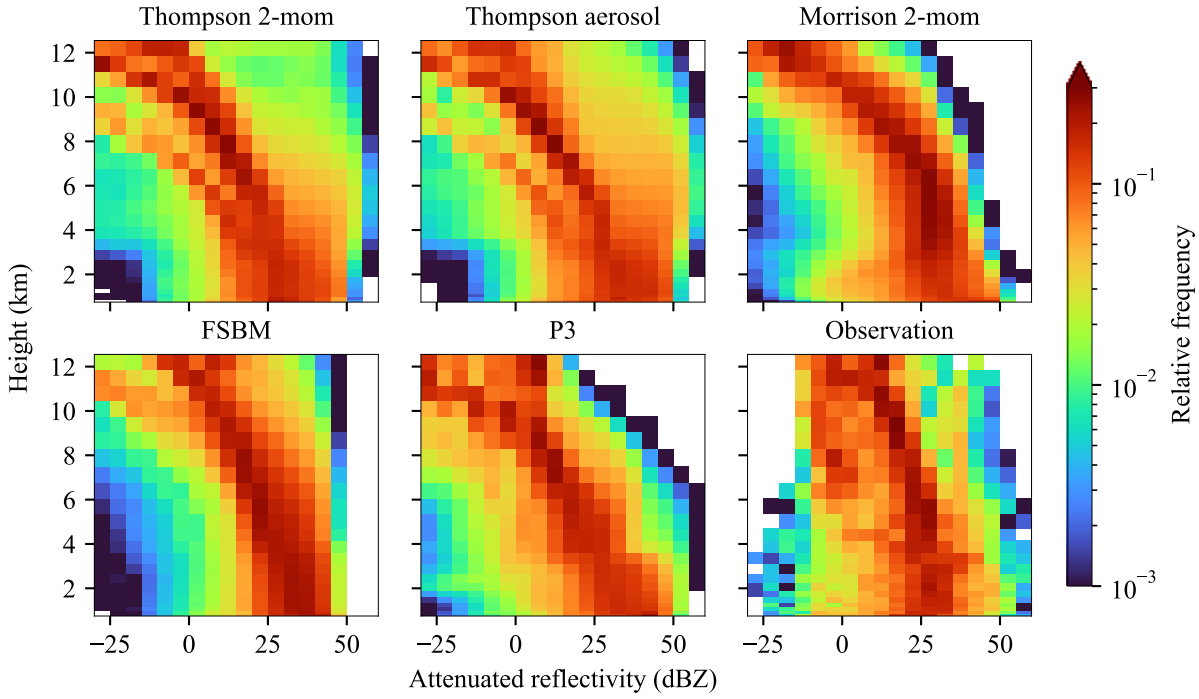

Figure 4.9: Contoured frequency by altitude diagrams (CFADs) of simulated and measured reflectivity Z_e over 5 convective days in 2019. Radar observations with POLDIRAD.

The observation CFADs contain about 1300 profiles in convective clouds. The simulated CFADs consist of many more profiles (on the order of 10^5) because 1) all cells present during one time step on the model domain are analyzed, and 2) all columns within each identified cell are included (as opposed to the 3 x 3 profiles that an S-RHI observation provides). The restriction to the center

profile of the convective cell, which is a default output of the TINT cell tracking, would have been an alternative approach. This approach was not taken because of three reasons: 1) the observation was targeted at the location of highest reflectivity and the geometric TINT cell center is not necessarily the location of highest reflectivity; 2) using the S-RHI strategy, more variation from each cell is included compared to one center profile; and 3) more profiles provide a better statistical basis for intercomparison of schemes. In Fig. 4.9 the simulated reflectivities are corrected for attenuation to make them comparable to the radar observations. Below the melting layer, high reflectivities of more than 30 and up to 45 dBZ are simulated most frequently. Overall, the schemes agree in the simulated reflectivity in this area, mostly caused by rain and graupel. They differ only in the spread. The Morrison 2-mom scheme shows a higher spread, more often simulating reflectivities below 30 dBZ and even down to 0 dBZ. In contrast, the FSBM produces reflectivities below 25 dBZ less often than the others within the convective cells. Compared to the observed CFAD, high reflectivities below the melting layer are generally modeled too frequently. This is in agreement with Putnam et al. (2016), who compare radar signals simulated by five different microphysics schemes for two case studies and find that especially the Morrison 2-mom scheme, but to a lesser extent also the Thompson 2-mom scheme, produces Z_e values that are too high. They attribute this to stratiform rain PSDs that contain too many large drops, to an over-forecast of the precipitation coverage overall, and, in the case of Morrison 2-mom, to a high bias of wet graupel in convective regions. Given that the forward operator applied in this study does not consider wet particles, it is found that the high bias in Z_e exists even without considering wet graupel and comes mostly from rain, suggesting PSDs that contain too many large raindrops compared to the observations.

Above the melting layer, simulated reflectivities start to decrease with height. This is a fingerprint of ice growth processes where falling particles increase in size by deposition, aggregation, or riming. At these subfreezing heights, the schemes show more deviations from each other. While most schemes exhibit a smooth transition from ice to liquid phase, the prominent exception is the P3 scheme for which reflectivities abruptly increase by about 15 dBZ at the melting layer height (approximately at 3.6 km height, varies among cases). All other schemes show a slow and smooth increase in reflectivity, which better agrees with the observations. However, given that the reflectivity within rain was too high, the reflectivity distribution above the melting layer height is reproduced quite well by the P3 scheme. Most other schemes directly above the melting layer height extend to higher reflectivities, showing reflectivities greater than 25 dBZ too often. The two Thompson schemes even simulate reflectivities of more than 45 dBZ above the melting layer height, frequently. These extreme reflectivity values are produced mostly by graupel and to a lesser extent by rain (see Appendix C for CFADs of radar signals separated by hydrometeor classes). Compared to the measurements, these reflectivities are unrealistically large. A high bias in reflectivity could be produced in principle by three mechanisms: the simulated particles are 1) too dense, 2) too many, or 3) too large. The graupel densities assumed by the schemes (and correspondingly in the forward operator) are 500 kg m^{-3} in both Thompson schemes, and 400 kg m^{-3} in the Morrison 2-mom and FSBM scheme. The higher graupel density could explain the higher bias seen in the Thompson schemes compared to the moderate bias in Morrison 2-mom and FSBM, but the underlying PSD could also play a role. Reflectivity overestimation in deep convection at

subfreezing temperatures was found by other studies as well (e.g., Stanford et al., 2017, Varble et al., 2011) and is explained to be a result of graupel or snow particles that are too large, likely a product of overly strong updrafts. Stanford et al. (2017) show that this bias not only exists for bulk schemes, but also for a bin scheme. This is confirmed by the simulations of this work; the bias exists for the FSBM scheme too, even though it appears to be strongest in the two Thompson schemes. However, this could be a consequence of the higher assumed graupel density.

4.4.2 Profiles of Polarimetric Variables

The same analysis is possible for simulated and observed polarimetric variables, e.g., differential reflectivity Z_{DR} (Fig. 4.10). K_{DP} was found to provide not much additional value, in part due to noisy observations, which is why K_{DP} is neglected in the subsequent analysis.

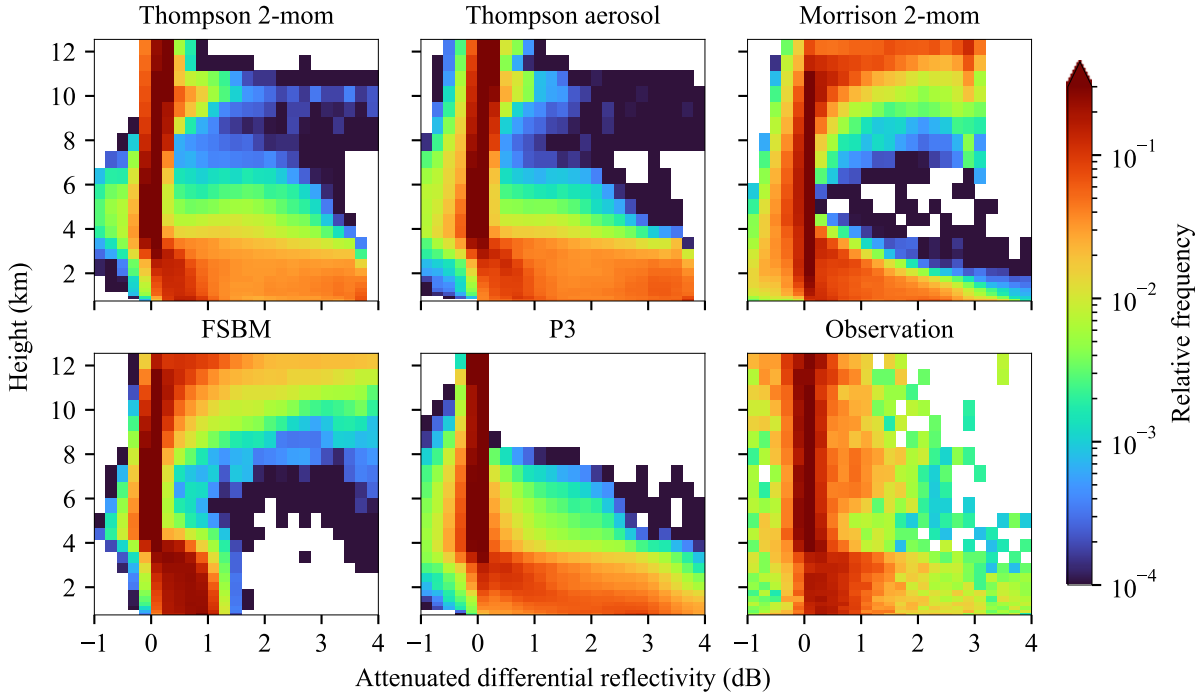

Figure 4.10: Contoured frequency by altitude diagrams (CFADs) of simulated and measured differential reflectivity Z_{DR} over 5 convective days in 2019. Observation with the POLDIRAD radar.

Strong differences between the simulations are visible in the liquid phase below the melting layer. While most schemes show a wide spread over the whole range of 0–4 dB within rain, the FSBM only produces Z_{DR} values up to around 1.5 dB. This is in much better agreement with the observations, where Z_{DR} values of up to 1.5 dB have been measured most of the time, though also covering slightly higher Z_{DR}. Here, the advantage of the FSBM that uses a discrete PSD becomes apparent. The FSBM scheme is able to explicitly predict raindrops of each bin, which is

more flexible and potentially better captures the variability in observed PSDs (better size-sorting). Ryzhkov et al. (2011), for example, evaluate radar signals simulated from a spectral bin scheme for a hailstorm case and find that their spectral bin scheme produces PSDs for rain that deviate from the gamma distribution. Bulk schemes would not be able to reproduce these PSDs, and since radar signals strongly depend on the PSD, Ryzhkov et al. (2011) argue that spectral bin schemes are better suited to simulate polarimetric radar signals. However, contributions by other microphysical processes, such as drop breakup or evaporation, could also facilitate the Z_{DR} signatures and were not examined in this study. All other schemes use a gamma distribution (Eq. 3.1) with a shape parameter $\mu = 0$ for rain. This effectively is an exponential (Marshall–Palmer) PSD, which has a slope that is too weak; there are too few small rain droplets and too many big drops. Putnam et al. (2016) find similar results regarding Z_{DR} signatures near the surface. In their two case studies, the simulations with Thompson 2-mom and with Morrison 2-mom cloud microphysics showed incorrect Z_{DR} maxima, associated with isolated large drops at locations of weak convection, where this would not be expected. All of this suggests that the underlying rainPSD are better captured by the FSBM compared to the bulk schemes.

In order to separate the analysis into reasons due to differences in the underlying modeled microphysics and due to different processing in the forward operator, rain PSDs directly produced by the NWP model were examined (rain PSD CFAD in Appendix C). The FSBM scheme provides the rain PSDs over a number of size bins; for the bulk schemes, the PSDs are calculated according to the schemes' parameterization. The FSBM bins are approximated by calculating the number of drops for the geometric center of the FSBM bin. The calculated number of drops for the given bin center diameters is then summed over all time steps and over the grid boxes at each height and visualized as a relative frequency. Only grid boxes that were flagged as a convective cell by the TINT cell tracking are considered. The rain PSD CFAD confirms the findings of the Z_{DR} CFAD: the two Thompson schemes simulate large raindrops from the surface up to the melting layer height and even above, while the Morrison 2-mom scheme produces large raindrops only at the surface, and the FSBM produces the highest frequency of small droplets.

Directly above the melting layer, the FSBM and Morrison 2-mom schemes show Z_{DR} values close to 0 dB, while the P3 and the two Thompson schemes have their frequency maximum at 0 dB but also show more spread to higher Z_{DR} values. Z_{DR} of 0 dB is associated with spherical particles. The signal directly above the melting layer height is generally dominated by graupel, which has the highest reflectivity signal (see Appendix C for separation by hydrometeor class) and is associated with Z_{DR} values of 0 dB, due to the assumed aspect ratio of 1 in the forward simulation. The sparse but large values of Z_{DR} in the two Thompson schemes and the P3 scheme are predominantly caused by rain, likely lifted by strong updrafts in the convective situations. The FSBM scheme also shows Z_{DR} signals originating from rain particles in that area, but the total Z_{DR} is reduced by a significant contribution from other hydrometeors with a lower Z_{DR}. Only the Morrison 2-mom scheme shows no contribution by lifted raindrops directly above the melting layer. The observations show a little more spread compared to Morrison 2-mom and FSBM in that area, but the Z_{DR} does not reach values as high as for the two Thompson and the P3 schemes. There are multiple possible explanations for the differences to the observations: compared to the observed convective cells, 1) more (fewer) large raindrops are lifted above the

melting layer height in Thompson 2-mom, Thompson aeresol-aware, and P3 (Morrison 2-mom and FSBM); 2) there are more (fewer) particles with spherical nature alongside lifted raindrops in the observations that reduce the total Z_{DR} compared to Thompson 2-mom, Thompson aeresol-aware, and P3 (Morrison 2-mom and FSBM). Furthermore, 3) the observed variability of Z_{DR} is possibly not correctly captured by the radar forward operator, which has to assume fixed distributions of particle orientations as well as a fixed aspect ratio of the particles.

At upper levels, clear differences between Morrison 2-mom and FSBM, and the two Thompson and P3 schemes can be seen. The Morrison 2-mom and FSBM schemes show Z_{DR} values of up to 4 dB at these heights, while the Thompson schemes and the P3 scheme are close to 0 dB. Here, the high Z_{DR} values are caused by cloud ice (see Appendix C for CFADs of radar signals separated by hydrometeor class). All schemes assuming spherical cloud ice or with other dominating spherical hydrometeor classes at these heights show small Z_{DR}. This is true for the P3 small ice fraction for which the forward operator assumes spherical aspect ratio of 1. In the Thompson schemes, the assumed aspect ratio by the forward operator is 0.2, suggesting that other hydrometeor classes with lower Z_{DR} like snow or graupel dominate the signal. Only for FSBM and Morrison 2-mom (aspect ratio 0.2) does cloud ice dominate the signal. The stronger signal in FSBM and Morrison 2-mom is not a result of different density assumptions because both the FSBM and Morrison 2-mom scheme assume lower density of cloud ice compared to both Thompson schemes. The observations do not show increased Z_{DR} at these heights. This could either mean 1) that there are no large cloud ice particles observed, 2) that the signal is dominated by other more spherical particles in the observations, or 3) that the assumed aspect ratio of 0.2 by the radar forward operator is unrealistic, and the observed particles are more spherical in nature.

4.4.3 Profiles of Dual-Wavelength Variables

More insight about the particle size is provided by the simulated and observed dual-wavelength ratio dwr Fig. 4.11). The standard radar reflectivity is strongly influenced by the number of particles within the radar beam, the particle sizes, and the particle densities. In contrast, dwr is rather sensitive to the particle size. In principle, it is also sensitive to the particle density, but the simulated density is assumed to be constant or a function of particle size.

Figure 4.11 shows deviations between the schemes within the ice phase as well as in the liquid phase. Here, no attenuation correction is applied. This makes the comparison to the radar observations less realistic but reveals differences in microphysical processes and fingerprints between the simulations more clearly. The observations show dwr close to 0 dB at upper levels, where ice crystals are very small. All simulations and the observations agree at these heights. The observations then show a steady increase of dwr towards the melting layer height. This reflects ice particle growth, given that dwr is mainly sensitive to particle size. All simulations reproduce this increase of dwr towards the melting layer heights but differ in the slope and height where the increase starts. While the Morrison 2-mom and FSBM simulations already show the beginning of an increase in dwr at about 10 km, the P3 and the two Thompson simulations show the beginning of an increase at about 7 km, which agrees better with the observations. At melting layer heights, the dwr values reach their maximum in all simulations. The magnitude of the

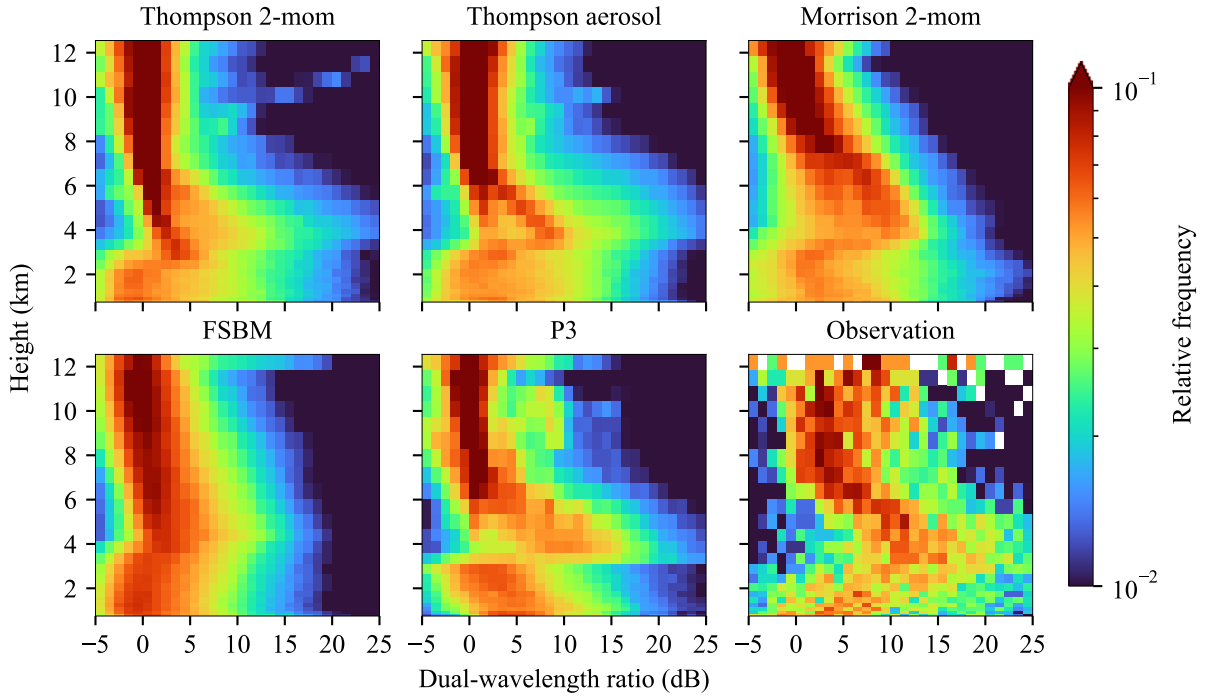

Figure 4.11: Contoured frequency by altitude diagrams (CFADs) of simulated and measured *dwr* over 5 convective days in 2019. Radar observations with POLDIRAD and MIRA-35.

maximum *dwr* values differs: Morrison 2-mom and FSBM do not produce *dwr* values larger than 20 dB, while the P3 and the two Thompson schemes produce *dwr* values of up to 25 dB. At these heights, the two Thompson schemes produce distinct streaks of higher frequencies at low *dwr* values (0–10 dB) and then a diffuse area of lower frequencies at higher *dwr* (> 10 dB). The streaks are related to snow growth during sedimentation. Both Thompson schemes only uses one mass–size relation for snow, while the P3 is more flexible: it uses a varying mass–size relation depending on whether the ice particle is unrimed, partially rimed, or fully rimed. This is the reason why the *dwr* corridor in P3 above the melting layer height is wider.

Below the melting layer, the observed *dwr* steadily decreases towards the ground. The schemes do not reproduce this very well. Even though the *dwr* decreases in all simulations, this decrease happens abruptly at the melting layer. The *dwr* directly below the melting layer height is very different between the simulations and the observations. However, including attenuation increases the simulated *dwr* and its variability, making it difficult to quantify *dwr* deviations between simulations and observations as discussed below. Below the melting layer height, the simulated *dwr* stays more or less constant, while the observed *dwr* decreases towards the surface. In the P3 simulations (and weaker in the Morrison 2-mom scheme), the *dwr* even increases again towards the ground. At these heights, rain and graupel are the dominant species. The simulated increase of *dwr* towards the ground is likely a result of the simulated collection process: raindrops grow while falling by collecting smaller droplets. This is visible also directly in the rain PSD (see

Appendix C) and was discussed in Sect. 4.4.2. Conversely, the large particles precipitating from the melting layer seem to shrink towards the ground, perhaps by drop breakup or evaporation. The general magnitude of simulated *dwr* values near the surface is close to the observed again at around −3–10 dB.

Comparing *dwr* signatures without including attenuation gives insight into the details of the microphysics schemes but is not well suited for a direct comparison with radar observations because especially the Ka-band observations are potentially strongly attenuated. This would lead to an increase in *dwr*. Figure 4.12 shows the same *dwr* CFADs including attenuation. Obviously, attenuation drastically increases the variability in *dwr*. As a result, *dwr* values are scattered over larger ranges, partially masking the underlying fingerprints that were visible in the CFADs without attenuation. Furthermore, the lower number of observed profiles compared to the simulated profiles is still clearly visible. This is most prominent in the *dwr* CFAD but also in the CFADs of Z_e (Fig. 4.9) and Z_{DR} (Fig. 4.10). This is reminiscent of the large observational effort to collect targeted cell core RHI scans.

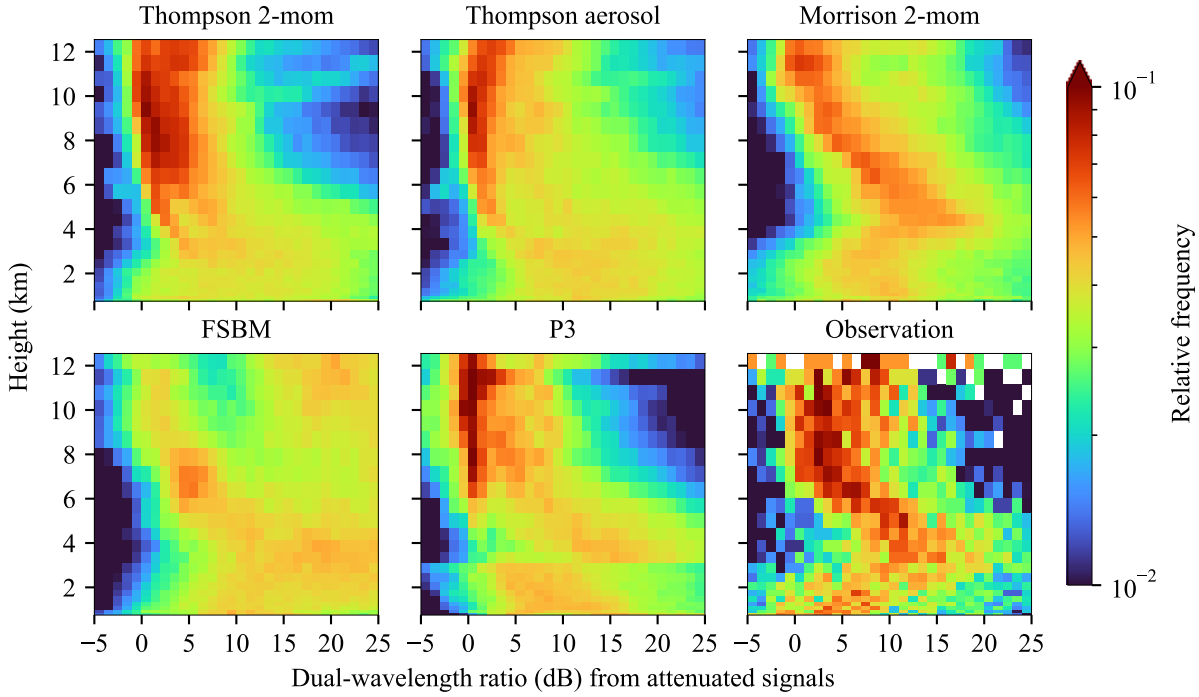

Figure 4.12: Contoured frequency by altitude diagrams (CFADs) of simulated and measured *dwr* with attenuation included over 5 convective days in 2019. Radar observations with POLDIRAD and MIRA-35.

4.5 The Influence of Cloud Microphysics Schemes on the Prediction of High-Impact Weather

Up to now, the focus of the analysis was laid onto understanding differences of observed and simulated macro- and microphysical signals. This last section of this chapter concentrates on the central aspect for the majority of the customers on the ground: a convective weather forecast for high-impact weather events. In Sect. 4.5.1 the area and frequency of simulated heavy rainfall events are compared against the observations. In the same way, hail and graupel events are evaluated in Sect. 4.5.2.

4.5.1 Heavy Rainfall Statistics

The objective of this study is to statistically evaluate microphysics schemes using polarimetric radar observations. To enable comparison between model and radar, either a radar signal must be simulated based on the model output, or information about hydrometeor classes must be obtained from the observed radar signals. These two approaches are combined here to statistically compare observations and model outputs to evaluate microphysical processes related to high-impact weather events: heavy rain and hail. To define a heavy rain or hail event, the HID algorithm of Dolan et al. (2013) was applied to the observed and simulated (with a radar forward operator) polarimetric signals in the same way. The frequency and area of heavy rain and hail events defined in this way are then statistically compared to analyze differences between model and observation and the influence of the microphysical processes. The statistics extend over 30 convection days. Since there are no ground-based observations available due to radar elevation, all analyses are restricted to an altitude level of about 1 km above Munich. This altitude is the lowest possible altitude at which there is complete radar coverage of Munich.

Statistics based on observed and simulated reflectivity

We begin the statistical analysis with an evaluation of the frequency and area of heavy rain events. The top row in Fig. 4.13 shows the frequency and area of rain events for different event strengths at an altitude of 1 km above Munich. The strength of the event is defined by the simulated or observed reflectivity. The total duration of a day when rain was classified above a certain reflectivity threshold is calculated. For the 30 d dataset, this gives a time series of 30 values.

The minimum, mean, and maximum of this time series are shown on the top left of Fig. 4.13 for both the simulations for the five microphysics schemes and the observations. Thus, one can compare the frequency of rain of different intensities. The maximum possible time is 24 h, which would correspond to rain for an entire day (for all 288 5 min steps) above the given reflectivity threshold. For the left column of Fig. 4.13, it does not matter how large the area was classified as rain during a time step as long as at least one pixel was classified as rain. The area of rain events is presented in the top right of Fig. 4.13. The term “area” here refers to the cross section area at 1 km altitude that was covered by the rain during a time step.

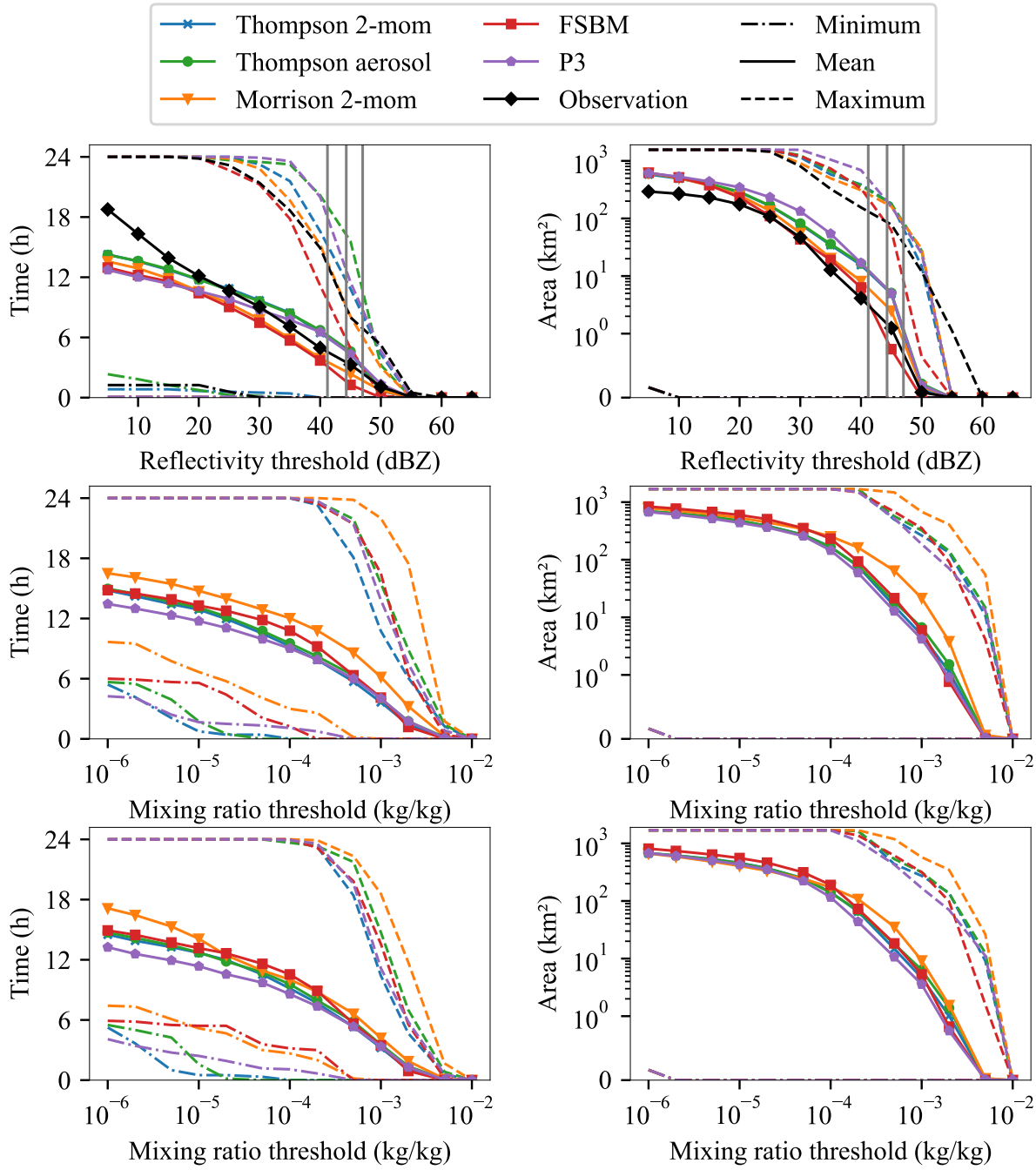

Figure 4.13: Daily duration (left column) and area (right column) of classified rain above various thresholds. Minimum (dashed-dotted line), mean (solid line), and maximum (dashed line) over the 30 d data set. Gray vertical stripes: thresholds for heavy precipitation (15, 25, and 40 mm h^{-1}) from the German Meteorological Service (DWD) after conversion to reflectivity (dBZ) using a Z–R relation. First row: statistics based on simulated and observed reflectivity thresholds at 1 km altitude. Simulated reflectivity from the Weather Research and Forecasting (WRF) model output after applying the Cloud-resolving model Radar SIMulator (CR-SIM). Second row: statistics based on mixing ratio thresholds at 1 km altitude. Third row: statistics based on thresholds for mixing ratio at the surface. The y-axis on the right side is logarithmically scaled, except for a small range around zero (0–1) with a linear scale.

The maximum possible area is 1800 km^2, which would mean that the Munich domain is completely covered by rain above the specified threshold. Both model output and radar observations provide data every five minutes. Figure 4.13 shows the minimum, mean, and maximum area over all time steps where rain was classified above the corresponding threshold. The total time with any rain somewhere in the domain averages to more than 13 h in all simulations and in the observations. This high number of rain events is a consequence of the fact that the data set consists specifically of days with convective precipitation. At the smallest reflectivity thresholds (5–10 dBZ), all schemes underestimate the occurrence of rain in the domain by about 5 h on average per day compared to radar observations. This weak precipitation is typically classified as drizzle. At the same time, the area of these drizzle events is larger in the simulations than in the observations. This is due to the fact that the radar observations are much more likely to show scattered and isolated grid cells classified as drizzle, while the simulations typically show somewhat larger, contiguous fields of precipitation. In part, this difference may be due to some clutter that could not be filtered out from the observations. In any case, these observed isolated drizzle clouds are usually very small and likely evaporate before they reach the ground. There are some arguments why these drizzle events are nevertheless important, even if the precipitation does not reach the ground, such as by affecting the water balance and turbulent dynamics (Wyant et al., 2007). In addition, drizzle is often poorly represented in NWP models (Wyant et al., 2007, Wilkinson et al., 2012). However, this issue is not considered to be the focus of this study and will not be discussed it in detail.

The gray vertical lines in Fig. 4.13 show the thresholds used by the DWD for heavy rainfall (15, 25, and 40 mm h^{-1} ; Deutscher Wetterdienst, 2022) after applying a Z–R relationship for convective precipitation (Woodley, 1970)

$$z_e = 300 \cdot {R_{rate}}^{1.4} , \tag{4.1}$$

where R_{rate} is the rain rate for heavy rain as defined by the DWD and z_e is the reflectivity in $mm^6\,m^{-3}$, which is then converted into logarithmic units in decibels

$$Z_e = 10 \cdot \log_{10}(z_e) . \tag{4.2}$$

The heavy rain thresholds of 15, 25, and 40 l m^{-2} are thus converted to reflectivity thresholds of 41.2, 44.3, and 47 dBZ. This gives an indication of the reflectivity thresholds that correspond to heavy rain. In these ranges, the cloud microphysics has a strong influence on the simulated rain events. The frequencies from the simulated heavy rain events scatter around the observed frequency, which is pretty much in the middle of the different simulations. However, the scatter is considerable, i.e., some of the simulations differ by 4 h in mean, which corresponds to a factor of more than 2 for the 41.2 dBZ heavy rainfall threshold and a factor of about 5 for the 44 dBZ threshold. All simulations produce rainfall areas that are, on average, larger than the observed rainfall areas, almost regardless of the reflectivity threshold. Interestingly, the same microphysics schemes that simulate heavy rain events most frequently also simulate the largest rain areas, i.e., the simulations using the P3 scheme and the two Thompson schemes.

The most important information from this section is that most schemes produce heavy rainfall that

is too large in area by a factor of up to four. The frequency of heavy rain events is more similar to observed events, but still scatters by a factor of up to 2 around the observations. In particular, for both Thompson schemes and the P3 scheme, this is a large overestimate of heavy precipitation events. These statistics are based on reflectivity thresholds. The question here is: will this also affect the amount of precipitation, i.e., rain mass? Reflectivity is disproportionately dominated by large drops compared to rain mass. So in order to relate these results to actual rain mass, the analysis from this section is repeated below, but based on thresholds for rain mass (or rain mass mixing ratio) instead of reflectivity.

Heavy rainfall statistics based on model mass mixing ratio

In the previous part, statistics of rain events of different intensity based on HID fields classified from (simulated) radar reflectivity fields were shown. To constrain the model output with radar observations, it is necessary to simulate reflectivities from the model output. A disadvantage of this procedure is that it relies on the radar forward operator. However, information about the simulated hydrometeors is also directly available in the model output in the form of the mixing ratios. In the following part, the analysis from the previous part is repeated with rain mass mixing ratio thresholds instead of reflectivity thresholds, to show how the analysis in reflectivity space is related to a direct analysis of the model output rain mass.

The middle row in Fig. 4.13 shows the same analysis as the top row, with the difference that this time the rain events are defined by the mixing ratio directly from the model output. The center left image shows how often rain was simulated above different mixing ratio thresholds. The center right image shows the covered area, following the same methodology as in the previous part. The analysis also takes place at an altitude of 1 km above the surface to guarantee comparability, even though the simulated mixing ratio data is available at the surface as well. Most of the schemes produce distributions of rain events with a similar pattern over the different mixing ratio thresholds, actually only the Morrison 2-mom scheme deviates noticeably and produces rain events of any magnitude (with respect to the mixing ratio) more frequently than the other schemes. At higher mixing ratio thresholds ($> 10^4\,\mathrm{kg\,kg^{-1}}$), these events are also simulated over larger areas in the Morrison 2-mom simulations than in the other simulations. This ultimately means that the Morrison 2-mom simulations produce a significantly larger mixing ratio, and especially so for the particularly intense precipitation events.

When comparing this to the top row, substantial differences are found. The schemes that overestimated heavy precipitation events the most when based on reflectivity thresholds (P3, Thompson 2-mom, Thompson aerosol-aware) simulated actually the least often heavy precipitation events when based on direct mixing ratio thresholds. Especially the conclusion that the P3, Thompson 2-mom, and Thompson aerosol-aware simulations simulate too much heavy precipitation is not visible at all from the model mixing ratio directly. How can this discrepancy be explained? The following two reasons account for this: 1) for liquid drops, mass mixing ratio depends to the third power ($\propto D^3$) on particle diameter, while reflectivity depends to the sixth power ($\propto D^6$) on particle diameter. Thus, the PSD plays an important role in inferring mass from reflectivity or vice versa. For example, PSD with many small particles and few large particles may contribute

significantly to the mass mixing ratio, but very little to reflectivity. 2) the HID algorithm always returns the dominant hydrometer class and not the mixture of all particles present in the volume. In contrast, the mixing ratio output by the model takes into account all simulated hydrometeors. This means that if rain is common in a scheme but is rarely the dominant class, then rain is strongly represented in mixing ratio analyses but poorly represented in the HID analysis.

The role of the particle size distribution

To test the hypothesis from above, rain PSDs were calculated for all microphysics schemes. The mean PSD over all time steps and all inner domain grid boxes at 1 km are shown in Fig. 4.14.

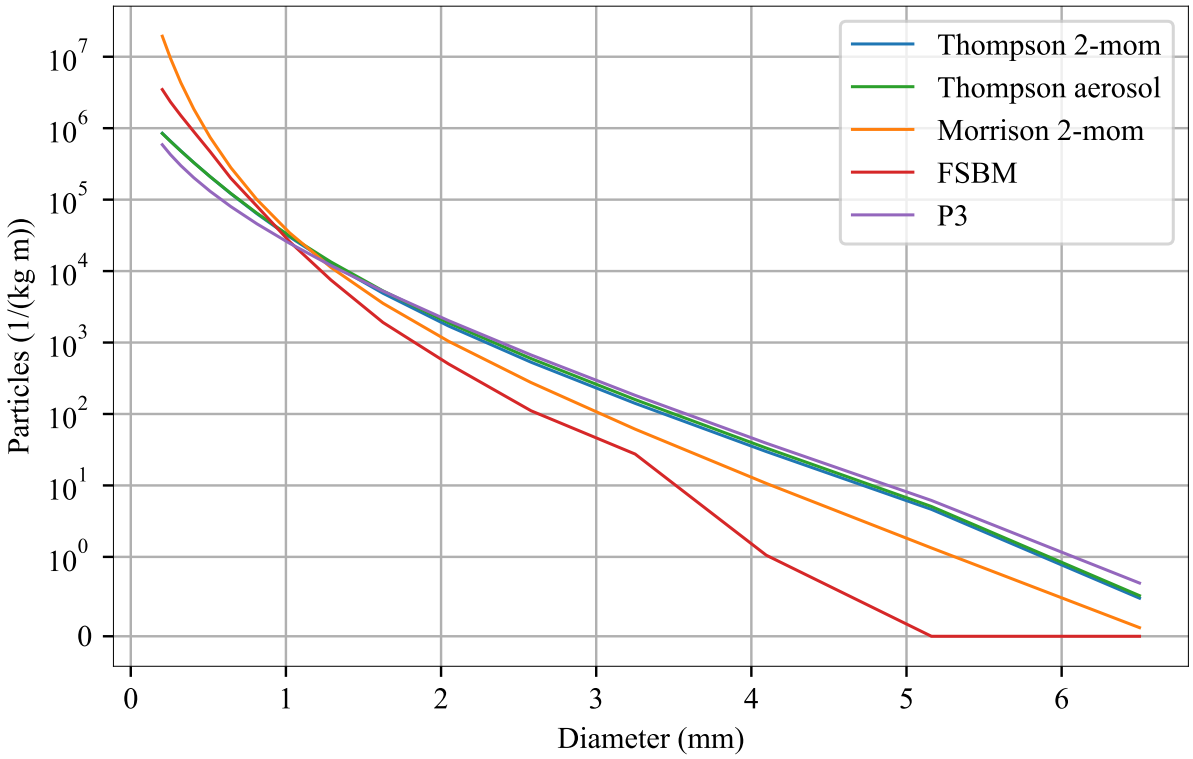

Figure 4.14: Mean rain particle size distribution (PSD) over all 30 days at 1 km altitude. The y-axis is logarithmically scaled, except for a small range around zero (0–1) with a linear scale.

The FSBM simulations provide total mixing ratios for a number of drop size bins as direct model output. From this, the number concentration of raindrops of a given size bin is calculated by dividing the given mixing ratio by the mass of a drop of the corresponding size bin. For the bulk schemes, the PSD was calculated according to the parameterization of the schemes by implementing the parameterization as described in the corresponding publication (Thompson et al., 2008, Morrison et al., 2009, Thompson and Eidhammer, 2014, Shpund et al., 2019, Morrison and Milbrandt, 2015) as well as directly from the code available on GitHub (Skamarock et al., 2019).

Because the bulk schemes do not actually have fixed size bins, the number concentration can be calculated for any drop size. To make the PSDs comparable, the number concentrations for the bulk schemes were calculated for the drop sizes that match the raindrop size bins of the FSBM scheme. Figure 4.14 shows the PSD over these 18 bins. It can be seen that, on average, the FSBM and Morrison 2-mom schemes produce raindrops of 1 mm and smaller much more frequently (by a factor of more than 10) for small diameters. The opposite is true for large raindrops greater than 4 mm, which were not simulated at all by the FSBM scheme. In principle, the FSBM can simulate larger raindrops, as the largest bin corresponds to raindrops of 6.6 mm diameter. According to Shpund et al. (2019), there is a drop break-up scheme applied that follows Kamra et al. (1991) and Srivastava (1971), which includes spontaneous breakup and collisional breakup. There is also a snow breakup scheme applied, which might limit the raindrop sizes for rain created from melting snow. Therefore, it seems likely that the PSD is the main reason for the different behaviors of the schemes in reflectivity space and mixing ratio space. The sheer amount of small droplets in the Morrison 2-mom and FSBM schemes thus contributes noticeably to the total mass, but less to the reflectivity, which is simulated much lower in comparison, especially in the FSBM scheme due to the lack of large raindrops.

This strongly suggests that it is not the produced rain mass that is the problem with the simulations, but rather the distribution of mass across drop sizes. Unfortunately, it is not possible to say with certainty what the PSDs looked like in reality during the 30 d data set because there are no direct measurements of the PSD available. But given that the FSBM scheme simulates high mixing ratio of rain mass, but at the same time produces too few heavy rain events based on the reflectivity produced, it stands to reason that this scheme generally produces too few large raindrops. The exact opposite is true for the P3, Thompson 2-mom, and Thompson aerosol-aware simulations. These results are consistent with the findings of the previous section, where vertical distributions of simulated differential reflectivity was statistically compared with the observed ones. In particular, the FSBM scheme did not produce larger differential reflectivity in the lower elevations, suggesting the absence of large drops in the FSBM, while the P3 and both Thompson schemes produced large differential reflectivity signals too frequently. A similar comparison of polarimetric radar signatures was performed by Wu et al. (2021) for a typhoon precipitation event in 2016. They noted that none of their simulations were able to successfully reproduce the observed polarimetric radar signatures. This was attributed to median raindrop sizes that are too large (Morrison 2-mom and Thompson 2-mom scheme), and to a simulated frequency of very large raindrops lower than observed (Thompson 2-mom scheme). In contrast, Putnam et al. (2016) found that both Morrison 2-mom and Thompson 2-mom produce reflectivity values that are too high, which they attributed to PSDs containing too many large drops, too much precipitation coverage, and, in the case of the Morrison 2-mom simulations, a bias due to wet graupel. With respect to this study, it can be confirmed that the simulations produce too much precipitation coverage, and it is suggested that there are too many large raindrops in the two Thompson simulations, which is consistent with Putnam et al. (2016) but in contrast to Wu et al. (2021). However, both studies evaluated the microphysics schemes using only case studies, which is not generally applicable to different weather situations. This shows an advantage of the statistical approach, which allows more robust conclusions.

The analysis to this point has been limited to an altitude of 1 km above the surface, limited by the radar observations. However, another question remains: does the analysis at 1 km altitude translate to precipitation at the surface? Precipitation on its way to the ground is affected by processes such as evaporation and drop sedimentation, and different microphysics schemes treat these processes differently. Therefore, the mixing ratio analysis is repeated, but with data from the surface, to relate the results from 1 km altitude to results at the surface.

Rain mass mixing ratio analysis at the surface

The bottom row in Fig. 4.13 shows the same analysis as the center row, except that this time surface mixing ratios are analyzed instead of 1 km altitude. At the surface, the Morrison 2-mom and FSBM simulations showed the most frequent and most widespread rain events, throughout most mixing ratio thresholds. This is in general agreement with the analysis at 1 km height. However, the difference, especially between Morrison 2-mom and the other schemes, becomes smaller. This suggests that rain within the Morrison 2-mom scheme undergoes stronger evaporation compared to the others. Given that the Morrison 2-mom scheme produced on average the highest number of very small rain droplets of 0.5 mm and smaller at 1 km altitude, a high evaporation rate is to be expected. Since the general ranking between the schemes is almost the same between 1 km altitude and the surface, the findings at 1 km altitude are arguably a good proxy for the surface. However, the difference between the schemes at the surface definitely becomes smaller, and all schemes produce frequency and area of rain events of similar magnitude.

Summarizing the results of the rainfall statistics, the following is noted: all schemes overestimate the area of heavy rain events based on reflectivity thresholds; P3 and the two Thompson schemes also overestimate the frequency of heavy rain events, while the FSBM and Morrison 2-mom schemes underestimate the frequency of heavy rain events. Further analysis of the rain mixing ratio and the calculated PSDs indicates that large raindrops that contribute strongly to high reflectivities are simulated too frequently in the P3, Thompson 2-mom, and Thompson aerosol-aware simulations, while large raindrops occur too infrequently in the FSBM simulations.

4.5.2 Hail and Graupel Statistics

So far, the focus has been exclusively on heavy rain events. However, hail events also have damage potential and therefore are of interest. The P3 scheme does not have a separate hail or graupel class. Therefore, to allow for a fair comparison between the schemes, all ice was included in this analysis. Given that the dataset consists of convective cases mainly in summer, most of the ice present at 1 km altitude and below is graupel or hail-like anyway. For completeness, the analysis restricted to graupel and hail only (and thus without the P3 scheme) is provided in Appendix D.

Statistics based on observed and simulated reflectivity

Figure 4.15 shows the area and frequency of these ice events in the same manner as Fig. 4.13 for rain. The choice of microphysics scheme has a significant impact on the ice statistics, across all reflectivity thresholds. The most extreme case is the FSBM scheme, which hardly produces any ice events at higher reflectivities. There is not a single time step within the 30 d dataset at which the FSBM scheme simulated ice grid cells of 35 dBZ or higher (top left image in Fig. 4.15).

However, most of the other schemes, and especially the Morrison scheme, also consistently show fewer ice events compared to the observations. Unlike the rain analysis, this is consistent across all reflectivity thresholds and not limited to the lower reflectivities. Only the P3 scheme is similar in terms of frequency, and for it only the highest reflectivity events ($\geq$ 55 dBZ) are too rare. None of the simulations, regardless of the cloud microphysics scheme, were able to reproduce these extreme events. This can have multiple reasons:

1. *Model resolution* Such high reflectivities require very large particles. For hail formation, for example, strong updrafts must be present. There is some discussion about the grid spacing required to properly represent these updrafts. Lebo and Morrison (2015) and Jeevanjee (2017), for example, show that a grid spacing less than about 250 m is required before some convective storm characteristics such as vertical velocity or convective core area converge, i.e., further decreasing the grid spacing has only a limited effect. This means that even the grid spacing of 400 m, which is much better than current weather models, may still be too large to correctly simulate the strongest hail events.

2. *Particle density.* The particle density strongly influences the reflectivity. All schemes except the P3 scheme consider graupel particles with a constant density of 400–500 kg m^{-3} and do not explicitly calculate hail[1]. Hail particles, however, are typically much denser than graupel. This means, if hail events are observed, the high hail density can lead to high observed reflectivities that cannot be reproduced by the simulations due to the lower assumed particle density. Only the P3 scheme has a more flexible approach that allows varying ice particle density reaching up to 900 kg m^{-3}.

[1] With the configuration that was used in this study.

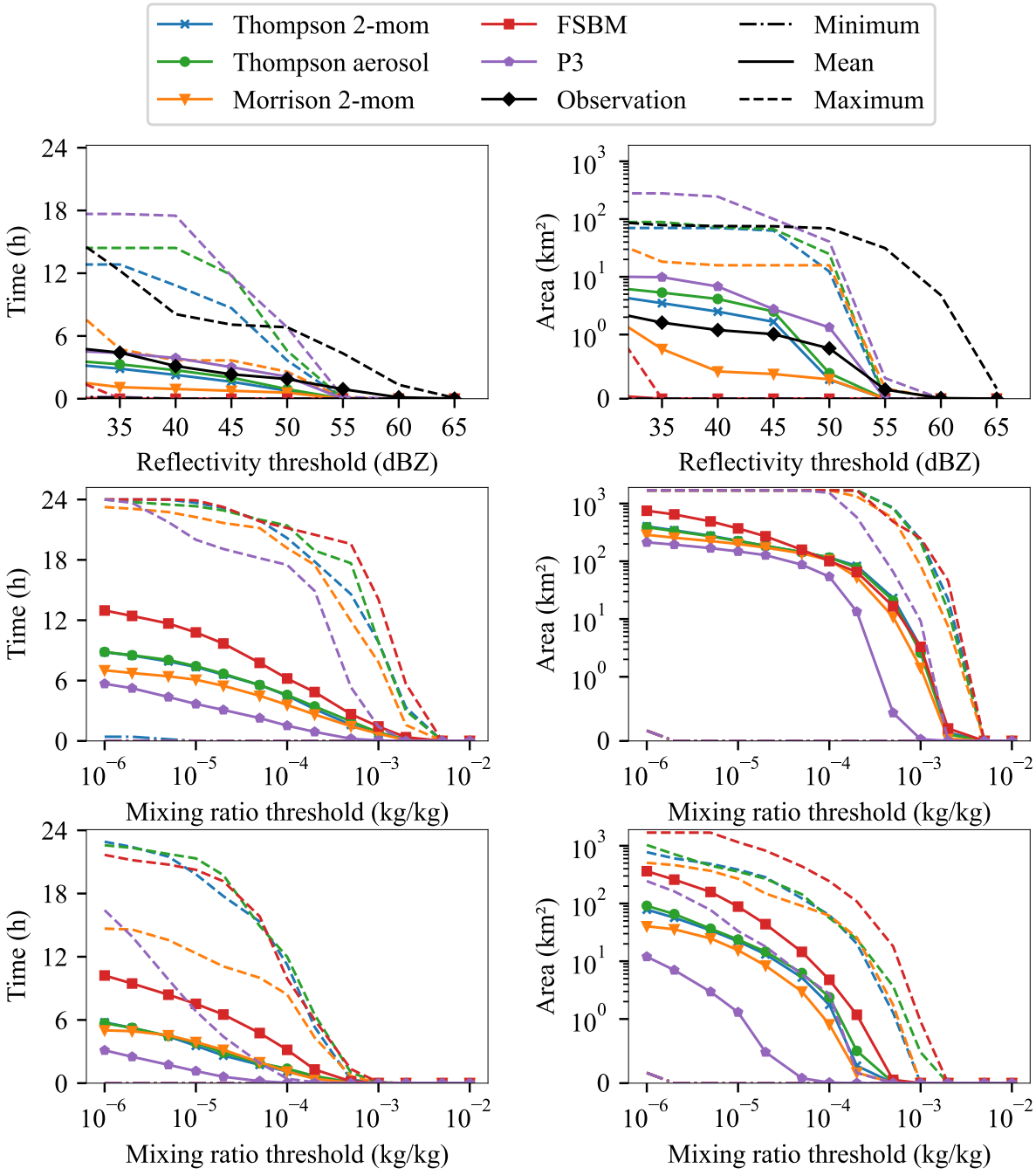

Figure 4.15: Frequency (left column) and area (right column) of ice events above various thresholds. Minimum (dashed-dotted line), mean (solid line), and maximum (dashed line) over the 30 d data set. First row: statistics based on simulated and observed reflectivity thresholds at 1 km altitude. Simulated reflectivity from the Weather Research and Forecasting (WRF) model output after applying the Cloud-resolving model Radar SIMulator (CR-SIM). Second row: statistics based on mixing ratio thresholds at 1 km altitude. Third row: statistics based on thresholds for mixing ratio at the surface. The y-axis on the right side is logarithmically scaled, except for a small range around zero (0–1) with a linear scale.

3. *Melting particles.* The applied microphysics schemes do not consider particles that are partially melted, all particles are either completely frozen or completely melted[2]. The radar forward operator CR-SIM does not apply a melting scheme either. That means, it is not only impossible to reproduce certain radar signatures related to melting (e.g., a "bright band"), but also the increase in reflectivity due to partially melted hail particles cannot be simulated. The highest reflectivity events observed could be due to partially melted hail particles, which would translate to an increase in reflectivity that is not reproducible by the schemes applied in this study.

It should be noted, however, that most schemes are quite capable of producing events of this magnitude at reflectivity thresholds of about 45 dBZ and 50 dBZ. However, most schemes underestimate the frequency and area of these events compared to radar observations. With a reflectivity threshold of 50 dBZ (which may be, in part, hail events), the P3 scheme is the only one capable of producing similar statistics in terms of area and frequency of hail/graupel events. The main difference of the P3 scheme with the other schemes is that instead of predicting the moments of multiple ice hydrometeor classes (including hail and graupel), this version of the P3 scheme uses only one ice class and instead predicts the properties of that ice class, such as the fraction of rime mass. This is more flexible and may better reflect the variability of real ice particles. With the configuration that was used in this study, P3 is also the only scheme that allows ice particles to reach densities up to $900\,\mathrm{kg\,m^{-3}}$, i.e., to simulate hail-like particles. While the Thompson 2-mom and Thompson aerosol simulations are at least able to reproduce the ice statistics at lower reflectivity thresholds, Morrison 2-mom and FSBM produce too few and too small ice events regardless of reflectivity threshold. The reasons for this likely are differences in PSDs in both cases. Morrison 2-mom and FSBM generally produce much lower reflectivity values, presumably because again the larger particles are absent. However, graupel density assumptions could also play a role. Both, Morrison 2-mom and FSBM assume a graupel density of $400\,\mathrm{kg\,m^{-3}}$. This is slightly lower than the $500\,\mathrm{kg\,m^{-3}}$ assumed by the two Thompson schemes.

Again, the question arises as to how statistics based on radar reflectivity translate to statistics based on mass mixing ratio. Therefore, it is continued with the analysis of ice in terms of mixing ratio, following the same structure as in the section on rain.

Hail and graupel statistics based on model mass mixing ratio

The middle row of Fig. 4.15, shows the same analysis as the top row, but this time for the model's initial ice mixing ratios. A clear ranking can be seen between the microphysics schemes, both for area and for the frequency of ice events, which is almost independent of the mixing ratio threshold: the FSBM simulations produced the most frequent and widespread ice events on average, while P3 produced ice events that were the smallest and least frequent. The majority of the ice events at the height of 1 km are graupel events, because slower falling ice, like aggregates or cloud ice, melts before it reaches the 1 km altitude. Comparing the mixing ratio analysis to the frequency and area statistics based on reflectivity in the previous section, again there is a stark contrast, especially for

[2] A newer version of the P3 scheme does include partially melted ice: Cholette et al. (2019).

the P3 scheme, where ice events are most common when obtained from radar reflectivity, and for the FSBM scheme, where ice events are the least common. Only for the Morrison 2-mom scheme, ice events are found less frequently, regardless of mixing ratio or reflectivity analysis. The FSBM scheme, on the other hand, is again likely missing the larger particles, since a large mass of ice particles is generated, but this does not translate into high reflectivities.

The ice statistics from this section were performed at 1 km altitude to ensure comparability with radar observations. Again, the question is whether the results from this section can be extrapolated to the surface. Therefore, the mixing ratio analysis is repeated at the surface.

Hail and graupel mass mixing ratio analysis at the surface

The bottom row in Fig. 4.15 shows the same analysis as the middle row, except that this time the mixing ratio is analyzed at the surface rather than at 1 km altitude. It can be seen that the FSBM scheme at the surface simulates the most frequent and widespread ice events, regardless of the reflectivity threshold, followed by the two Thompson schemes and the Morrison 2-mom scheme. The least frequent and also the smallest ice events are simulated by the P3 scheme. This ranking is the same as at 1 km altitude, indicating that the findings from 1 km altitude are approximately applicable to the surface as well. However, the P3 scheme simulates much smaller areas of ice at the surface than at 1 km altitude. This suggests that the melting process in the P3 scheme is stronger than in the other schemes. However, since there are no measurements of the PSD at the surface available, it is impossible to say whether these high melting rates are realistic.

In summary, for the ice statistics, no scheme is able to reproduce the most extreme reflectivity statistics of greater than 55 dBZ, which might be a problem with density assumptions, the absence of partially melted particles in the simulations or a resolution issue. Hail/graupel at reflectivity thresholds of 45–50 dBZ is correctly reproduced only by the P3 scheme. The other schemes, especially Morrison 2-mom and FSBM, underestimate the frequency and area of ice events regardless of reflectivity threshold. Analysis of the ice mixing ratio directly from the model output suggests that the FSBM scheme produces a high ice mixing ratio, but this is not correctly distributed over the particles sizes and likely the larger graupel particles are missing.

Chapter 5

Discussion

The representation of cloud microphysics in numerical weather prediction (NWP) models is a major source of uncertainty in precipitation forecasts (Morrison et al., 2020, Fan et al., 2017). This is partly due to fundamental gaps in our knowledge of the underlying microphysical processes in clouds, due to the difficulty of observing these processes directly and the complexity of microphysical interactions (Morrison et al., 2020). Microphysical processes occur on small scales of millimeters and less and are usually parameterized by cloud microphysics schemes in numerical weather models. A promising approach to evaluating these schemes are polarimetric radar observations (Ryzhkov et al., 2020), which are sensitive to many of the hydrometeor properties, such as particle shapes, sizes, densities, and more. Convective weather situations are a particular challenge in forecasting. Up to today, convective weather predictions are accurate only up to time scales of a few hours (Zhang et al., 2015, 2016). The majority of existing studies use single case studies to analyze the performance of cloud microphysics schemes. Given the variability of weather situations, a statistical approach is more robust in evaluating microphysics schemes, but is also associated with considerably more effort. In this dissertation, polarimetric radar observations and dual-wavelength radar observations are used as an observational basis for statistical evaluation of cloud microphysics schemes of varying complexity over 30 convective measurement days.

A methodological framework was presented that allows for a statistical comparison of polarimetric dual-wavelength radar observations with NWP model output. Targeted dual-wavelength observations of convective cell characteristics in the vicinity of Munich over a significant fraction of cell lifetime have been established. Cell-specific observations of a Ka-band and two C-band radars were provided for simulations and observations using a polarimetric radar forward operator and automatic cell tracking. The total data set presented includes 30 convective days of simulation and radar observations of the polarimetric radar in Isen, operated by the German Meteorological Service (Deutscher Wetterdienst, DWD). On five of those days, targeted observations were performed by two additional radars at C- and Ka-band, adding up to about 1300 range height indicator (RHI) profiles of dual-wavelength observations of convective clouds. A convection-permitting Weather Research and Forecasting (WRF; Skamarock et al., 2019) model setup over Munich was implemented with a grid spacing of 400 m. WRF simulations were conducted with five different microphysics schemes of varying complexity: three two-moment bulk schemes (Thompson et al.,

2008, Thompson and Eidhammer, 2014, Morrison et al., 2009) the FSBM and the "Predicted Particle Properties" (P3; Morrison and Milbrandt, 2015) scheme. The "Cloud-resolving model Radar SIMulator" (CR-SIM; Oue et al., 2020) was applied that provides polarimetric radar variables from model output. The cell tracking algorithm "TINT is not TITAN" (TINT; Raut et al., 2021) was applied on radar and model data in the same way to allow for comparison of convective cell characteristics. The hydrometeor identification (HID) algorithm of Dolan et al. (2013) was applied to simulated as well as observed radar signals to identify dominant hydrometeor classes and define heavy rain or ice events. The 30 d dataset was then analyzed in several ways to evaluate cloud microphysics schemes of varying complexity with the polarimetric and dual-wavelength radar observations. First, macrophysical convective cloud properties were compared, i.e., cloud geometry or the number of convective cells, their size, strength, or lifetime. Second, the vertical distributions of the simulated polarimetric radar signals were compared with the observed signals, allowing conclusions about microphysical aspects, such as particle size distributions (PSDs) or particle densities. Finally, the influence of the microphysics schemes on the model's ability to predict high-impact weather events, i.e., hail and heavy precipitation, was analyzed by statistically comparing the frequency of these events and the horizontal area they cover. The results obtained in this way will be discussed in the following, to answer the research questions stated originally the introduction.

Scientific objective 1: Can polarimetric radar observations provide sufficient microphysical information to statistically evaluate microphysics schemes?

In this dissertation, a unique approach that combines polarimetric and complementary dual-wavelength radar observations for a statistical evaluation of microphysics schemes was presented. It was shown how weather simulations with varying microphysics schemes produce varying polarimetric and dual-wavelength radar signatures. In comparison to the radar observations, these helped to identify several simulation aspects with the potential for improvement.

Macrophysical cloud properties

The application of an automated cell tracking algorithm (Raut et al., 2021) on simulated and observed fields of reflectivity facilitates objective comparison on the basis of convective cell objects. In general, simulations showed too few convective cells. The difference is mainly caused by missing weak cells with cell core heights between 3–4 km. This is attributed to grid resolution issues. The NWP model applied here has a grid spacing of 400 m, which is about five times better than the resolution at which current operational weather models operate (e.g. ICON-DE at 2.2 km, Zängl et al., 2014). However, this still means that only convective cells larger than at least 2 km are effectively resolved (Skamarock, 2004) and smaller cells might not be represented by the model.

Other problems involved statistics of maximum reflectivity or height of convective cell cores. The Thompson 2-mom and Thompson aerosol-aware schemes produced convective cell cores with reflectivities of 50 dBZ up to an altitude of 10 km. This is unrealistically high and strong compared to radar observations. The P3 scheme, on the other hand, appears to reproduce the cell core structure best. The reflectivity bias of the two Thompson schemes was found to be mainly caused by graupel. However, up to this point, it was not possible to separate possible sources of error based on radar reflectivity alone; the simulated particle number concentration, size, or density could all lead to an overestimation of the reflectivity in ice. Therefore, statistical and vertical distributions of polarimetric and two-wavelength radar variables were analyzed. Polarimetric and dual-wavelength radar variables are sensitive to many of the particle properties, such as particle phase, density, orientation, shape, or number concentration. This can be used to find out the underlying microphysical causes for the observed deviations. The resulting conclusions regarding the microphysical aspects of the simulations are discussed below.

Particle size distributions

Below the melting layer height, the radar signal distributions are dominated by rain. At this height, most schemes show a high bias of radar reflectivity. Statistical distributions of simulated differential reflectivity (Z_{DR}) below the melting layer height revealed that all schemes except the FSBM scheme produce Z_{DR} signals within rain with too much spread. This is attributed to the assumed exponential (Marshall–Palmer) rain PSD producing too many large and too few small droplets. The FSBM scheme has the advantage of explicitly resolving the PSD, which better

reflects the high occurrence of small rain droplets. Direct analysis of the simulated rain PSDs shows that the FSBM scheme on average produces more small rain droplets of 1 mm and smaller by a factor of up to 10. However, at the same time the FSBM scheme completely misses large raindrops of more than 4 mm in size, likely as a result of the drop breakup scheme applied. This translates into the inability of the FSBM scheme to produce high-impact precipitation events, defined as rain events with reflectivities of 41 dBZ or more. P3, Thompson 2-mom, and Thompson aereosol-aware simulations on the other hand overestimate the frequency of heavy rain events based on reflectivity thresholds by a factor of up to 2 compared to radar observations. At the same time, these schemes produce the fewest heavy rainfall events based on simulated mixing ratio thresholds. This leads to the conclusion that it is not the produced rain mass that is the problem, but rather the distribution across drop sizes; compared to the radar-observed heavy rain events, the P3, Thompson 2-mom, and Thompson aerosol-aware schemes produce large raindrops too frequently, while the FSBM simulations produce too few. The results related to the Thompson 2-mom and Morrison 2-mom schemes are in conflict with a previous study by Wu et al. (2021), but are consistent with Putnam et al. (2016), highlighting the problem of evaluating microphysics schemes using case studies and demonstrating the importance of statistical evaluation as in this study.

Above the melting layer, all schemes except the P3 scheme simulate unrealistic high reflectivities, partly over 45 dBZ, related to graupel. An overestimation of reflectivity can in principle be produced by simulation of too many, too large, or too dense particles. Vertical, statistical distributions of the dual-wavelength ratio (dwr) allow analyzing the effect of the particle sizes more directly, because dwr is independent of the particle number concentration. These distributions were best reproduced by the P3 scheme, which seems to better reproduce the variability of real ice particles. Furthermore, especially the Thompson aerosol-aware scheme, but to a lesser extent also the other schemes (except P3) produced dwr signals above the melting layer height that were too high. This leads to conclude that the unrealistic high reflectivities above the melting layer height are related to the mean graupel size that is simulated too large by all schemes except the P3. There are other studies that found an overestimation of reflectivities in the ice phase for case studies and attribute this to graupel or snow, depending on the microphysics scheme. Varble et al. (2011) for example, used C-band radar observations to evaluate cloud microphysics schemes and find a high reflectivity bias in ice. They suggest that the assumed PSD is unrealistic, but since the conclusions are based on reflectivity, density, number concentration, or size influences cannot be disentangled completely. Stanford et al. (2017) also find a high ice reflectivity bias in their simulations of a deep convective system. By retrieving ice PSDs from aircraft measurements, they could clearly attribute this to ice particles that are simulated too large. The analysis in this work demonstrates that microphysical conclusions like that can be drawn from polarimetric and dual-wavelength radar observations, which are associated with less effort than airplane campaigns and provide a better measurement coverage.

Density assumptions

None of the simulations were able to produce high-impact weather events of more than 55 dBZ, even though they have been observed during the evaluation period. This might be related 1) to limitations due to model resolution, 2) to density assumptions that are not representative for high density hail-like particles, or 3) the absence of partially melted particles in the simulations. Most likely seem issues related to density assumptions (2). Radar reflectivities higher than 55 dBZ are typically related to hail events, due to their high density of about 900 $\mathrm{kg\,m^{-3}}$. Most of the microphysics schemes applied in this work, however, are not able to produce high density particles like hail, and instead use a graupel class with lower densities of 400 or 500 $\mathrm{kg\,m^{-3}}$. This makes it impossible for these schemes to reproduce reflectivities produced by high density particles such as hail. The only scheme in this work capable of simulating higher density particles is the P3 scheme. At reflectivity thresholds of 45–50 dBZ, which might be in part hail events, the P3 scheme is the only scheme that was able to reproduce the observed statistics ice statistics. This suggests that the more flexible approach of ice particle density that is applied by the P3 scheme does translate into the ability to better reproduce radar signatures of hail and graupel events.

Can polarimetric radar observations provide sufficient microphysical information to statistically evaluate microphysics schemes? The analysis in this dissertation should give a clear answer: yes! By using a combination of polarimetric and dual-wavelength radar variables, this work showed how conclusions can be drawn about microphysical aspects of the simulations, such as the simulated PSD or the applied density assumptions.

Scientific objective 2: Does greater complexity in microphysics schemes improve numerical weather prediction of convective weather?

Microphysical processes are very complex, due to the high variability of particles and the many small-scale interactions involved. Ice particles are especially difficult to handle, because they can take on many different shapes and particle densities (Morrison et al., 2020). Microphysics schemes of varying complexity are available, that attempt to represent these processes in a NWP model. More complex schemes require also more computational effort, which is often the limited resource in NWP. A more complex scheme must therefore provide significant better results to justify its use. However, it is not clear that more complex schemes necessarily provide better results. One of the most complex types of schemes are spectral bin schemes that resolve the PSD explicitly and require high computational effort (Khain et al., 2015). There are some intercomparison studies that find bin schemes to give better results compared to more traditional "bulk" schemes (e.g. Fan et al., 2015, Li et al., 2009, Khain et al., 2015). However, other studies demonstrate that the spread among different bin schemes is equally large compared to the spread between bulk schemes (vanZanten et al., 2011, Xue et al., 2017) or find no clear advantage of bin schemes over bulk schemes in ice microphysics dominated convection simulations (Han et al., 2019, Stanford et al., 2017). To evaluate, how the added complexity improves the prediction accuracy for convective weather situations, 5 different microphysics schemes of varying complexity have been applied. Three of these schemes, the Thompson 2-mom, Thompson aerosol-aware, and Morrison 2-mom, are two-moment bulk schemes that predict the mass and number concentration of several hydrometeor classes. Both Thompson schemes are two-moment only for rain and cloud ice, making them the least complex schemes of the applied schemes. The FSBM scheme, on the other hand, requires by far the highest computational effort because it is a bin scheme in which the PSD is resolved with a number of 33 bins, and each bin requires additional calculations. The P3 scheme is also a bulk scheme, but deviates from the traditional schemes by using only one ice class. Instead, this scheme predicts properties of that ice, such as the riming mass fraction. This makes the P3 scheme somewhat more complex compared to the traditional bulk schemes, but the computational effort is still much lower compared to the FSBM scheme.

Can NWP forecasts be further improved by applying more complex microphysics schemes? The analysis in this dissertation does not show a clear advantage of more complex schemes; there are significant deviations from observations for all the applied schemes. The FSBM scheme, which is the most complex scheme of the selection in this work, arguably performs worse in many of the evaluations applied here, and only really shows an advantage in producing a more realistic number of small rain droplets. The P3 scheme, on the other hand, does seem to produce more realistic ice microphysics in comparison to the other applied schemes. The fact that the most complex scheme is not always producing the best results shows that simply increasing the complexity does not necessarily improve predictions. First, the microphysical processes need to be better constrained, and new observations are needed to provide the necessary information. In this work, the potential of polarimetric radar observations has been shown to do just that, and it is proposed they be further explored.

Remaining challenges

Using the framework presented in this work, there are some challenges for the evaluation of the microphysics schemes' performance. Using a large data set provides the possibility of a statistical evaluation. Thus, it can provide a correct general overview of the schemes' performance. On the other hand, considering long periods of time, multiple different weather situations produce convective cells of varying types. In this analysis, these are all analyzed together. This introduces ambiguities, and some individual microphysical aspects might be disguised by internal variability of convective situations in the data set. A solution would be a separation of different convective cloud types, e.g., by classifying into shallow, congestus, or deep convective clouds (e.g., Matsui et al., 2009). Classifications into weak/strong forcing situations could also be of interest, to analyze the effect of, e.g., frontal systems on the distribution of radar signals.

Furthermore, a radar forward operator was used for the analysis in this study. This is a useful tool to simulate the expected radar signals using the model data. However, it makes broad assumptions about the aspect ratio, orientation, shape, and density of the particles. Therefore, the application of these fixed relations inevitably results in the simulated particle properties not exhibiting the same variability as in nature. In addition, the radar forward operator applied in this study does not consider mixed-phase particles. For future evaluations, either a microphysics scheme that is able to simulate melting particles or a radar forward operator that applies a melting scheme should be considered. For example, a new version of the P3 scheme was recently developed that does include partially melted ice (Cholette et al., 2019). Finally, there is more noise in the radar statistics compared to the simulation statistics (for example, Fig. 4.9) due to the lower number of data points available from the observations. This could partially mask microphysical fingerprints, reminiscent of the large observational effort to statistically compare convective cloud characteristics. More dual-wavelength data are needed to compare radar observations and a model for convective weather situations with more confidence.

Relating radar-derived weather statistics to precipitation statistics at the surface is challenging. Although the simulations suggest that the mixing ratio at 1 km altitude is strongly related to the mixing ratio – and hence precipitation rate – at the ground, there are processes such as evaporation, drop breakup, or self-collection that affect this. In special cases, it is certainly possible for these processes to significantly change the precipitation rate. Therefore, one always has to rely on a model that correctly simulates these processes when radar measurements are used to make statements about precipitation on the ground. Furthermore, in this study, a HID algorithm to classify the predominant hydrometeors in the radar observation volumes was applied. This algorithm is based on theoretical scattering simulations and determines only the dominant hydrometeor class. This makes it difficult to relate the radar-based results to precipitation rates. It would be very helpful if, in addition to the dominant hydrometeor class, the fraction of each hydrometeor or even the corresponding mixing ratio was also derived from the polarimetric radar variables. Within a subproject of the German Research Foundation (Deutsche Forschungsgemeinschaft, DFG) Priority Programme 2115 PROM (Polarimetric Radar Observations meet Atmospheric Modelling – Fusion of Radar Polarimetry and Numerical Atmospheric Modelling Towards an Improved Understanding of Cloud and Precipitation Processes; Trömel et al., 2021), a HID algorithm is

currently being developed for this purpose. This algorithm is based on a clustering approach and an algorithm for quantifying the mixing ratio following Grazioli et al. (2015), Besic et al. (2016), and Besic et al. (2018), aiming to calculate the mixing ratios of hydrometeor classes as well. Thus, mixing ratios derived from the radar signal could be directly compared with the mixing ratios simulated by the model.

Appendix A

Simulation and Observation Dates

Table A.1: List of convective days that were used in the analyses. Strategy A always refers to the whole day.

Date	Strategy
29.04.2019	Strategy A
06.05.2019	Strategy A
28.05.2019	Strategy A, Strategy B (11:25 to 14:00 UTC)
29.05.2019	Strategy A
11.06.2019	Strategy A
12.06.2019	Strategy A
21.06.2019	Strategy A, Strategy B (14:40 to 17:25 UTC)
01.07.2019	Strategy A, Strategy B (11:20 to 16:50 UTC)
07.07.2019	Strategy A, Strategy B (09:20 to 15:10 UTC)
08.07.2019	Strategy A, Strategy B (09:00 to 14:00 UTC)
17.06.2020	Strategy A
20.06.2020	Strategy A
27.06.2020	Strategy A
28.06.2020	Strategy A
29.06.2020	Strategy A
01.07.2020	Strategy A
10.07.2020	Strategy A
11.07.2020	Strategy A
23.07.2020	Strategy A
24.07.2020	Strategy A
26.07.2020	Strategy A
28.07.2020	Strategy A
01.08.2020	Strategy A
02.08.2020	Strategy A
03.08.2020	Strategy A
18.08.2020	Strategy A
17.09.2020	Strategy A
22.09.2020	Strategy A
23.09.2020	Strategy A
12.10.2020	Strategy A

Appendix B

Euler View on the 1st of July 2019 Case

In Fig. 4.5 (Sect. 4.3), an example of a tracked convective cell was shown. The corresponding Eulerian view, that includes the simulated reflectivity over the entire domain, is shown below. Figure 4.5 refers to cell number 22 in the figure below.

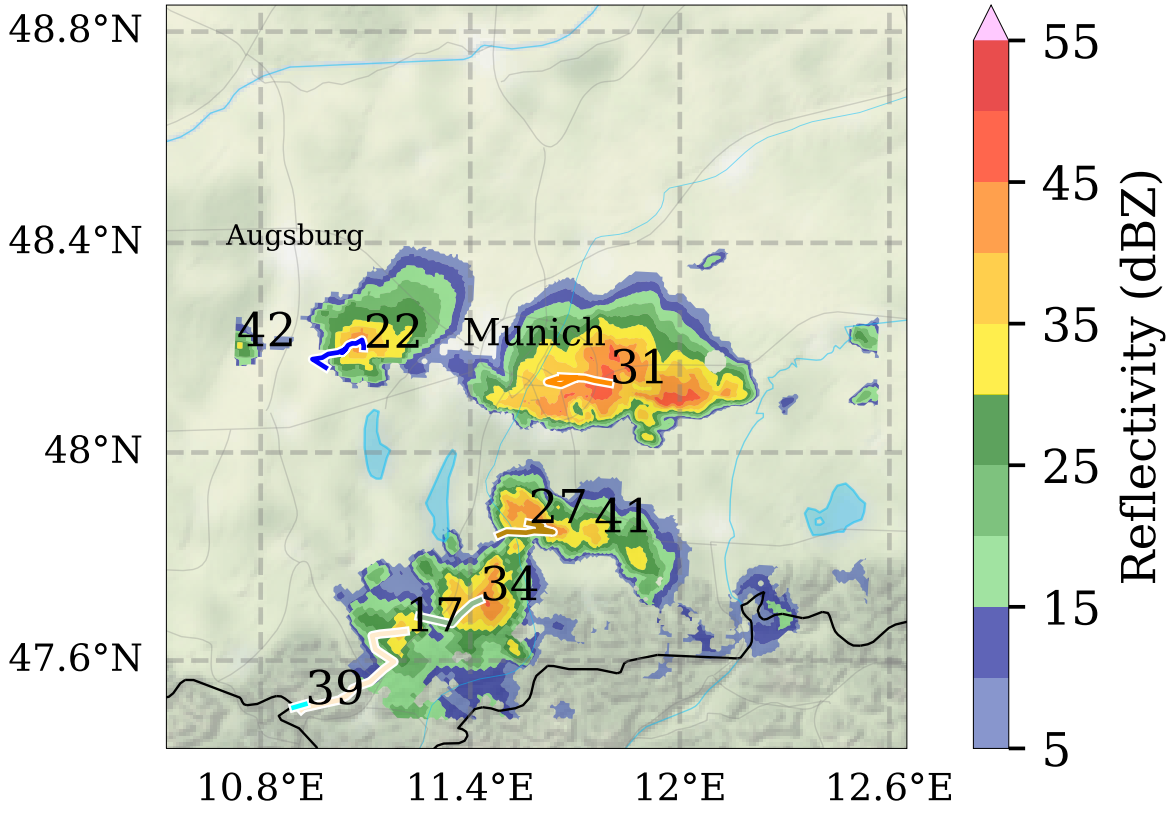

Figure B.1: Eulerian view of the situation corresponding to the convective cell shown in Fig. 4.5 on July 1, 2019, 13:35 UTC.

Appendix C

Hydrometeor Class CFADs

CR-SIM calculates radar signals for the single hydrometeor classes independently, next to the total signal of all hydrometeors together. Below are CFAD of the signals calculated from the most relevant hydrometeor classes. The CFADs are shown on the original WRF grid and without attenuation correction. The FSBM simulation sometimes showed spurious rain signals on the highest levels (> 10 km). Sometimes there are small numbers of rain drops present in the largest bins, even though the mass mixing ratio of rain is 0 kg kg^{-1} in the FSBM simulation. This is considered an error with no physical meaning.

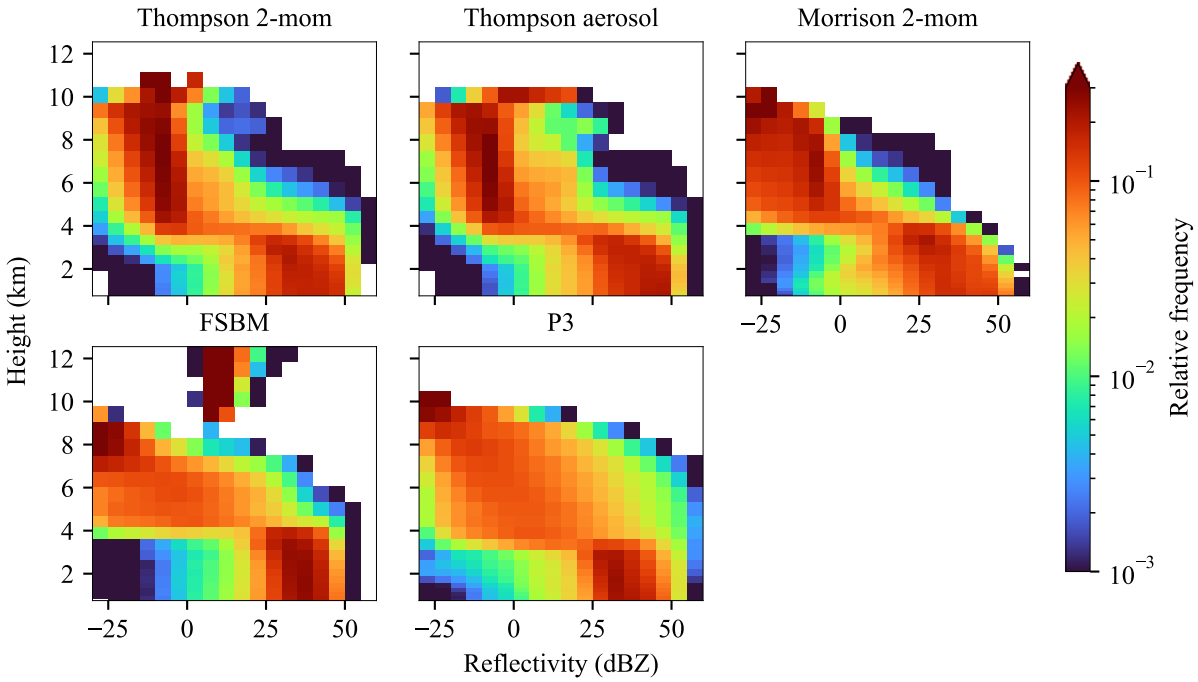

Figure C.1: Contoured frequency by altitude diagrams (CFADs) of simulated reflectivity of the rain hydrometeor class over 5 convective days in 2019.

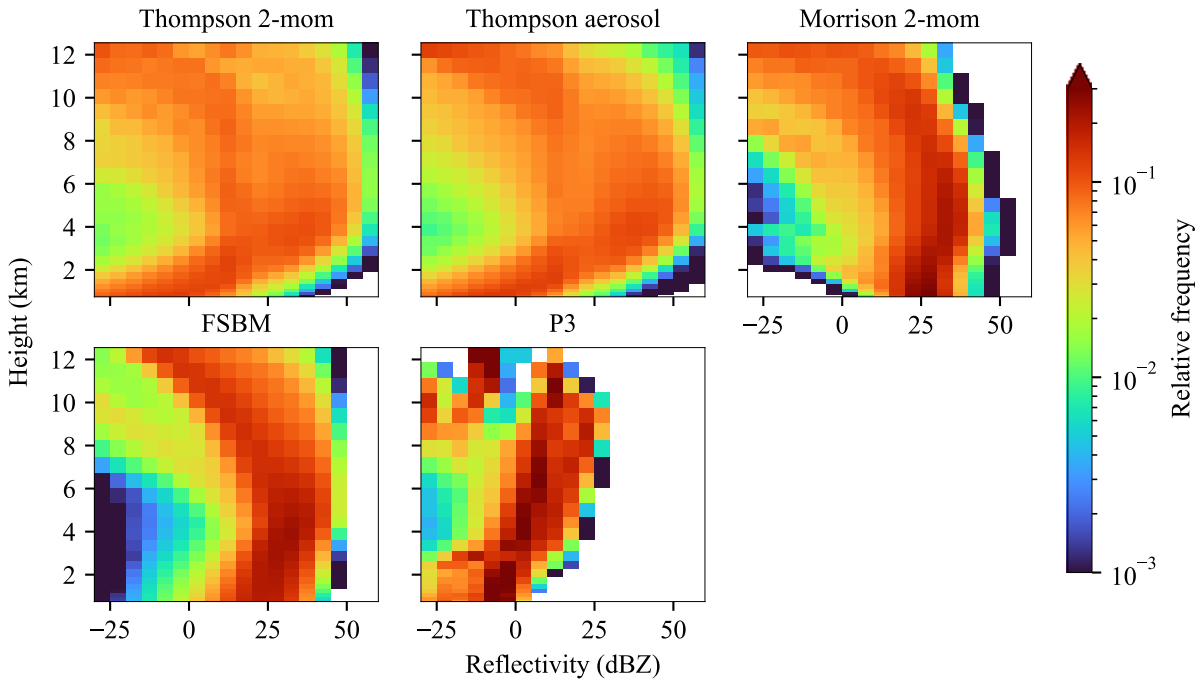

Figure C.2: Contoured frequency by altitude diagrams (CFADs) of simulated reflectivity of the graupel hydrometeor class over 5 convective days in 2019.

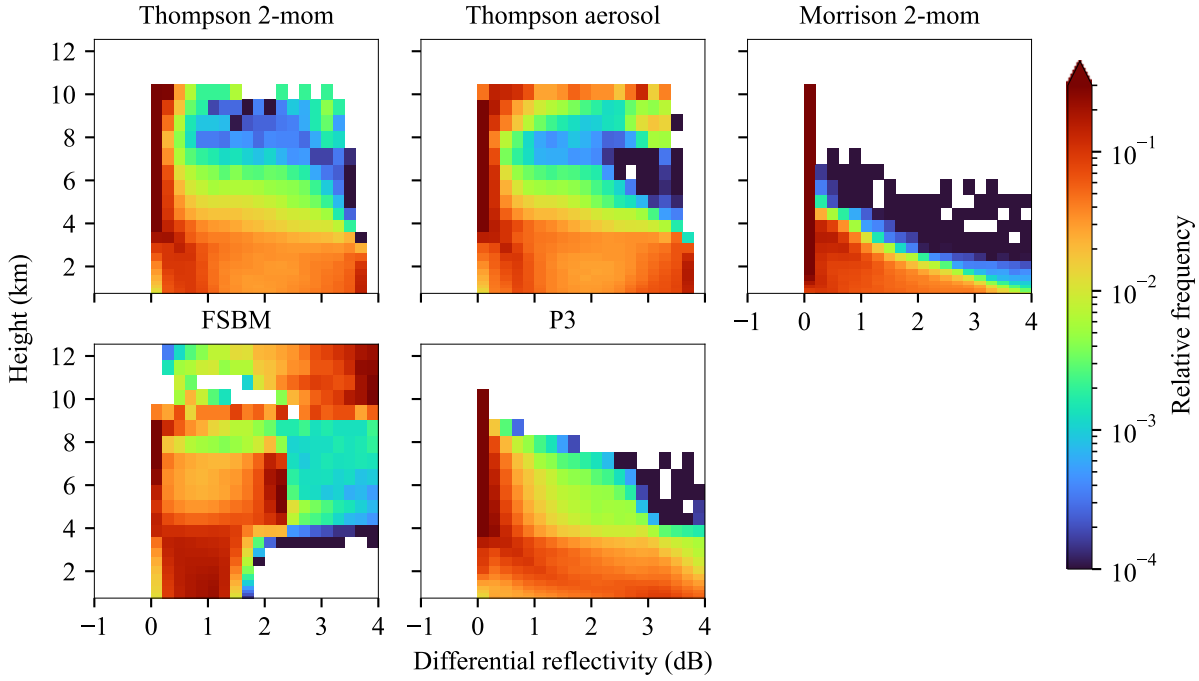

Figure C.3: Contoured frequency by altitude diagrams (CFADs) of simulated differential reflectivity of the rain hydrometeor class over 5 convective days in 2019.

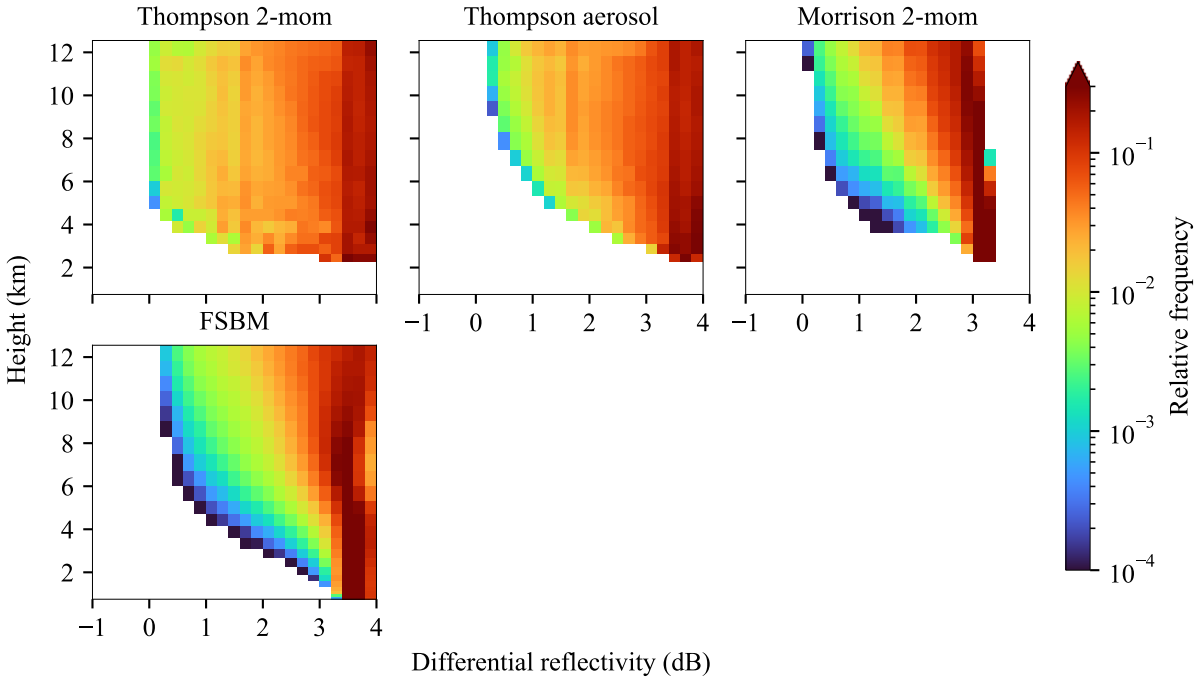

Figure C.4: Contoured frequency by altitude diagrams (CFADs) of simulated differential reflectivity of the cloud ice hydrometeor class over 5 convective days in 2019. The P3 scheme does not provide the classical cloud ice category.

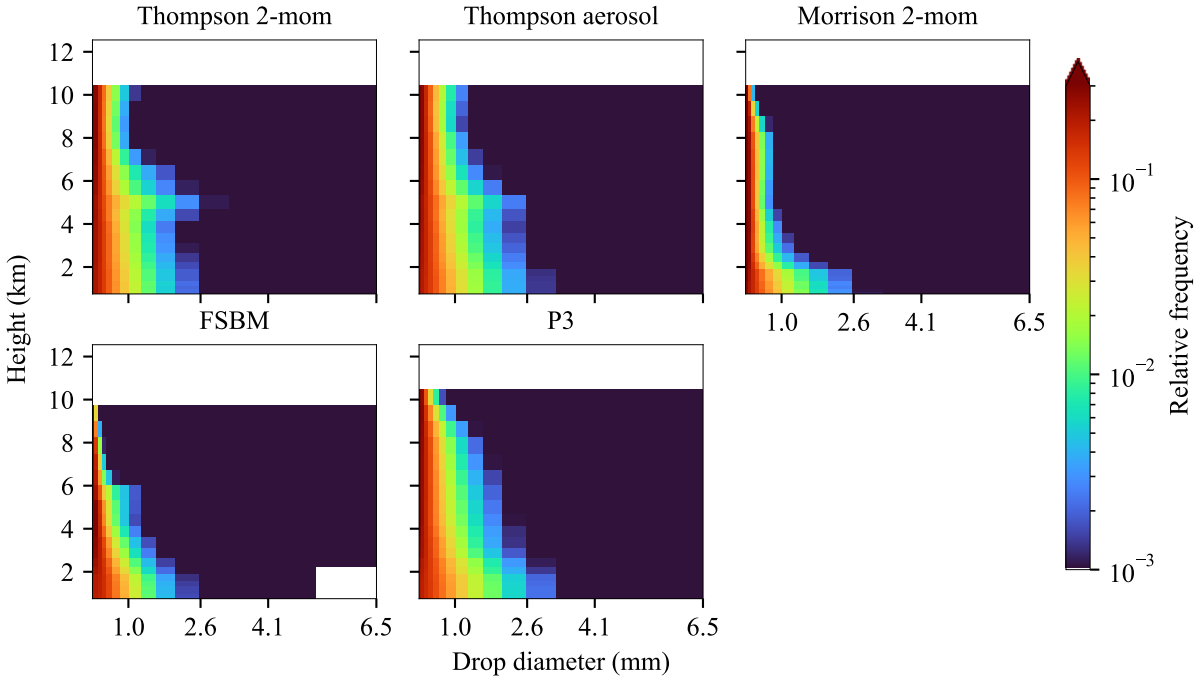

Figure C.5: Contoured frequency by altitude diagrams (CFADs) of simulated rain drop particle size distributions (PSDs) over during the measurement periods over 5 convective days in 2019.

Appendix D

Graupel and Hail Analysis

In Sect. 4.5, the frequency and area of ice events have been evaluated. In the analysis, all ice was included to guarantee a fair comparison between all microphysics schemes, which do not use exactly the same ice classes. The analysis was restricted to an altitude of about 1 km above the surface, which is about the height of the lowest elevation scan of the DWD ISEN radar above Munich. At this height, most of the ice, simulated and observed, is fast falling and thus graupel or hail-like anyway. For completeness, in Fig. D.1 below the same analysis is shown as in Fig. 4.15, but this time only including hail and graupel (and thus without the P3 scheme, which does not provide these classes).

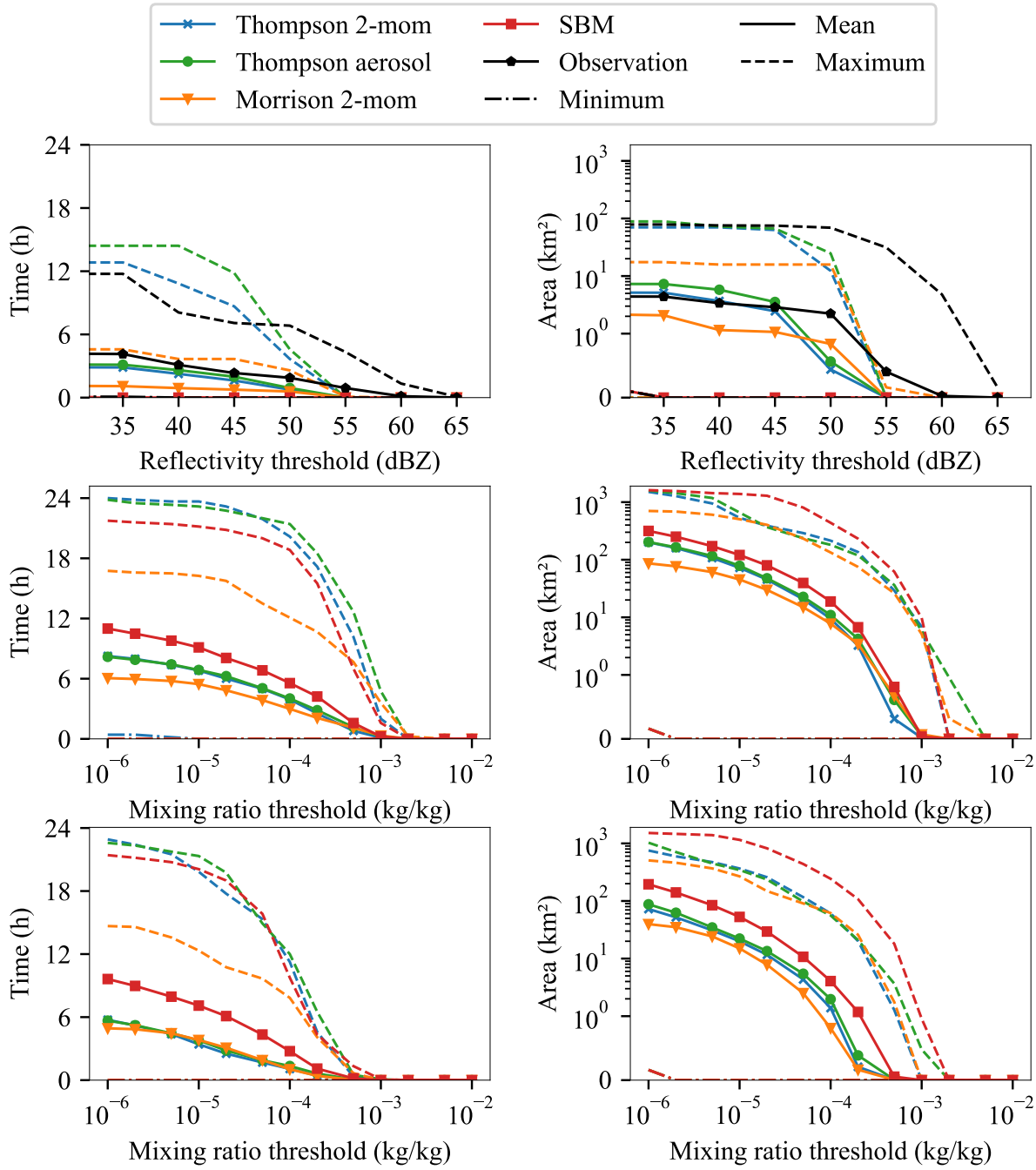

Figure D.1: Frequency (left column) and area (right column) of hail and graupel events above various thresholds. Minimum (dashed-dotted line), mean (solid line), and maximum (dashed line) over the 30 d data set. First row: statistics based on simulated and observed reflectivity thresholds at 1 km altitude. Simulated reflectivity from the Weather Research and Forecasting (WRF) model output after applying the Cloud-resolving model Radar SIMulator (CR-SIM). Second row: statistics based on mixing ratio thresholds at 1 km altitude. Third row: statistics based on thresholds for mixing ratio at the surface. The y-axis on the right side is logarithmically scaled, except for a small range around zero (0–1) with a linear scale.

Appendix E

WRF Namelist

WRF requires a namelist file that defines all necessary configurations, for example time or domain settings. On the following pages is a copy of the namelist that was used for all simulations of WRF in this dissertation. Only the mp_physics option was adjusted, according to the applied microphysics scheme. The example below is for the Morrison 2-mom scheme that has a WRF-ID of 10.

```
 &time_control
 start_year                          = __startYear__, __startYear__,
__startYear__, __startYear__,
 start_month                         = __startMonth__, __startMonth__,
__startMonth__, __startMonth__,
 start_day                           = __startDay__, __startDay__, __startDay__,
__startDay__,
 start_hour                          = __startHour__, __startHour__,
__startHour__, __startHour__,
 start_minute                        = 00, 00, 00, 00,
 start_second                        = 00, 00, 00, 00,
 end_year                            = __endYear__, __endYear__, __endYear__,
__endYear__,
 end_month                           = __endMonth__, __endMonth__, __endMonth__,
__endMonth__,
 end_day                             = __endDay__, __endDay__, __endDay__,
__endDay__,
 end_hour                            = __endHour__, __endHour__, __endHour__,
__endHour__,
 end_minute                          = 00, 00, 00, 00,
 end_second                          = 00, 00, 00, 00,
 interval_seconds                    = __metIncSec__,
 input_from_file                     = .true., .true., .true., .true.,
 history_interval                    = 60, 60, 60, 60,
 frames_per_outfile                  = 1, 1, 1, 1,
 restart                             = __isRestart__,
 restart_interval                    = __restartInterval__,
 override_restart_timers             = .true.,
 io_form_history                     = 2
 io_form_restart                     = 2
 io_form_input                       = 2
 io_form_boundary                    = 2
 debug_level                         = 0
 iofields_filename                   = "iofields" ,"iofields", "iofields",
"iofields",
 auxhist7_outname                    = "clouds_d<domain>_<date>",
 auxhist7_interval                   = 0, 0, 5, 5,
 frames_per_auxhist7                 = 1, 1, 1, 1,
 io_form_auxhist7                    = 2,
 /

 &domains
 use_adaptive_time_step              = .false.,
 step_to_output_time                 = .true.,
 target_cfl                          = 1.0, 1.0, 1.0, 1.2,
 max_step_increase_pct               = 5, 51, 51, 51,
 starting_time_step                  = -1, -1, -1, -1,
 max_time_step                       = 200, 40, 3, 4,
 min_time_step                       = -1, -1, -1, -1,
 adaptation_domain                   = 3,
 time_step                           = 60,
 time_step_fract_num                 = 0,
 time_step_fract_den                 = 1,
 max_dom                             = 3,
 e_we                                = 375, 221, 361, 196,
 e_sn                                = 375, 221, 361, 156,
 e_vert                              = 40, 40, 40, 40,
 num_metgrid_levels                  = 34,
 num_metgrid_soil_levels             = 4,
 dx                                  = 10000, 2000, 400, 400
 dy                                  = 10000, 2000, 400, 400
 grid_id                             = 1, 2, 3, 4,
 parent_id                           = 1, 1, 2, 2,
 i_parent_start                      = 1, 195, 76, 65,
```

```
 j_parent_start                      = 1, 147, 74, 20,
 parent_grid_ratio                   = 1, 5, 5, 5,
 parent_time_step_ratio              = 1, 5, 5, 5,
 feedback                            = 1,
 /

 &physics
 mp_physics                          = 10, 10, 10, 10,
 progn                               = 1, 1, 1, 1,
 prec_acc_dt                         = 60., 60., 60., 60.,
 ra_lw_physics                       = 4, 4, 4, 4,
 ra_sw_physics                       = 4, 4, 4, 4,
 radt                                = 5, 5, 5, 5,
 aer_opt                             = 3,
 sf_sfclay_physics                   = 5, 5, 5, 5, ! Ravans suggestion
 sf_surface_physics                  = 2, 2, 2, 2, ! NOAH
 sf_surface_mosaic                   = 1,
 sf_lake_physics                     = 1, 1, 1, 1,
 sf_urban_physics                    = 1, 1, 1, 1,
 bl_pbl_physics                      = 5, 5, 5, 5, ! MYNN 2.5
 bl_mynn_cloudpdf                    = 1,
 bl_mynn_cloudmix                    = 1,
 scalar_pblmix                       = 1,
 tracer_pblmix                       = 1,
! grav_settling                       = 0, 2, 2, 2 ! settling of fog / cloud
droplets
 bldt                                = 0, 0, 0, 0,
 cu_physics                          = 5, 0, 0, 0, ! Grell 3D
 cudt                                = 1,
 cugd_avedx                          = 1, ! set to 3 for 4km run, 1 for 36km
 ishallow                            = 0,
 iz0tlnd                             = 1, ! thermal roughness length over land
determined by vegetation type
 isfflx                              = 1,
 ifsnow                              = 1,
 icloud                              = 1,
 icloud_bl                           = 1,
 num_soil_layers                     = 4,
 cu_rad_feedback                     = .true., .false.,.false.,.false.
 cu_diag                             = 1, 0, 0, 0,
 slope_rad                           = 1, 1, 1, 1,
 topo_shading                        = 0, 0, 0, 0,
 num_land_cat                        = 21,
 /

 &fdda
 grid_fdda                           = 1, 0, 0, 0,
 gfdda_inname                        = "wrffdda_d<domain>",
 gfdda_end_h                         = 312, 0, 0, 0,
 gfdda_interval_m                    = 60, 0, 0, 0,
 if_no_pbl_nudging_uv                = 1, 1, 1, 1,
 if_no_pbl_nudging_t                 = 1, 1, 1, 1,
 if_no_pbl_nudging_q                 = 1, 1, 1, 1,
 if_zfac_uv                          = 0, 0, 0, 0,
 k_zfac_uv                           = 2,
 if_zfac_t                           = 0, 0, 0, 0,
 k_zfac_t                            = 2,
 if_zfac_q                           = 0, 0, 0, 0,
 k_zfac_q                            = 2,
 guv                                 = 0.0006, 0.0006, 0.0006, 0.0006,
 gt                                  = 0.0006, 0.0006, 0.0006, 0.0006,
 gq                                  = 0.0006, 0.0006, 0.0006, 0.0006,
 if_ramping                          = 0,
 dtramp_min                          = 360,
```

```
io_form_gfdda                       = 2,
/

&dynamics
rk_ord                              = 3,
time_step_sound                     = 4, 4, 4, 4,
w_damping                           = 1,
diff_opt                            = 1, 2, 2, 2,
km_opt                              = 4, 4, 4, 4,
diff_6th_opt                        = 0, 0, 0, 0,
diff_6th_factor                     = 0.12, 0.12, 0.75, 0.5,
epssm                               = 0.1, 0.1, 0.5, 0.5,
sfs_opt                             = 0, 0, 0, 0,
base_temp                           = 290.
damp_opt                            = 3,
zdamp                               = 5000., 5000., 5000., 5000.,
dampcoef                            = 0.15, 0.15, 0.15, 0.15,
khdif                               = 0, 0, 0, 0,
kvdif                               = 0, 0, 0, 0,
mix_isotropic                       = 0, 0, 1, 1,
non_hydrostatic                     = .true.,
moist_adv_opt                       = 2, 2, 4, 4,
scalar_adv_opt                      = 2, 2, 4, 4,
tke_adv_opt                         = 2, 2, 4, 4,
do_avgflx_em                        = 1, 1, 1, 1,
hybrid_opt                          = 0,
use_theta_m                         = 1,
/

&bdy_control
spec_bdy_width                      = 5,
spec_zone                           = 1,
relax_zone                          = 4,
specified                           = .true., .false., .false., .false.,
nested                              = .false., .true., .true., .true.,
/

&grib2
/

&namelist_quilt
nio_tasks_per_group                 = 0,
nio_groups                          = 0
/
```

Abbreviations

CAPE	Convective Available Potential Energy.
CCN	Cloud Condensation Nuclei.
CFAD	Contoured frequency by altitude diagram (Yuter and Houze, 1995).
CFL	Courant–Friedricks–Lewy.
CIN	Convective Inhibition.
CR-SIM	Cloud-resolving model Radar SIMulator (Oue et al., 2020).
CW	Continuous-wave radar.
DFG	German Research Foundation (Deutsche Forschungsgemeinschaft).
DLR	German Aerospace Center.
DWD	German Meteorological Service (Deutscher Wetterdienst).
FSBM	Fast Spectral Bin Model (Shpund et al., 2019).
GFS	Global Forecast System (National Centers For Environmental Prediction/National Weather Service/NOAA/U.S. Department Of Commerce, 2015).
HID	Hydrometeor Identification.
IcePolCKa	Investigation of the initiation of convection and the evolution of precipitation using simulations and polarimetric radar observations at C- and Ka-band.
IN	Ice Nuclei.
IPCC	Intergovernmental Panel on Climate Change.
LAM	Limited Area Model.
LCM	Lagrangian cloud model.
LMU	Ludwig-Maximilians-Universität.
LT	Local Time (Central European Time).
MIM	Meteorological Institute Munich.
MYNN2	Mellor–Yamada scheme by Nakanishi and Niino (Nakanishi and Niino, 2006).

NWP Numerical Weather Prediction.

P3 Predicted Particle Properties (Morrison and Milbrandt, 2015).
PPI Plan Position Indicator.
PROM Polarimetric Radar Observations meet Atmospheric Modelling – Fusion of Radar Polarimetry and Numerical Atmospheric Modelling Towards an Improved Understanding of Cloud and Precipitation Processes (Trömel et al., 2021).
PSD Particle Size Distribution.

QPE Quantitative Precipitation Estimation.

RHI Range Height Indicator.
RRTMG Rapid Radiative Transfer Model for General Circulation Models (Iacono et al., 2008).

S-RHI Sector Range Height Indicator.

TINT TINT is not TITAN (Raut et al., 2021).
TITAN Thunderstorm Identification, Tracking, Analysis, and Nowcasting (Dixon and Wiener, 1993).

UTC Coordinated Universal Time.

WRF Weather Research and Forecasting (Skamarock et al., 2019).

Symbols

Symbol	Description	Unit
A_{DP}	Specific differential attenuation	$\mathrm{dB\,km^{-1}}$
A_{e}	Effective antenna area	$\mathrm{m^2}$
A_{s}	Specific attenuation	$\mathrm{dB\,km^{-1}}$
$A_{\mathrm{s,i}}$	Specific attenuation at range gate i	$\mathrm{dB\,km^{-1}}$
B	Bouyancy	$\mathrm{m\,s^{-2}}$
C	Some constant	
D_{A}	Antenna diameter	m
D	Diameter	m
F_{r}	Rime mass fraction	1
G	Antenna gain	1
K_{DP}	Specific differential phase shift	$\mathrm{deg\,m^{-1}}$
L_{DR}	Linear depolarization ratio	dB
N_0	Intercept parameter of the PSD	Varying. $\mathrm{m^{-4}}$ for μ=0
N	Number concentration	$\mathrm{m^{-4}}$
P_σ	Power scattered back towards radar	W
P_{r}	Power received at the radar	W
P_{t}	Transmitted beam power	W
P	Power	W
R_{rate}	Rain rate	$\mathrm{mm\,h^{-1}}$
R_{un}	Maximum unambiguous range	m
R	Specific gas constant of dry air ($R = 287\,\mathrm{J\,kg^{-1}\,K^{-1}}$)	$\mathrm{J\,kg^{-1}\,K^{-1}}$
S	Beam power density	$\mathrm{W\,m^2}$
T'	Environmental temperature	K

Symbol	Description	Unit
$T_{\mathrm{v,0}}$	Virtual temperature of the environment	K
$T_{\mathrm{v,p}}$	Virtual temperature of an air parcel	K
T	Temperature	K
Vol	Unit volume	m^3
V	Radar beam volume	m^3
Z_{DR}	Differential reflectivity	dB
$Z_{\mathrm{e},\lambda 1}$	Equivalent reflectivity factor of radar with wavelength λ_1	dBZ
$Z_{\mathrm{e},\lambda 2}$	Equivalent reflectivity factor of radar with wavelength λ_2	dBZ
Z_{e}	Equivalent reflectivity factor on a logarithmic scale. Referred to as *reflectivity* in this work.	dBZ
Z_{hh}	Equivalent reflectivity transmitted and received at horizontal polarization	dBZ
Z_{hv}	Equivalent reflectivity transmitted at horizontal and received at vertical polarization	dBZ
Z_{vv}	Equivalent reflectivity transmitted and received at vertical polarization	dBZ
$Z_{\mathrm{corr,r}}$	Attenuation corrected equivalent reflectivity	dBZ
$Z_{\mathrm{e,r}}$	Equivalent reflectivity at range gate r	dBZ
$\Delta\phi_{\mathrm{dp}}$	Differential phase shift between vertically and horizontally polarized wave	deg
Δr	Radar range resolution	m
Λ	Slope parameter of the PSD	1
Ω	Angular speed of Earth's rotation ($7.292 \times 10^{-5}\,\mathrm{s}^{-1}$)	s^{-1}
α	Some proportionality factor	1
$\dot{Q}_{\mathrm{v}}$	Humidity sinks or sources	$\mathrm{kg\,kg}^{-1}\,\mathrm{s}^{-1}$
$\dot{Q}$	Heating rate	$\mathrm{J\,K}^{-1}\,\mathrm{s}^{-1}$
ϵ_{r}	Relative permativity	1
η	Reflectivity	m^{-1}
γ	Size parameter	1
λ	Wavelength	m
μ	Shape parameter of the PSD	1
ν	Kinematic viscosity coefficient	$\mathrm{m}^2\,\mathrm{s}^{-1}$
ω	Beamwidth	rad
ϕ	Latitude	deg

Symbol	Description	Unit
ρ_b	Hydrometeor bulk density	$\mathrm{kg\,m^{-3}}$
ρ_hv	Co-polar correlation coefficient	1
ρ_r	Rime density	$\mathrm{kg\,m^{-3}}$
ρ	Density	$\mathrm{kg\,m^{-3}}$
σ_t	Total radar cross section of all targets in beam volume	$\mathrm{m^2}$
σ	Radar cross section	$\mathrm{m^2}$
τ	Pulse length	s
θ	Beam elevation	rad
υ	Some function	
$\vec{\Omega}$	Rotation vector of Earth	$\mathrm{s^{-1}}$
$\vec{f}$	External (mass-specific) forces	$\mathrm{m\,s^{-2}}$
$\vec{g}$	Effective gravity	$\mathrm{m\,s^{-2}}$
$\vec{v}$	Wind velocity	$\mathrm{m\,s^{-1}}$
a_e	Effective Earth radius for a refracted beam	m
a_o	Earth radius (a_o=6 371 000 m)	m
ar	Aspect ratio	1
a	Parameter of mass–size relation ($m = aD^b$)	$\mathrm{kg\,m^{-b}}$
b	Parameter of mass–size relation ($m = aD^b$)	1
c_m	Speed of electromagnetic radiation through a medium	$\mathrm{m\,s^{-1}}$
c_p	Specific heat capacity at constant pressure	$\mathrm{J\,K^{-1}\,kg^{-1}}$
c	Speed of light in vacuum ($3 \times 10^8\,\mathrm{m\,s^{-1}}$)	$\mathrm{m\,s^{-1}}$
dwr	Dual-wavelength ratio	dB
f_pr	Pulse repitition frequency	$\mathrm{s^{-1}}$
f	Frequency	$\mathrm{s^{-1}}$
g	Scalar effective gravity ($9.81\,\mathrm{m\,s^{-2}}$)	$\mathrm{m\,s^{-2}}$
h	Beam height above surface	m
i	Some integer	1
k_e	Effective Earth radius factor ($a_\mathrm{e} = k_\mathrm{e}a_\mathrm{o}$)	1
l_a	Power loss factor due to attenuation	1
l_b	Power loss factor due to losses other than attenuation	1
l	Beam cone length	m
m	Mass	kg
n	Refractive index	1

Symbol	Description	Unit
p_{EL}	Pressure at the equilibrium level	Pa
p_{LFC}	Pressure at the level of free convection	Pa
p	Pressure	Pa
q	Water vapor mixing ratio	$\mathrm{kg\,kg^{-1}}$
r	Beam range gate	m
t	Time	s
u	Wind speed in x-direction	$\mathrm{m\,s^{-1}}$
x	Cartesian x-coordinate	m
y	Cartesian y-coordinate	m
z_{e}	Equivalent reflectivity factor	$\mathrm{mm^6\,m^{-3}}$
z_{fac}	Reflectivity factor	$\mathrm{mm^6\,m^{-3}}$
z_{hh}	Equivalent reflectivity factor transmitted and received at horizontal polarization	$\mathrm{mm^6\,m^{-3}}$
z_{hv}	Equivalent reflectivity factor transmitted at horizontal and received at vertical polarization	$\mathrm{mm^6\,m^{-3}}$
z_{vv}	Equivalent reflectivity factor transmitted and received at vertical polarization	$\mathrm{mm^6\,m^{-3}}$
z	Cartesian z-coordinate	m
$\lvert K\rvert^2$	Dielectric constant	1

Bibliography

Arakawa, A.: A Personal Perspective on the Early Years of General Circulation Modeling at UCLA, in: General Circulation Model Development, chap. 1, pp. 1–66, Academic Press, 2000.

Arias, P. A., Bellouin, N., Coppola, E., Jones, R. G., Krinner, G., Marotzke, J., Naik, V., Palmer, M. D., Plattner, G.-K., Rogelj, J., Rojas, M., Sillmann, J., Storelvmo, T., Thorne, P. W., Trewin, B., Achuta Rao, K., Adhikary, B., Allan, R. P., Armour, K., Bala, G., Barimalala, R., Berger, S., Canadell, J. G., Cassou, C., Cherchi, A., Collins, W., Collins, W. D., Connors, S. L., Corti, S., Cruz, F., Dentener, F. J., Dereczynski, C., Di Luca, A., Diongue Niang, A., Doblas-Reyes, F. J., Dosio, A., Douville, H., Engelbrecht, F., Eyring, V., Fischer, E., Forster, P., Fox-Kemper, B., Fuglestvedt, J. S., Fyfe, J. C., Gillett, N. P., Goldfarb, L., Gorodetskaya, I., Gutierrez, J. M., Hamdi, R., Hawkins, E., Hewitt, H. T., Hope, P., Islam, A. S., Jones, C., Kaufman, D. S., Kopp, R. E., Kosaka, Y., Kossin, J., Krakovska, S., Lee, J.-Y., Li, J., Mauritsen, T., Maycock, T. K., Meinshausen, M., Min, S.-K., Monteiro, P. M. S., Ngo-Duc, T., Otto, F., Pinto, I., Pirani, A., Raghavan, K., Ranasinghe, R., Ruane, A. C., Ruiz, L., Sallée, J.-B., Samset, B. H., Sathyendranath, S., Seneviratne, S. I., Sörensson, A. A., Szopa, S., Takayabu, I., Tréguier, A.-M., van den Hurk, B., Vautard, R., von Schuckmann, K., Zaehle, S., Zhang, X., and Zickfeld, K.: Technical summary. In Climate Change 2021: The Physical Science Basis. Contribution of Working Group I to the Sixth Assessment Report of the Intergovernmental Panel on Climate Change. [Masson-Delmotte, V., P. Zhai, A. Pirani, S.L. Connors, C. Péan, S. Berger, N. Caud, Y. Chen, L. Goldfarb, M.I. Gomis, M. Huang, K. Leitzell, E. Lonnoy, J.B.R. Matthews, T.K. Maycock, T. Waterfield, O. Yelekçi, R. Yu, and B. Zhou (eds.)], Cambridge University Press, Cambridge, United Kingdom and New York, NY, USA, pp. 33–144, doi:10.1017/9781009157896.002, https://report.ipcc.ch/ar6/wg1/IPCC_AR6_WGI_FullReport.pdf, last access: 22 February 2023, 2021.

Augros, C., Caumont, O., Ducrocq, V., Gaussiat, N., and Tabary, P.: Comparisons between S-, C- and X-band polarimetric radar observations and convective-scale simulations of the HyMeX first special observing period, Quarterly Journal of the Royal Meteorological Society, 142, 347–362, doi:10.1002/qj.2572, 2015.

Austin, P. M. and Bemis, A. C.: A QUANTITATIVE STUDY OF THE "BRIGHT BAND" IN RADAR PRECIPITATION ECHOES, Journal of Atmospheric Sciences, 7, 145 – 151, doi:10.1175/1520-0469(1950)007<0145:AQSOTB>2.0.CO;2, 1950.

Bachmann, K., Keil, C., Craig, G. C., Weissmann, M., and Welzbacher, C. A.: Predictability of Deep Convection in Idealized and Operational Forecasts: Effects of Radar Data Assimilation, Orography, and Synoptic Weather Regime, Monthly Weather Review, 148, 63–81, doi:10.1175/mwr-d-19-0045.1, 2019.

Baldauf, M., Seifert, A., Förstner, J., Majewski, D., Raschendorfer, M., and Reinhardt, T.: Operational Convective-Scale Numerical Weather Prediction with the COSMO Model: Description and Sensitivities, Monthly Weather Review, 139, 3887–3905, doi:10.1175/mwr-d-10-05013.1, 2011.

Barber, P. and Yeh, C.: Scattering of electromagnetic waves by arbitrarily shaped dielectric bodies, Applied Optics, 14, 2864, doi:10.1364/ao.14.002864, 1975.

Barrett, A. I., Gray, S. L., Kirshbaum, D. J., Roberts, N. M., Schultz, D. M., and Fairman, J. G.: Synoptic versus orographic control on stationary convective banding, Quarterly Journal of the Royal Meteorological Society, 141, 1101–1113, doi:10.1002/qj.2409, 2014.

Battan, L. J.: Radar observation of the atmosphere, University of Chicago Press, 1973a.

Battan, L. J.: Radar Detection of Spherical Particles, in: Radar observation of the atmosphere, chap. 4, pp. 29–44, University of Chicago Press, 1973b.

Bauer-Pfundstein, M.: Manufacturer documentation of the MIRA-35 antenna: Antenna CA-35.15-1.0m-D/003, Tech. rep., Metek GmbH, 2012.

Besic, N., Figueras i Ventura, J., Grazioli, J., Gabella, M., Germann, U., and Berne, A.: Hydrometeor classification through statistical clustering of polarimetric radar measurements: a semi-supervised approach, Atmospheric Measurement Techniques, 9, 4425–4445, doi:10.5194/amt-9-4425-2016, 2016.

Besic, N., Gehring, J., Praz, C., Figueras i Ventura, J., Grazioli, J., Gabella, M., Germann, U., and Berne, A.: Unraveling hydrometeor mixtures in polarimetric radar measurements, Atmospheric Measurement Techniques, 11, 4847–4866, doi:10.5194/amt-11-4847-2018, 2018.

Bjerknes, V.: Das Problem der Wettervorhersage, betrachtet vom Standpunkte der Mechanik und der Physik, Meteor. Z., 21, 1–7, 1904.

Boot, H. A. H. and Randall, J. T.: The cavity magnetron, Journal of the Institution of Electrical Engineers - Part IIIA: Radiolocation, 93, 928–938, doi:10.1049/ji-3a-1.1946.0183, 1946.

Brandes, E. A., Zhang, G., and Vivekanandan, J.: Experiments in Rainfall Estimation with a Polarimetric Radar in a Subtropical Environment, Journal of Applied Meteorology, 41, 674 – 685, doi:10.1175/1520-0450(2002)041<0674:EIREWA>2.0.CO;2, 2002.

Bringi, V. N. and Chandrasekar, V.: Polarimetric Doppler Weather Radar, Cambridge University Press, doi:10.1017/cbo9780511541094, 2001a.

Bringi, V. N. and Chandrasekar, V.: Electromagnetic concepts useful for radar applications, in: Polarimetric Doppler Weather Radar, chap. 1, pp. 1–44, Cambridge University Press, doi:10.1017/cbo9780511541094, 2001b.

Brown, P. R. A. and Francis, P. N.: Improved Measurements of the Ice Water Content in Cirrus Using a Total-Water Probe, Journal of Atmospheric and Oceanic Technology, 12, 410 – 414, doi:10.1175/1520-0426(1995)012<0410:IMOTIW>2.0.CO;2, 1995.

Caine, S., Lane, T. P., May, P. T., Jakob, C., Siems, S. T., Manton, M. J., and Pinto, J.: Statistical Assessment of Tropical Convection-Permitting Model Simulations Using a Cell-Tracking Algorithm, Monthly Weather Review, 141, 557–581, doi:10.1175/mwr-d-11-00274.1, 2013.

Cao, Q., Zhang, G., Brandes, E., Schuur, T., Ryzhkov, A., and Ikeda, K.: Analysis of Video Disdrometer and Polarimetric Radar Data to Characterize Rain Microphysics in Oklahoma, Journal of Applied Meteorology and Climatology, 47, 2238–2255, doi:10.1175/2008jamc1732.1, 2008.

Cao, Q., Zhang, G., Brandes, E. A., and Schuur, T. J.: Polarimetric Radar Rain Estimation through Retrieval of Drop Size Distribution Using a Bayesian Approach, Journal of Applied Meteorology and Climatology, 49, 973–990, doi:10.1175/2009jamc2227.1, 2010.

Charney, J. G., FjÖrtoft, R., and Neumann, J. V.: Numerical Integration of the Barotropic Vorticity Equation, Tellus, 2, 237–254, doi:10.3402/tellusa.v2i4.8607, 1950.

Chen, F. and Dudhia, J.: Coupling an Advanced Land Surface–Hydrology Model with the Penn State–NCAR MM5 Modeling System. Part I: Model Implementation and Sensitivity, Monthly Weather Review, 129, 569 – 585, doi:10.1175/1520-0493(2001)129<0569:CAALSH>2.0.CO;2, 2001.

Cholette, M., Morrison, H., Milbrandt, J. A., and Thériault, J. M.: Parameterization of the Bulk Liquid Fraction on Mixed-Phase Particles in the Predicted Particle Properties (P3) Scheme: Description and Idealized Simulations, Journal of the Atmospheric Sciences, 76, 561–582, doi:10.1175/jas-d-18-0278.1, 2019.

Clark, P., Roberts, N., Lean, H., Ballard, S. P., and Charlton-Perez, C.: Convection-permitting models: a step-change in rainfall forecasting, Meteorological Applications, 23, 165–181, doi:10.1002/met.1538, 2016.

Coiffier, J.: Fundamentals of numerical weather prediction, Cambridge University Press, 2011a.

Coiffier, J.: Half a century of numerical weather prediction, in: Fundamentals of numerical weather prediction, chap. 1, pp. 1–14, Cambridge University Press, 2011b.

Coiffier, J.: Weather prediction equations, in: Fundamentals of numerical weather prediction, chap. 2, pp. 15–38, Cambridge University Press, 2011c.

Detlefsen, J., Svensson, S. P., and Lugli, P.: Radartechnik Grundlagen, Bauelemente, Verfahren, Anwendungen, Springer, 1989a.

Detlefsen, J., Svensson, S. P., and Lugli, P.: Grundlagen der Radartechnik, in: Radartechnik, chap. 2, pp. 10–55, Springer, 1989b.

Deutscher Wetterdienst: URL https://www.dwd.de/DE/service/lexikon/begriffe/S/Starkregen.html, last access: 5 September 2022, 2022.

Deutscher Wetterdienst: URL https://www.dwd.de/DE/service/lexikon/Functions/glossar.html?lv2=100510&lv3=100534, last access: 13 February 2023, 2023a.

Deutscher Wetterdienst: URL https://www.dwd.de/SharedDocs/broschueren/EN/press/dmrz_en.pdf?__blob=publicationFile&v=2, last access: 28 March 2023, 2023b.

Deutscher Wetterdienst: URL https://opendata.dwd.de/climate_environment/CDC/observations_germany/climate/10_minutes/wind/, last access: 19 January 2023, 2023c.

Dixon, M. and Wiener, G.: TITAN: Thunderstorm Identification, Tracking, Analysis, and Nowcasting—A Radar-based Methodology, Journal of Atmospheric and Oceanic Technology, 10, 785 – 797, doi:10.1175/1520-0426(1993)010<0785:TTITAA>2.0.CO;2, 1993.

Dolan, B. and Rutledge, S. A.: A Theory-Based Hydrometeor Identification Algorithm for X-Band Polarimetric Radars, Journal of Atmospheric and Oceanic Technology, 26, 2071–2088, doi:10.1175/2009jtecha1208.1, 2009.

Dolan, B., Rutledge, S. A., Lim, S., Chandrasekar, V., and Thurai, M.: A Robust C-Band Hydrometeor Identification Algorithm and Application to a Long-Term Polarimetric Radar Dataset, Journal of Applied Meteorology and Climatology, 52, 2162–2186, doi:10.1175/jamc-d-12-0275.1, 2013.

Doswell III, C. A.: Severe Convective Storms – An Overview, in: Severe Convective Storms, chap. 1, pp. 1 – 26, American Meteorological Society, 2001.

Doviak, R. J.: Doppler radar and weather observations, Academic Press, 1984a.

Doviak, R. J.: Electromagnetic Waves and Propagation, in: Doppler radar and weather observations, chap. 2, pp. 4–20, Academic Press, 1984b.

Doviak, R. J.: Principles of Radar, in: Doppler radar and weather observations, chap. 3, pp. 21–49, Academic Press, 1984c.

Durran, D. R.: Numerical Methods for Fluid Dynamics, Springer New York, doi:10.1007/978-1-4419-6412-0, 2010a.

Durran, D. R.: Introduction, in: Numerical Methods for Fluid Dynamics, chap. 1, pp. 1–34, Springer New York, doi:10.1007/978-1-4419-6412-0, 2010b.

Durran, D. R.: Ordinary Differential Equations, in: Numerical Methods for Fluid Dynamics, chap. 2, pp. 35–87, Springer New York, doi:10.1007/978-1-4419-6412-0, 2010c.

Ek, M. B., Mitchell, K. E., Lin, Y., Rogers, E., Grunmann, P., Koren, V., Gayno, G., and Tarpley, J. D.: Implementation of Noah land surface model advances in the National Centers for Environmental Prediction operational mesoscale Eta model, Journal of Geophysical Research: Atmospheres, 108, doi:10.1029/2002jd003296, 2003.

Ewald, F., Groß, S., Hagen, M., Hirsch, L., Delanoë, J., and Bauer-Pfundstein, M.: Calibration of a 35 GHz airborne cloud radar: lessons learned and intercomparisons with 94 GHz cloud radars, Atmospheric Measurement Techniques, 12, 1815–1839, doi:10.5194/amt-12-1815-2019, 2019.

Fabry, F.: Radar Meteorology Principles and Practice, Cambridge University Press, 2017a.

Fabry, F.: Fundamentals of weather radar measurements, in: Radar Meteorology Principles and Practice, chap. 2, pp. 8–31, Cambridge University Press, 2017b.

Fabry, F.: What does radar really measure?, in: Radar Meteorology Principles and Practice, chap. 13, pp. 201–214, Cambridge University Press, 2017c.

Fan, J., Liu, Y.-C., Xu, K.-M., North, K., Collis, S., Dong, X., Zhang, G. J., Chen, Q., Kollias, P., and Ghan, S. J.: Improving representation of convective transport for scale-aware parameterization: 1. Convection and cloud properties simulated with spectral bin and bulk microphysics, Journal of Geophysical Research: Atmospheres, 120, 3485–3509, doi:10.1002/2014jd022142, 2015.

Fan, J., Han, B., Varble, A., Morrison, H., North, K., Kollias, P., Chen, B., Dong, X., Giangrande, S. E., Khain, A., Lin, Y., Mansell, E., Milbrandt, J. A., Stenz, R., Thompson, G., and Wang, Y.: Cloud-resolving model intercomparison of an MC3E squall line case: Part I—Convective updrafts, Journal of Geophysical Research: Atmospheres, 122, 9351–9378, doi:10.1002/2017jd026622, 2017.

Field, P. R., Hogan, R. J., Brown, P. R. A., Illingworth, A. J., Choularton, T. W., and Cotton, R. J.: Parametrization of ice-particle size distributions for mid-latitude stratiform cloud, Quarterly Journal of the Royal Meteorological Society, 131, 1997–2017, doi:10.1256/qj.04.134, 2005.

Fridlind, A. M., van Lier-Walqui, M., Collis, S., Giangrande, S. E., Jackson, R. C., Li, X., Matsui, T., Orville, R., Picel, M. H., Rosenfeld, D., Ryzhkov, A., Weitz, R., and Zhang, P.: Use of polarimetric radar measurements to constrain simulated convective cell evolution: a pilot study with Lagrangian tracking, Atmospheric Measurement Techniques, 12, 2979–3000, doi:10.5194/amt-12-2979-2019, 2019.

Grazioli, J., Tuia, D., and Berne, A.: Hydrometeor classification from polarimetric radar measurements: a clustering approach, Atmospheric Measurement Techniques, 8, 149–170, doi:10.5194/amt-8-149-2015, 2015.

Görsdorf, U., Lehmann, V., Bauer-Pfundstein, M., Peters, G., Vavriv, D., Vinogradov, V., and Volkov, V.: A 35-GHz Polarimetric Doppler Radar for Long-Term Observations of Cloud Parameters—Description of System and Data Processing, Journal of Atmospheric and Oceanic Technology, 32, 675–690, doi:10.1175/jtech-d-14-00066.1, 2015.

Han, B., Fan, J., Varble, A., Morrison, H., Williams, C. R., Chen, B., Dong, X., Giangrande, S. E., Khain, A., Mansell, E., Milbrandt, J. A., Shpund, J., and Thompson, G.: Cloud-Resolving Model Intercomparison of an MC3E Squall Line Case: Part II. Stratiform Precipitation Properties, Journal of Geophysical Research: Atmospheres, 124, 1090–1117, doi:10.1029/2018jd029596, 2019.

Hanley, K. E., Kirshbaum, D. J., Belcher, S. E., Roberts, N. M., and Leoncini, G.: Ensemble predictability of an isolated mountain thunderstorm in a high-resolution model, Quarterly Journal of the Royal Meteorological Society, 137, 2124–2137, doi:10.1002/qj.877, 2011.

Hanley, K. E., Kirshbaum, D. J., Roberts, N. M., and Leoncini, G.: Sensitivities of a Squall Line over Central Europe in a Convective-Scale Ensemble, Monthly Weather Review, 141, 112–133, doi:10.1175/mwr-d-12-00013.1, 2013.

Helmert, K., Tracksdorf, P., Steinert, J., Werner, M., Frech, M., Rathmann, N., Hengstebeck, T., Mott, M., Schumann, S., and Mammen, T.: DWDs new radar network and post-processing algorithm chain, in: Proc. Eighth European Conf. on Radar in Meteorology and Hydrology (ERAD 2014), Garmisch-Partenkirchen, Germany, URL `https://www.pa.op.dlr.de/erad2014/programme/ExtendedAbstracts/237_Helmert.pdf`, last access: 16 February 2022, 2014.

Helmus, J. J. and Collis, S. M.: The Python ARM Radar Toolkit (Py-ART), a Library for Working with Weather Radar Data in the Python Programming Language, Journal of Open Research Software, 4, 25, doi:10.5334/jors.119, 2016.

Heymsfield, A. J.: Properties of Tropical and Midlatitude Ice Cloud Particle Ensembles. Part II: Applications for Mesoscale and Climate Models, Journal of the Atmospheric Sciences, 60, 2592 – 2611, doi:10.1175/1520-0469(2003)060<2592:POTAMI>2.0.CO;2, 2003.

Hogan, R. J., Tian, L., Brown, P. R. A., Westbrook, C. D., Heymsfield, A. J., and Eastment, J. D.: Radar Scattering from Ice Aggregates Using the Horizontally Aligned Oblate Spheroid Approximation, Journal of Applied Meteorology and Climatology, 51, 655–671, doi:10.1175/jamc-d-11-074.1, 2012.

Holton, J. R. and Hakim, G. J.: Basic Conservation Laws, in: An introduction to dynamic meteorology, chap. 2, pp. 31–66, Academic Press, 5th edn., 2012a.

Holton, J. R. and Hakim, G. J.: Numerical Modeling and Prediction, in: An introduction to dynamic meteorology, chap. 2, pp. 453–490, Academic Press, 5th edn., 2012b.

Houze, R. A.: Cloud Dynamics, vol. 53 of *International Geophysics*, Academic Press, 1994.

Iacono, M. J., Delamere, J. S., Mlawer, E. J., Shephard, M. W., Clough, S. A., and Collins, W. D.: Radiative forcing by long-lived greenhouse gases: Calculations with the AER radiative transfer models, Journal of Geophysical Research, 113, doi:10.1029/2008jd009944, 2008.

Inness, P. and Dorling, S.: Operational Weather Forecasting, John Wiley and Sons Ltd, 2013a.

Inness, P. and Dorling, S.: Introduction, in: Operational Weather Forecasting, chap. 1, pp. 1–8, John Wiley and Sons Ltd, 2013b.

Inness, P. and Dorling, S.: The Nature of the Weather Forecasting Problem, in: Operational Weather Forecasting, chap. 2, pp. 9–26, John Wiley and Sons Ltd, 2013c.

Inness, P. and Dorling, S.: NWP Models - the Basic Principles, in: Operational Weather Forecasting, chap. 4, pp. 54–108, John Wiley and Sons Ltd, 2013d.

Jeevanjee, N.: Vertical Velocity in the Gray Zone, Journal of Advances in Modeling Earth Systems, 9, 2304–2316, doi:10.1002/2017ms001059, 2017.

Jung, S.-H. and Lee, G.: Radar-based cell tracking with fuzzy logic approach, Meteorological Applications, 22, 716–730, doi:10.1002/met.1509, 2015.

Kamra, A. K., Bhalwankar, R. V., and Sathe, A. B.: Spontaneous breakup of charged and uncharged water drops freely suspended in a wind tunnel, Journal of Geophysical Research, 96, 17 159, doi:10.1029/91jd01475, 1991.

Kessler, E.: On the Distribution and Continuity of Water Substance in Atmospheric Circulations, in: On the Distribution and Continuity of Water Substance in Atmospheric Circulations, pp. 1–84, American Meteorological Society, doi:10.1007/978-1-935704-36-2_1, 1969.

Khain, A. P., Beheng, K. D., Heymsfield, A., Korolev, A., Krichak, S. O., Levin, Z., Pinsky, M., Phillips, V., Prabhakaran, T., Teller, A., van den Heever, S. C., and Yano, J.-I.: Representation of microphysical processes in cloud-resolving models: Spectral (bin) microphysics versus bulk parameterization, Reviews of Geophysics, 53, 247–322, doi:10.1002/2014rg000468, 2015.

Kumjian, M. R.: Weather Radars, in: Remote Sensing of Clouds and Precipitation, chap. 2, pp. 15–63, Springer International Publishing, doi:10.1007/978-3-319-72583-3_2, 2018.

Köcher, G., Zinner, T., and Knote, C.: Influence of cloud microphysics schemes on weather model predictions of heavy precipitation, Atmospheric Chemistry and Physics Discussion [preprint], doi:10.5194/acp-2022-835, 2022a.

Köcher, G., Zinner, T., Knote, C., Tetoni, E., Ewald, F., and Hagen, M.: Evaluation of convective cloud microphysics in numerical weather prediction models with dual-wavelength polarimetric radar observations: methods and examples, Atmospheric Measurement Techniques, 15, 1033–1054, doi:10.5194/amt-15-1033-2022, 2022b.

Kühnlein, C., Keil, C., Craig, G. C., and Gebhardt, C.: The impact of downscaled initial condition perturbations on convective-scale ensemble forecasts of precipitation, Quarterly Journal of the Royal Meteorological Society, 140, 1552–1562, doi:10.1002/qj.2238, 2014.

Lang, T., Dolan, B., Guy, N., CAM Gerlach, and Hardin, J.: CSU-Radarmet/CSU_RadarTools: CSU_RadarTools v1.3, doi:10.5281/ZENODO.2562063, 2019.

Lean, H. W., Clark, P. A., Dixon, M., Roberts, N. M., Fitch, A., Forbes, R., and Halliwell, C.: Characteristics of High-Resolution Versions of the Met Office Unified Model for Forecasting Convection over the United Kingdom, Monthly Weather Review, 136, 3408–3424, doi:10.1175/2008mwr2332.1, 2008.

Lebo, Z. J. and Morrison, H.: Effects of Horizontal and Vertical Grid Spacing on Mixing in Simulated Squall Lines and Implications for Convective Strength and Structure, Monthly Weather Review, 143, 4355–4375, doi:10.1175/mwr-d-15-0154.1, 2015.

Li, X., Tao, W.-K., Khain, A. P., Simpson, J., and Johnson, D. E.: Sensitivity of a Cloud-Resolving Model to Bulk and Explicit Bin Microphysical Schemes. Part I: Comparisons, Journal of the Atmospheric Sciences, 66, 3–21, doi:10.1175/2008jas2646.1, 2009.

Liang, X.-Z., Li, Q., Mei, H., and Zeng, M.: Multi-Grid Nesting Ability to Represent Convections Across the Gray Zone, Journal of Advances in Modeling Earth Systems, 11, 4352–4376, doi:10.1029/2019ms001741, 2019.

Lorenz, E. N.: The predictability of a flow which possesses many scales of motion, Tellus A: Dynamic Meteorology and Oceanography, 21, 289, doi:10.3402/tellusa.v21i3.10086, 1969.

Lunkeit, F.: Meteorologische Modellierung, lecture script, 2015.

Martin, G. M., Johnson, D. W., and Spice, A.: The Measurement and Parameterization of Effective Radius of Droplets in Warm Stratocumulus Clouds, Journal of Atmospheric Sciences, 51, 1823 – 1842, doi:10.1175/1520-0469(1994)051<1823:TMAPOE>2.0.CO;2, 1994.

Matsui, T., Zeng, X., Tao, W.-K., Masunaga, H., Olson, W. S., and Lang, S.: Evaluation of Long-Term Cloud-Resolving Model Simulations Using Satellite Radiance Observations and Multifrequency Satellite Simulators, Journal of Atmospheric and Oceanic Technology, 26, 1261–1274, doi:10.1175/2008jtecha1168.1, 2009.

Maxwell Garnett, J. C.: XII. Colours in metal glasses and in metallic films, Philosophical Transactions of the Royal Society of London. Series A, Containing Papers of a Mathematical or Physical Character, 203, 385–420, doi:10.1098/rsta.1904.0024, 1904.

McMurdie, L. and Houze, R. A.: Weather Systems, in: Atmospheric Science, chap. 8, pp. 313–374, Academic Press, 2nd edn., 2005.

Mie, G.: Beiträge zur Optik trüber Medien, speziell kolloidaler Metallösungen, Annalen der Physik, 330, 377–445, doi:10.1002/andp.19083300302, 1908.

Milbrandt, J. A. and Yau, M. K.: A Multimoment Bulk Microphysics Parameterization. Part II: A Proposed Three-Moment Closure and Scheme Description, Journal of the Atmospheric Sciences, 62, 3065–3081, doi:10.1175/jas3535.1, 2005.

Morrison, H. and Milbrandt, J. A.: Parameterization of Cloud Microphysics Based on the Prediction of Bulk Ice Particle Properties. Part I: Scheme Description and Idealized Tests, Journal of the Atmospheric Sciences, 72, 287–311, doi:10.1175/jas-d-14-0065.1, 2015.

Morrison, H., Thompson, G., and Tatarskii, V.: Impact of Cloud Microphysics on the Development of Trailing Stratiform Precipitation in a Simulated Squall Line: Comparison of One- and Two-Moment Schemes, Monthly Weather Review, 137, 991–1007, doi:10.1175/2008mwr2556.1, 2009.

Morrison, H., van Lier-Walqui, M., Fridlind, A. M., Grabowski, W. W., Harrington, J. Y., Hoose, C., Korolev, A., Kumjian, M. R., Milbrandt, J. A., Pawlowska, H., Posselt, D. J., Prat, O. P., Reimel, K. J., Shima, S.-I., van Diedenhoven, B., and Xue, L.: Confronting the Challenge of Modeling Cloud and Precipitation Microphysics, Journal of Advances in Modeling Earth Systems, 12, doi:10.1029/2019ms001689, 2020.

Nakamura, K.: Biases of Rain Retrieval Algorithms for Spaceborne Radar Caused by Nonuniformity of Rain, Journal of Atmospheric and Oceanic Technology, 8, 363 – 373, doi:10.1175/1520-0426(1991)008<0363:BORRAF>2.0.CO;2, 1991.

Nakanishi, M. and Niino, H.: An Improved Mellor–Yamada Level-3 Model: Its Numerical Stability and Application to a Regional Prediction of Advection Fog, Boundary-Layer Meteorology, 119, 397–407, doi:10.1007/s10546-005-9030-8, 2006.

Nathanson, F. E.: Radar Design Principles, McGraw-Hill, 1969.

National Centers For Environmental Prediction/National Weather Service/NOAA/U.S. Department Of Commerce: NCEP GFS 0.25 Degree Global Forecast Grids Historical Archive, doi:10.5065/D65D8PWK, 2015.

Natural Earth: `https://www.naturalearthdata.com`, last access: April 13, 2023., 2023.

OpenStreetMap: `https://www.openstreetmap.org`, last access: April 13, 2023, under the Open Data Commons Open Database License (ODbL) v1.0., 2023.

Oue, M., Tatarevic, A., Kollias, P., Wang, D., Yu, K., and Vogelmann, A. M.: The Cloud-resolving model Radar SIMulator (CR-SIM) Version 3.3: description and applications of a virtual observatory, Geoscientific Model Development, 13, doi:10.5194/gmd-13-1975-2020, (code available at: https://you.stonybrook.edu/radar/research/radar-simulators/, last access: 21 September 2021), 2020.

Park, H. S., Ryzhkov, A. V., Zrnić, D. S., and Kim, K.-E.: The Hydrometeor Classification Algorithm for the Polarimetric WSR-88D: Description and Application to an MCS, Weather and Forecasting, 24, 730–748, doi:10.1175/2008waf2222205.1, 2009.

Pinto, J. O., Grim, J. A., and Steiner, M.: Assessment of the High-Resolution Rapid Refresh Model's Ability to Predict Mesoscale Convective Systems Using Object-Based Evaluation, Weather and Forecasting, 30, 892–913, doi:10.1175/waf-d-14-00118.1, 2015.

Probert-Jones, J. R.: The radar equation in meteorology, Quarterly Journal of the Royal Meteorological Society, 88, 485–495, doi:10.1002/qj.49708837810, 1962.

Putnam, B. J., Xue, M., Jung, Y., Zhang, G., and Kong, F.: Simulation of Polarimetric Radar Variables from 2013 CAPS Spring Experiment Storm-Scale Ensemble Forecasts and Evaluation of Microphysics Schemes, Monthly Weather Review, 145, 49–73, doi:10.1175/mwr-d-15-0415.1, 2016.

Raghavan, S.: Radar Meteorology - History, Principles and Technology, in: Radar Meteorology, chap. 1, pp. 1–50, Springer, 2003.

Raut, B. A., Jackson, R., Picel, M., Collis, S. M., Bergemann, M., and Jakob, C.: An Adaptive Tracking Algorithm for Convection in Simulated and Remote Sensing Data, Journal of Applied Meteorology and Climatology, 60, 513–526, doi:10.1175/jamc-d-20-0119.1, 2021.

Rayleigh, L.: On the transmission of light through an atmosphere containing small particles in suspension, and on the origin of the blue of the sky, The London, Edinburgh, and Dublin Philosophical Magazine and Journal of Science, 47, 375–384, doi:10.1080/14786449908621276, 1899.

Reimann, J.: On fast, polarimetric non-reciprocal calibration and multipolarization measurements on weather radars, Ph.D. thesis, Technische Universität Chemnitz, URL `http://nbn-resolving.de/urn:nbn:de:bsz:ch1-qucosa-132088`, (last access: 16 February 2022), 2013.

Richardson, L. F.: Weather prediction by numerical process, Cambridge University Press, 1922.

Rinehart, R. E.: Radar for Meteorologists, Rinehart Pub, third edn., 1997a.

Rinehart, R. E.: Introduction, in: Radar for Meteorologists, chap. 1, pp. 1–14, Rinehart Pub, third edn., 1997b.

Rinehart, R. E.: Electromagnetic Waves, in: Radar for Meteorologists, chap. 3, pp. 47–64, Rinehart Pub, third edn., 1997c.

Rinehart, R. E.: Radar Equation for Point Targets, in: Radar for Meteorologists, chap. 4, pp. 65–80, Rinehart Pub, third edn., 1997d.

Rinehart, R. E.: Distributed Targets, in: Radar for Meteorologists, chap. 5, pp. 81–96, Rinehart Pub, third edn., 1997e.

Rinehart, R. E.: Advanced Uses of Meteorological Radar, in: Radar for Meteorologists, chap. 10, pp. 197–216, Rinehart Pub, third edn., 1997f.

Rogers, R. R. and Yau, M. K.: A short course in cloud physics, Butterworth Heinemann, 1989a.

Rogers, R. R. and Yau, M. K.: Weather Radar, in: A short course in cloud physics, chap. 11, pp. 184–195, Butterworth Heinemann, 1989b.

Ryzhkov, A., Pinsky, M., Pokrovsky, A., and Khain, A.: Polarimetric Radar Observation Operator for a Cloud Model with Spectral Microphysics, Journal of Applied Meteorology and Climatology, 50, 873–894, doi:10.1175/2010jamc2363.1, 2011.

Ryzhkov, A., Zhang, P., Bukovčić, P., Zhang, J., and Cocks, S.: Polarimetric Radar Quantitative Precipitation Estimation, Remote Sensing, 14, 1695, doi:10.3390/rs14071695, 2022.

Ryzhkov, A. V., Snyder, J., Carlin, J. T., Khain, A., and Pinsky, M.: What Polarimetric Weather Radars Offer to Cloud Modelers: Forward Radar Operators and Microphysical/Thermodynamic Retrievals, Atmosphere, 11, 362, doi:10.3390/atmos11040362, 2020.

Schroth, A. C., Chandra, M. S., and Mesichner, P. F.: A C-Band Coherent Polarimetric Radar for Propagation and Cloud Physics Research, Journal of Atmospheric and Oceanic Technology, 5, 803 – 822, doi:10.1175/1520-0426(1988)005<0803:ABCPRF>2.0.CO;2, 1988.

Seity, Y., Brousseau, P., Malardel, S., Hello, G., Bénard, P., Bouttier, F., Lac, C., and Masson, V.: The AROME-France Convective-Scale Operational Model, Monthly Weather Review, 139, 976–991, doi:10.1175/2010mwr3425.1, 2011.

Shima, S., Kusano, K., Kawano, A., Sugiyama, T., and Kawahara, S.: The super-droplet method for the numerical simulation of clouds and precipitation: a particle-based and probabilistic microphysics model coupled with a non-hydrostatic model, Quarterly Journal of the Royal Meteorological Society, 135, 1307–1320, doi:10.1002/qj.441, 2009.

Shpund, J., Khain, A., Lynn, B., Fan, J., Han, B., Ryzhkov, A., Snyder, J., Dudhia, J., and Gill, D.: Simulating a Mesoscale Convective System Using WRF With a New Spectral Bin Microphysics: 1: Hail vs Graupel, Journal of Geophysical Research: Atmospheres, 124, 14 072–14 101, doi:10.1029/2019jd030576, 2019.

Skamarock, W. C.: Evaluating Mesoscale NWP Models Using Kinetic Energy Spectra, Monthly Weather Review, 132, 3019–3032, doi:10.1175/mwr2830.1, 2004.

Skamarock, W. C., Klemp, J. B., Dudhia, J., Gill, D. O., Liu, Z., Berner, J., Wang, W., Powers, J. G., Duda, M. G., Barker, D. M., and Huang, X.-Y.: A Description of the Advanced Research WRF Model Version 4, Tech. rep., doi:10.5065/1DFH-6P97, (code available on GitHub at: https://github.com/wrf-model/WRF, last access: 20 June 2020), 2019.

Skolnik, M. I.: Introduction to Radar Systems, MC GRAW HILL INDIA, third edn., 2001a.

Skolnik, M. I.: An Introduction to Radar, in: Introduction to Radar Systems, chap. 1, pp. 1–29, MC GRAW HILL INDIA, third edn., 2001b.

Skolnik, M. I.: The Radar Equation, in: Introduction to Radar Systems, chap. 2, pp. 30–103, MC GRAW HILL INDIA, third edn., 2001c.

Snyder, J. C., Bluestein, H. B., Daniel T. Dawson, I. I., and Jung, Y.: Simulations of Polarimetric, X-Band Radar Signatures in Supercells. Part I: Description of Experiment and Simulated ρ_{hv} Rings, Journal of Applied Meteorology and Climatology, 56, 1977–1999, doi:10.1175/jamc-d-16-0138.1, 2017.

Spiridonov, V., Baez, J., Telenta, B., and Jakimovski, B.: Prediction of extreme convective rainfall intensities using a free-running 3-D sub-km-scale cloud model initialized from WRF km-scale NWP forecasts, Journal of Atmospheric and Solar-Terrestrial Physics, 209, 105 401, doi:10.1016/j.jastp.2020.105401, 2020.

Srivastava, R. C.: Size Distribution of Raindrops Generated by their Breakup and Coalescence, Journal of Atmospheric Sciences, 28, 410 – 415, doi:10.1175/1520-0469(1971)028<0410:SDORGB>2.0.CO;2, 1971.

Stamen Design: `https://stamen.com`, last access: April 13, 2023, under the Creative Commons Attribution (CC BY 3.0) license., 2023.

Stanford, M. W., Varble, A., Zipser, E., Strapp, J. W., Leroy, D., Schwarzenboeck, A., Potts, R., and Protat, A.: A ubiquitous ice size bias in simulations of tropical deep convection, Atmospheric Chemistry and Physics, 17, 9599–9621, doi:10.5194/acp-17-9599-2017, 2017.

Stein, T. H. M., Hogan, R. J., Clark, P. A., Halliwell, C. E., Hanley, K. E., Lean, H. W., Nicol, J. C., and Plant, R. S.: The DYMECS Project: A Statistical Approach for the Evaluation of Convective Storms in High-Resolution NWP Models, Bulletin of the American Meteorological Society, 96, 939–951, doi:10.1175/bams-d-13-00279.1, 2015.

Tetoni, E., Ewald, F., Hagen, M., Köcher, G., Zinner, T., and Groß, S.: Retrievals of ice microphysical properties using dual-wavelength polarimetric radar observations during stratiform precipitation events, Atmospheric Measurement Techniques, 15, 3969–3999, doi:10.5194/amt-15-3969-2022, 2022.

Thompson, G. and Eidhammer, T.: A Study of Aerosol Impacts on Clouds and Precipitation Development in a Large Winter Cyclone, Journal of the Atmospheric Sciences, 71, 3636–3658, doi:10.1175/jas-d-13-0305.1, 2014.

Thompson, G., Field, P. R., Rasmussen, R. M., and Hall, W. D.: Explicit Forecasts of Winter Precipitation Using an Improved Bulk Microphysics Scheme. Part II: Implementation of a New Snow Parameterization, Monthly Weather Review, 136, 5095–5115, doi:10.1175/2008mwr2387.1, 2008.

Trömel, S., Simmer, C., Blahak, U., Blanke, A., Doktorowski, S., Ewald, F., Frech, M., Gergely, M., Hagen, M., Janjic, T., Kalesse-Los, H., Kneifel, S., Knote, C., Mendrok, J., Moser, M., Köcher, G., Mühlbauer, K., Myagkov, A., Pejcic, V., Seifert, P., Shrestha, P., Teisseire, A., von

Terzi, L., Tetoni, E., Vogl, T., Voigt, C., Zeng, Y., Zinner, T., and Quaas, J.: Overview: Fusion of radar polarimetry and numerical atmospheric modelling towards an improved understanding of cloud and precipitation processes, Atmospheric Chemistry and Physics, 21, 17 291–17 314, doi:10.5194/acp-21-17291-2021, 2021.

Vallis, G. K.: Equations of Motion, in: Atmospheric and Oceanic Fluid Dynamics, pp. 3–54, Cambridge University Press, doi:10.1017/9781107588417.002, 2017.

vanZanten, M. C., Stevens, B., Nuijens, L., Siebesma, A. P., Ackerman, A. S., Burnet, F., Cheng, A., Couvreux, F., Jiang, H., Khairoutdinov, M., Kogan, Y., Lewellen, D. C., Mechem, D., Nakamura, K., Noda, A., Shipway, B. J., Slawinska, J., Wang, S., and Wyszogrodzki, A.: Controls on precipitation and cloudiness in simulations of trade-wind cumulus as observed during RICO, Journal of Advances in Modeling Earth Systems, 3, n/a–n/a, doi:10.1029/2011ms000056, 2011.

Varble, A., Fridlind, A. M., Zipser, E. J., Ackerman, A. S., Chaboureau, J.-P., Fan, J., Hill, A., McFarlane, S. A., Pinty, J.-P., and Shipway, B.: Evaluation of cloud-resolving model intercomparison simulations using TWP-ICE observations: Precipitation and cloud structure, Journal of Geophysical Research, 116, doi:10.1029/2010jd015180, 2011.

Vivekanandan, J., Adams, W. M., and Bringi, V. N.: Rigorous Approach to Polarimetric Radar Modeling of Hydrometeor Orientation Distributions, Journal of Applied Meteorology and Climatology, 30, 1053 – 1063, doi:10.1175/1520-0450(1991)030<1053:RATPRM>2.0.CO;2, 1991.

Warner, T. T.: Numerical weather and climate prediction, Cambridge University Press, 2011a.

Warner, T. T.: The governing systems of equations, in: Numerical weather and climate prediction, chap. 2, pp. 6–16, Cambridge University Press, 2011b.

Wilkinson, J. M., Porson, A. N. F., Bornemann, F. J., Weeks, M., Field, P. R., and Lock, A. P.: Improved microphysical parametrization of drizzle and fog for operational forecasting using the Met Office Unified Model, Quarterly Journal of the Royal Meteorological Society, 139, 488–500, doi:10.1002/qj.1975, 2012.

Woodley, W. L.: Precipitation Results from a Pyrotechnic Cumulus Seeding Experiment, Journal of Applied Meteorology and Climatology, 9, 242 – 257, doi:10.1175/1520-0450(1970)009<0242:PRFAPC>2.0.CO;2, 1970.

Wu, D., Zhang, F., Chen, X., Ryzhkov, A., Zhao, K., Kumjian, M. R., Chen, X., and Chan, P.-W.: Evaluation of Microphysics Schemes in Tropical Cyclones Using Polarimetric Radar Observations: Convective Precipitation in an Outer Rainband, Monthly Weather Review, 149, 1055–1068, doi:10.1175/mwr-d-19-0378.1, 2021.

Wyant, M. C., Bretherton, C. S., Chlond, A., Griffin, B. M., Kitagawa, H., Lappen, C.-L., Larson, V. E., Lock, A., Park, S., de Roode, S. R., Uchida, J., Zhao, M., and Ackerman, A. S.: A single-column model intercomparison of a heavily drizzling stratocumulus-topped boundary layer, Journal of Geophysical Research, 112, doi:10.1029/2007jd008536, 2007.

Xue, L., Fan, J., Lebo, Z. J., Wu, W., Morrison, H., Grabowski, W. W., Chu, X., Geresdi, I., North, K., Stenz, R., Gao, Y., Lou, X., Bansemer, A., Heymsfield, A. J., McFarquhar, G. M., and Rasmussen, R. M.: Idealized Simulations of a Squall Line from the MC3E Field Campaign Applying Three Bin Microphysics Schemes: Dynamic and Thermodynamic Structure, Monthly Weather Review, 145, 4789–4812, doi:10.1175/mwr-d-16-0385.1, 2017.

Yuter, S. E. and Houze, R. A.: Three-Dimensional Kinematic and Microphysical Evolution of Florida Cumulonimbus. Part II: Frequency Distributions of Vertical Velocity, Reflectivity, and Differential Reflectivity, Monthly Weather Review, 123, 1941 – 1963, doi:10.1175/1520-0493(1995)123<1941:TDKAME>2.0.CO;2, 1995.

Zadeh, L. A.: Fuzzy sets, Information and Control, 8, 338–353, doi:10.1016/s0019-9958(65)90241-x, 1965.

Zhang, Y., Zhang, F., Stensrud, D. J., and Meng, Z.: Practical Predictability of the 20 May 2013 Tornadic Thunderstorm Event in Oklahoma: Sensitivity to Synoptic Timing and Topographical Influence, Monthly Weather Review, 143, 2973–2997, doi:10.1175/mwr-d-14-00394.1, 2015.

Zhang, Y., Zhang, F., Stensrud, D. J., and Meng, Z.: Intrinsic Predictability of the 20 May 2013 Tornadic Thunderstorm Event in Oklahoma at Storm Scales, Monthly Weather Review, 144, 1273–1298, doi:10.1175/mwr-d-15-0105.1, 2016.

Zhu, K., Zhang, C., Xue, M., and Yang, N.: Predictability and skill of convection-permitting ensemble forecast systems in predicting the record-breaking "21·7" extreme rainfall event in Henan Province, China, Science China Earth Sciences, 65, 1879–1902, doi:10.1007/s11430-022-9961-7, 2022.

Zängl, G., Reinert, D., Rípodas, P., and Baldauf, M.: The ICON (ICOsahedral Non-hydrostatic) modelling framework of DWD and MPI-M: Description of the non-hydrostatic dynamical core, Quarterly Journal of the Royal Meteorological Society, 141, 563–579, doi:10.1002/qj.2378, 2014.

Acknowledgements

I gratefully acknowledge the project IcePolCKa (Investigation of the initiation of convection and the evolution of precipitation using simulations and polarimetric radar observations at C- and Ka-band) funded by the German Research Foundation (Deutsche Forschungsgemeinschaft, DFG) – 408027579 – as part of the special priority program 2155 PROM (Polarimetric Radar Observations meet Atmospheric Modelling – Fusion of Radar Polarimetry and Numerical Atmospheric Modelling Towards an Improved Understanding of Cloud and Precipitation Processes; Trömel et al., 2021). I further would like to thank the German Meteorological Service (Deutscher Wetterdienst, DWD) for providing the polarimetric radar data from the operational C-Band radar in Isen that served as a data basis for many of the results presented in this work.

My time as a PhD student has certainly been a good one. When I started in 2019, I was new to the city of Munich, knowing not a single person beforehand. The group put me into the "Kinderzimmer" – an office with fellow PhD students, who were known to have a fable for experimenting. There really could not have been a better place for me. I learned many fun and practical things: how to steer our radar with a playstation controller or how to install LED warning lights that would start to glow whenever there was a thunderstorm to measure in the vicinity. I especially want to mention Tobias Kölling, who really is a genius in programming languages. He always had time to explain to me how to solve certain programming issues, and he simply seemed to enjoy helping others, which is really a nice character trait that makes it easy to accept the help. I would further like to thank Fabian Jakub, Veronika Pörtge, Philipp Gregor, Richard Maier, Paul Ockenfuss, Mihail Manev, Felix Gödde, and all my other fellow PhD students for all the discussions and just for the great time I had. There is not a single one that I did not come to like, and you all were a big reason why I came to enjoy living in a new city so much.

Furthermore, I would like to thank our group leader Bernhard Mayer and my supervisors, Tobias Zinner and Christoph Knote. I heard stories many times about PhD students who felt isolated or left alone with their research problems. This is certainly not the case in this group. In weekly meetings, you would listen to my progress, and give me constructive feedback or discuss new ideas. I do not think that this is a given, so I would like to thank you for this.

I would also like to thank our cooperation group of the German Aerospace Center (DLR). Martin Hagen, Florian Ewald, and especially Eleni Tetoni, it has been a pleasure working with you, and I am happy that our cooperation will continue in the next years.

For proof reading this thesis, I would like to thank Aleksandar Keserovic, Tobias Zinner, and Mihail Manev.

There is a bunch of software, that deserves a shoutout, too. Above all, I would like to thank all python developers for the great language. It is my all-time favorite and nowadays, I do basically everything in python. Furthermore, I would like to thank freely available English translators, for example "deepl.com", that I came to use frequently whenever I was not able to find satisfying wording with my non-native English. There is the open source Weather Research and Forecasting (WRF; Skamarock et al., 2019) model, freely available on GitHub (https://github.com/wrf-model/WRF; last access: June 20, 2020; https://doi.10.5065/1dfh-6p97, Skamarock et al. (2019)), which I used for my numerical weather prediction. There is the "Cloud-resolving model Radar SIMulator" (CR-SIM; Oue et al., 2020), freely available on the website of the Stonybrook University (https://you.stonybrook.edu/radar/research/radar-simulators/, Oue et al. (2020)), a useful tool to simulate polarimetric radar signals from the numerical model output. There is the hydrometeor identification (HID) algorithm freely available on GitHub (https://github.com/CSU-Radarmet/CSU_RadarTools; last access: November 15, 2022; https://doi:10.5281/zenodo.2562063, Lang et al. (2019)), that I used to classify hydrometeors from the polarimetric radar signals.

There is a lot behind the scenes that influenced my work, even though not directly related. I am very thankful for the support that I get from my family. Jörg, Annelie, Jonas - not only can I ask basically anything from you, I also am very aware that I had a very easy path in life so far. I know that much of this is really your credit in the end, a result from the way you raised me, the things you taught me and the time we spent together. That is why I would like to say: Thank you. You are awesome.

Finally, I am exceptionally grateful to my wife, Anni. It really is a blessing to have a person in your life who just got your back. It does not matter what I need – it can be moral support, it can be help in repairing anything (which I am really not good at) or nursing when I am sick – it is nice to have someone that I can trust to be there with me.
We are a good team.